

**Development of a Closed-loop degaussing system  
Towards magnetic unobservable vessels**

Vijn, A.R.P.J.

**DOI**

[10.4233/uuid:ae431c9d-cbb3-4b5f-88c9-86d4ee81cabe](https://doi.org/10.4233/uuid:ae431c9d-cbb3-4b5f-88c9-86d4ee81cabe)

**Publication date**

2021

**Document Version**

Final published version

**Citation (APA)**

Vijn, A. R. P. J. (2021). *Development of a Closed-loop degaussing system: Towards magnetic unobservable vessels*. [Dissertation (TU Delft), Delft University of Technology]. <https://doi.org/10.4233/uuid:ae431c9d-cbb3-4b5f-88c9-86d4ee81cabe>

**Important note**

To cite this publication, please use the final published version (if applicable).  
Please check the document version above.

**Copyright**

Other than for strictly personal use, it is not permitted to download, forward or distribute the text or part of it, without the consent of the author(s) and/or copyright holder(s), unless the work is under an open content license such as Creative Commons.

**Takedown policy**

Please contact us and provide details if you believe this document breaches copyrights.  
We will remove access to the work immediately and investigate your claim.

**DEVELOPMENT OF A CLOSED-LOOP  
DEGAUSSING SYSTEM**

TOWARDS MAGNETIC UNOBSERVABLE NAVAL VESSELS



# **DEVELOPMENT OF A CLOSED-LOOP DEGAUSSING SYSTEM**

TOWARDS MAGNETIC UNOBSERVABLE NAVAL VESSELS

## **Proefschrift**

ter verkrijging van de graad van doctor  
aan de Technische Universiteit Delft,  
op gezag van de Rector Magnificus Prof.dr.ir. T.H.J.J. van der Hagen,  
voorzitter van het College voor Promoties,  
in het openbaar te verdedigen op donderdag 9 December 2021 om 15:00 uur

door

**Adrianus Robert Petrus Johannes VIJN**

wiskundig ingenieur,  
Technische Universiteit Delft, Nederland  
geboren te Den Haag, Nederland

Dit proefschrift is goedgekeurd door de

promotor	prof. dr. ir. A.W. Heemink
promotor	prof. dr. ir. M.B. van Gijzen
promotor	dr. J.L.A. Dubbeldam
copromotor	dr. ir. E.S.A.M. Lepelaars

Samenstelling promotiecommissie:

Rector Magnificus,	voorzitter
Prof. dr. ir. A.W. Heemink,	Technische Universiteit Delft, promotor
Prof. dr. ir. M.B. van Gijzen,	Technische Universiteit Delft, promotor
Dr. J.L.A. Dubbeldam,	Technische Universiteit Delft, promotor
Dr. ir. E.S.A.M. Lepelaars	Technische Universiteit Delft, copromotor

*Onafhankelijke leden:*

Prof. dr. O.N. Chadebec	Grenoble-INP, France
Prof. dr. A. Yarovoy,	Technische Universiteit Delft
Dr. ir. R.F. Remis,	Technische Universiteit Delft
Prof. dr. ir. C. Vuik,	Technische Universiteit Delft



*Keywords:* Magnetic signatures, closed-loop degaussing, ferromagnetism, hysteresis, data-assimilation  
*Printed by:* Ipskamp Printing, Enschede

Copyright © 2021 by A.R.P.J. Vijn

ISBN 978-94-6366-483-7

An electronic version of this dissertation is available at  
<http://repository.tudelft.nl/>.

*Few subjects in science are more difficult  
to understand than magnetism.*

David Jiles



# INHOUDSOPGAVE

<b>Summary</b>	<b>xi</b>
<b>Samenvatting</b>	<b>xiii</b>
<b>1 Introduction</b>	<b>1</b>
1.1 Background	1
1.1.1 Naval mines	2
1.2 The signature of a naval vessel	3
1.2.1 The magnetic signature of a naval vessel	4
1.2.2 Magnetic signature research	5
1.3 Mine counter measures	5
1.3.1 Induced and Permanent Magnetisation	5
1.3.2 Deperming a naval vessel	6
1.3.3 Degaussing	6
1.4 Mathematical formulation of the problem	8
1.4.1 Mathematical- Physical Model	8
1.4.2 Inverse modeling	9
1.4.3 Regularisation	10
1.4.4 Data Assimilation	10
1.5 Outline of this thesis	11
1.5.1 Research Objectives	11
1.5.2 Required models in Closed-loop Degaussing	11
1.6 Organisation of the thesis	12
References	13
<b>2 A crash course in Magnetism</b>	<b>15</b>
2.1 What is the nature of a magnetic field?	16
2.2 Biot-Savart law	18
2.3 Definition of the magnetic field	19
2.4 Magnetic induction field and flux	19
2.5 Maxwell's Equations	20
2.6 Solving the magnetostatic field equations	21
2.6.1 The Helmholtz Theorem	21
2.6.2 Solution based on a scalar potential	22
2.6.3 Solution based on a vector potential	23
References	23

<b>3</b>	<b>Ferromagnetic Models for Magnetic Signature Prediction: a study to select the right model</b>	<b>25</b>
3.1	Introduction . . . . .	26
3.2	Ferromagnetism . . . . .	26
3.3	Material models . . . . .	28
3.3.1	Model of induced and permanent magnetisation ( <b>IP</b> ) . . . . .	30
3.3.2	Rayleigh Hysteresis Model ( <b>RM</b> ) . . . . .	31
3.3.3	Jiles Atherton Hysteresis Model . . . . .	35
3.3.4	Energy-Based variational model ( <b>EV</b> ) . . . . .	40
3.4	Assessment of hysteresis models . . . . .	45
3.4.1	Number of free parameters . . . . .	46
3.4.2	Computational complexity . . . . .	47
3.4.3	Parameter estimation of models. . . . .	47
3.5	Comparison of models to experimental data. . . . .	48
3.5.1	Demagnetisation factors of a general ellipsoid . . . . .	48
3.5.2	Measurement data of steel ellipsoid. . . . .	50
3.6	Conclusion . . . . .	51
	References . . . . .	53
<b>4</b>	<b>Magnetic Susceptibility Estimation for Magnetostatics</b>	<b>57</b>
4.1	Introduction . . . . .	57
4.2	Methodology . . . . .	59
4.2.1	Magnetostatics . . . . .	59
4.2.2	The discrete forward problem. . . . .	60
4.2.3	Inverse problem formulation . . . . .	63
4.2.4	Inversion, minimization problem . . . . .	64
4.2.5	Inversion, Regularization . . . . .	65
4.2.6	Inversion, Solving the minimization problem . . . . .	66
4.2.7	Magnetic susceptibility estimation method . . . . .	67
4.3	Numerical Examples . . . . .	67
4.3.1	Solving the integral equation . . . . .	67
4.3.2	Twin experiment for parameter estimation . . . . .	68
4.3.3	Experiment Design . . . . .	70
4.4	Sensitivity Analysis . . . . .	72
4.4.1	Forward propagation of magnetic susceptibility . . . . .	72
4.5	Conclusion . . . . .	75
	References . . . . .	76
	<b>Appendix A. Adjoint method for gradient computations</b>	<b>78</b>
	<b>Appendix B. Subtle application of the divergence theorem of Gauss</b>	<b>80</b>
<b>5</b>	<b>Parameter Estimation for the Jiles-Atherton Model in Weak Fields</b>	<b>83</b>
5.1	Introduction . . . . .	84
5.2	Ferromagnetic Hysteresis. . . . .	86
5.2.1	Jiles-Atherton Model . . . . .	86
5.2.2	General form of PDE for <b>JA+R</b> . . . . .	88

5.3	Initial magnetisation distribution $M_0$ . . . . .	88
5.4	Parameter estimation of JA+R . . . . .	90
5.4.1	Forward problem . . . . .	91
5.4.2	Minimization Problem . . . . .	91
5.4.3	Solving the minimization problem . . . . .	92
5.5	Measurement setup . . . . .	92
5.6	Experimental Result . . . . .	92
5.6.1	Specimen description . . . . .	93
5.6.2	Measuring a minor loop . . . . .	94
5.6.3	Initial magnetisation determination . . . . .	94
5.6.4	Parameter estimation results . . . . .	95
5.6.5	Error analysis of SFLA results . . . . .	96
5.6.6	Computational effort . . . . .	98
5.7	Conclusion . . . . .	98
	References . . . . .	100
<b>Appendix A. Table of JA+R parameter boundaries for SFLA</b>		<b>104</b>
<b>Appendix B. Parameter estimation flowchart</b>		<b>104</b>
<b>6</b>	<b>Prediction of the Magnetic State of Ferromagnetic Objects by Assimilating Data into a Physical Model</b>	<b>107</b>
6.1	Introduction . . . . .	108
6.2	Assumptions . . . . .	109
6.3	Magnetostatics . . . . .	110
6.4	Method of Moments . . . . .	111
6.5	Static forward and inverse problem . . . . .	113
6.5.1	Static Forward Problem. . . . .	113
6.5.2	Static Inverse Problem . . . . .	113
6.5.3	Permanent magnetisation estimation . . . . .	114
6.5.4	Operators for regularisation. . . . .	115
6.5.5	Dictionary regularisation as a preconditioner . . . . .	117
6.6	Hysteresis model and connection to the Method of Moments . . . . .	118
6.6.1	Rayleigh's hysteresis model . . . . .	118
6.6.2	Mathematical model for temporal behaviour of a ferromagnetic object. . . . .	120
6.7	Hybrid Model Based on Data Assimilation . . . . .	120
6.7.1	Initial magnetic state . . . . .	120
6.7.2	Data assimilation . . . . .	120
6.7.3	Magnetic state update . . . . .	121
6.8	Test Object . . . . .	122
6.9	Numerical twin experiment . . . . .	122
6.9.1	Computation of the simulated data set . . . . .	123
6.9.2	Results of Twin Experiment . . . . .	124
6.10	Application of the Hybrid Model to Experimental Data . . . . .	129
6.11	Conclusion . . . . .	132
	References . . . . .	133

<b>Appendix A. Pseudo-code for hybrid model</b>	<b>135</b>
<b>7 Conclusion</b>	<b>137</b>
7.1 Answers to the research questions . . . . .	137
7.2 Recommendations for future work . . . . .	138
<b>Acknowledgements</b>	<b>141</b>
<b>Curriculum Vitæ</b>	<b>143</b>
<b>List of Publications</b>	<b>145</b>

# SUMMARY

The focus of this thesis is to study the magnetic behavior of ferromagnetic materials, parameter estimates of the material properties of ferromagnetic materials, and to introduce a mathematical physics model that can accurately describe the temporal changes of the magnetic state of a naval vessel. The aspects mentioned are important steps in the development of a closed-loop degaussing system.

In the introduction, extensive attention is paid to the background of the magnetic signatures domain. Since the early twentieth century, sea mines have been seen as a major threat to civilian ship traffic around the world. This led to the decision at the 1907 Peace Conference that the use of sea mines should be strictly regulated in order to ensure safety on sea routes. Since then, the development of sea mines has not stood still, and due to technological developments, sea mines are becoming smarter and therefore more dangerous. We then describe how the magnetic signature of a naval vessel introduces a vulnerability to smart sea mines. The challenges this threat creates are named, and we show what traditional solutions have been devised to address them. Finally, we describe the mathematical formulation of the problem we consider in this thesis and define a number of research questions that are central to it.

In Chapter 2 we give a brief description of the physical background used throughout the thesis. Through a “Crash course” we explain the origin of magnetization and show what (macroscopic) physical principles underlie magnetization. We end by solving the magneto-static equations, and show how the application of Helmholtz’s theorem provides an elegant description of magnetic fields, given the magnetization distribution of a magnetized object. These expressions are a starting point for the derivation of the mathematical-physical model (the “Method of Moments”) in Chapters 4 and 6.

Chapter 3 considers an extensive literature review comparing different models that have been proposed in the past for the description of ferromagnetic behavior. In particular, we review (1) the traditional model that divides the magnetic signature into an induced part and a permanent part (this is strictly not a description of hysteresis), (2) the hysteresis model of Lord Rayleigh, (3) the model of Jiles and Atherton, and (4) the Energy-Based variational model by Progizhin and others. The purpose of this study is to understand which model is best suited to be used in describing the magnetic behavior of a large ferromagnetic object, such as a naval vessel. For this purpose, we consider not only the accuracy in describing ferromagnetic behavior, but also the complexity of implementing the models. A trade-off is made herein.

Chapter 4 introduces a parameter estimation method for the magnetic susceptibility distribution in for linear reacting materials. For a good description of the magnetic state, it is

important to accurately map the magnetic susceptibility distribution. It is conceivable that a the material from which an object is constructed is inhomogeneous. Based on the magnetostatic equations, an integral equation is derived that describes the induced behavior of the object, under the condition that the magnetic susceptibility distribution is known. The parameter estimator relies on solving the corresponding inversion problem. This means that given a collection of magnetic measurements of a magnetized object in a given background field, an estimate of the best magnetic susceptibility distribution is made. The addition of regularization supports this search, and imposes a smoothness requirement on the solution of the inverse problem.

Chapter 5 introduces a parameter estimator for an extension of the Jiles Atherton model. The extension is designed to guarantee closed minor loops in the hysteresis curve; this is a well-known artifact in the traditional Jiles and Atherton model. These types of estimators are more common in the literature, but the focus in this chapter is in the derivation of the material parameters in the absence of weak fields. This is in contrast to well-known parameter estimators that require that the applied field can be so strong that saturation in the material can occur. The parameter estimator we propose consists of two steps. In the first step, an initial magnetization estimate is made based on an inversion model. For this purpose, a collection of radial functions is used to represent the magnetization distribution of a steel plate. Then, in the second step, a dataset of measurements of the interference field for a varying background field is used to estimate, through a memetic algorithm (the Shuffled Leaping Frog Algorithm), the optimal values for the material properties of the Jiles Atherton model.

Chapter 6 introduces two concepts. On the one hand, a mathematical-physical model is proposed that can describe the temporal variations in the magnetic state of a ferromagnetic object. On the other hand, we propose a data assimilation scheme that, through magnetic field measurements, improves the descriptive power of the mathematical-physical model. In the mathematical model, we distinguish between the initial magnetization estimate and an integration of the model over time. In a first step, the Method of Moments underlying the description of the interaction between the ferromagnetic object and the background field is described. Based on this, an inverse problem is derived that serves to estimate the initial magnetization distribution. Next, the coupling between the Moments method and the Rayleigh hysteresis model is considered. Together this forms the mathematical-physical model used to describe the temporal variations in magnetization. Building on the mathematical-physical model, we introduce a data assimilation scheme, which can be used to improve the estimation of the magnetization of a ferromagnetic object over time. Finally, we analyse the accuracy of the proposed model through a numerical Twin Experiment, and validate that the mathematical-physical model, in combination with the data-assimilation scheme, is able to accurately represent the experimental data.

In Chapter 7, we conclude this thesis and make a number of recommendations for a continuation of the presented research.

# SAMENVATTING

De focus van dit proefschrift ligt op het bestuderen van het magnetisch gedrag van ferromagnetische materialen, parameterschattingen van de materiaaleigenschappen van ferromagnetische materialen en het introduceren van een mathematisch fysisch model die de temporele veranderingen van de magnetische staat van een marineschip nauwkeurig kan beschrijven. De genoemde aspecten zijn belangrijke stappen in de ontwikkeling van een closed-loop degaussing systeem.

In de introductie wordt uitgebreid aandacht geschonken aan de achtergrond van het magnetische signature domein. Sinds het begin van de twintigste eeuw worden zeemijnen gezien als een grote dreiging voor civiel scheepsverkeer op de wereld. Dit heeft ertoe geleid dat tijdens de vredesconventie in 1907 besloten is dat het gebruik van zeemijnen streng gereguleerd moet worden, om zo de veiligheid op vaarroutes op zee te kunnen waarborgen. Sindsdien heeft de ontwikkeling van zeemijnen niet stilgelegen, en vanwege technologische ontwikkelingen worden zeemijnen steeds slimmer en dus gevaarlijker. Vervolgens beschrijven we hoe de magnetische signatuur van een marineschip een kwetsbaarheid voor slimme zeemijnen introduceert. De uitdagingen die deze dreiging creeëert worden benoemd, en we laten zien welke traditionele oplossingen hiervoor zijn bedacht. Als laatste beschrijven we de wiskunde formulering van het probleem dat we in dit proefschrift beschouwen en definiëren we een aantal onderzoeksvragen die centraal staan.

In hoofdstuk 2 geven we een beknopte beschrijving van de fysische achtergrond die door het proefschrift heen gebruikt wordt. Via een “Crash course” leggen we uit wat de oorsprong is van magnetisatie en laten we zien welke (macroscopische) fysische principes ter grondslag liggen aan magnetisatie. We eindigen met het oplossen van de magnetostatische vergelijkingen, en laten zien hoe de toepassing van de stelling van Helmholtz een elegante beschrijving geeft van magnetische velden, gegeven de magnetisatie verdeling van een gemagnetiseerd object. Deze uitdrukkingen zijn een startpunt voor het afleiding van het mathematisch-fysisch model (de “Method of Moments”) in Hoofdstuk 4 en 6.

Hoofdstuk 3 beschouwt een uitgebreide literatuurstudie waarin een vergelijking gemaakt wordt tussen verschillende modellen die in het verleden zijn voorgesteld voor de beschrijving van ferromagnetisch gedrag. In het bijzonder bekijken we (1) het traditionele model dat de magnetische signatuur opdeelt in een geïnduceerd deel en een permanent deel (dit is strikt genomen geen beschrijving van hysteresis), (2) het hysteresis model van Lord Rayleigh, (3) het model van Jiles en Atherton en (4) het Energy-Based variational model door onder andere Progizhin. Het doel van deze studie is het begrijpen welk model het meest geschikt is om gebruikt te worden in het beschrijven van het magnetische gedrag van een groot ferromagnetisch object, zoals een marineschip. Met dit doel beschouwen we niet alleen de nauwkeurigheid in de beschrijving van ferromagnetisch gedrag, maar ook de

complexiteit van het implementeren van de modellen. Een afweging wordt hierin gemaakt.

In hoofdstuk 4 wordt een parameterschatting methode voor de magnetische susceptibiliteit verdeling in voor linear reagerende materialen geïntroduceerd. Voor een goede beschrijving van de magnetische staat is het van belang om de magnetische susceptibiliteitsverdeling nauwkeurig in kaart te brengen. Het is niet ondenkbaar dat een het materiaal waaruit een object is geconstrueerd, inhomogeen is. Op basis van de magnetostatische vergelijkingen, wordt een integraalvergelijking afgeleid die het geïnduceerde gedrag van het object beschrijft, onder de voorwaarde dat de magnetische susceptibiliteitsverdeling bekend is. De parameterschatter berust op het oplossen van het corresponderende inversie probleem. Dit houdt in dat gegeven een collectie van magnetische metingen van een gemagnetiseerd object in een gegeven achtergrondveld, een inschatting wordt gemaakt van de beste magnetische susceptibiliteitsverdeling. Door de toevoeging van regularisatie wordt deze zoektocht ondersteunt, en wordt een gladheidseis op de oplossing van het inverse probleem opgelegd.

Hoofdstuk 5 wordt een parameter schatter voor een uitbreiding van het Jiles Atherton model afgeleid. De uitbreiding is erop berust om gesloten minor loops in de hysteresis curve te kunnen garanderen; dit is een bekend artefact in het traditioneel model van Jiles en Atherton. In de literatuur komen dit soort schatters vaker voor, maar de focus ligt in dit hoofdstuk in het afleiding van de materiaalparameters in de afwezigheid van zwakke velden. Dit in tegenstelling tot bekende parameter schatters die eisen dat het aangelegde veld zo sterk kan zijn, dat saturatie in het materiaal kan plaatsvinden. De parameter schatter die we voorstellen bestaat uit twee stappen. In de eerste stap wordt een initiële magnetisatie inschatting gemaakt op basis van een inversie model. Met dit doel wordt een collectie van radiale functies gebruikt om de magnetisatie verdeling van een stalen plaat te representeren. Vervolgens wordt in de tweede stap een dataset van metingen van het stoorveld voor een variërend achtergrondveld gebruikt om, door middel van een memetisch algoritme (het Shuffled Leaping Frog Algorithm), de optimale waarden voor de materiaalparameters van het Jiles Atherton model in te schatten.

Hoofdstuk 6 introduceert twee concepten. Aan de ene kant wordt een mathematisch-fysisch model voorgesteld dat de temporele variaties in de magnetische toestand van een ferromagnetisch object kan beschrijven. Aan de andere kant stellen we een data-assimilatieschema voor dat, door middel van magnetische veldmetingen, de beschrijvende kracht van het mathematisch-fysisch model verbetert. In het mathematisch model maken we onderscheid tussen de initiële magnetisatie schatting en een integratie van het model in de tijd. In een eerste stap wordt de Method of Moments beschreven die ten grondslag ligt aan de beschrijving van de interactie tussen het ferromagnetische object en het achtergrondveld. Op basis hiervan wordt een invers probleem afgeleid dat dient voor het schatten van de initiële magnetisatie verdeling. Vervolgens wordt de koppeling tussen de Momentenmethode en het Rayleigh hysteresis model beschouwd. Samen vormt dit het wiskundig-fysisch model dat wordt gebruikt om de temporele variaties in magnetisatie te beschrijven. Voortbouwend op het wiskundig-fysisch model, introduceren wij een data-assimilatieschema, dat kan worden gebruikt om de schatting van de magnetisatie van een ferromagnetisch object in de tijd te

verbeteren. Tenslotte analyseren we de juistheid van het voorgestelde model door middel van een numeriek Twin Experiment, en valideren we dat het mathematisch-fysisch model, in combinatie met het data-assimilatieschema, in staat is om de experimentele meetdata nauwkeurig te beschrijven.

In hoofdstuk 7 besluiten we dit proefschrift en doen we een aantal aanbevelingen voor een vervolg op het gepresenteerde onderzoek.



# 1

## INTRODUCTION

### 1.1. BACKGROUND

Naval vessels often operate in areas where the threat of naval mines is high. Such fields of naval mines can be found in littoral waters. During a mission, the detonation of naval mines must be avoided to ensure the safety of the vessels and its crew. At this moment<sup>1</sup>, still over a quarter of a million World War II mines are estimated to be active and impose an extra risk to both civilian and military shipping. Furthermore, there is an estimated number of 500.000 up to a million modern influence mines active in Earth's (shallow) waters. Such numbers show the need of *Mine Counter Measures* (MCM).

Naval mines have been known in history for a long time. The first use of primitive naval mines already stems back from the Ming dynasty in the 16<sup>th</sup> century, when the first mines were deployed to target pirates operating in coastal seas near China. These kind of mines consisted of an explosive charge that was loaded into a wooden box and sealed with putty. A rip cord was pulled by hidden defenders located on the nearby shore which allowed them to rotate a steel wheel-lock flint mechanism in the wooden box to produce sparks and ignite the fuse inside the wooden box. During the American Civil war (1860-1865), watertight keg filled with gunpowder naval mines were used. Floating on the sea surface, these contact naval mines approached the enemy and detonated by a sparking mechanism if it did hit a ship. But it was during the Russo-Japanese War (1904-1905) that naval mines were used extensively as a (defensive) weapon. It is estimated that thousands of mines were deployed by the Russians. As a result, they induced high costs to the naval fleet of both belligerents. Unfortunately, it is known that civilians also paid a high price and commercial shipping suffered both during and after the war. More recently, there are a number of detonations known that led to large damages to naval vessels (both intended and unintended). These occurrences clearly show that the threat of naval mines is still a reality. A more recent example is the following: in 2005 three fishermen died in The Netherlands after a naval mine was fished up and accidentally detonated.

---

Parts of this section are taken from [27].

<sup>1</sup>source: <https://www.naval-technology.com>

In the past the use of naval mines in conflicts led to the desire to introduce a ban on naval mines, in particular the unanchored ones, as such classes of mines were a huge threat to civilian shipping as well due to the lack to control their location. It was during the Peace convention in The Hague in 1907 that a treaty was defined to regulate the use of naval mines in both times of war and peace. The treaty, called Hague VIII [4], defined the regulations and focussed on the principle “freedom of sea routes, the common highway of all nations”. Furthermore, the treaty forbids the use of unanchored automatic contact mines, under the exception that “they are constructed as to become harmless at most one hour after the person who laid them ceases to control them” [8]. It was clear for all nations (involved in this treaty) that these mines are far too dangerous to civilians in both war and peace time.

### 1.1.1. NAVAL MINES

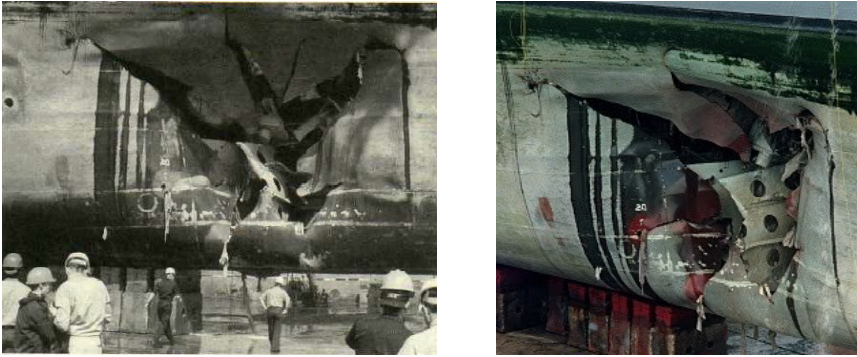
As a weapon naval mines are relatively cheap but have a significant value in both a tactical, operational and strategic point of view. They can be used as a blockages of passage for ships at strategic locations, or to (heavily) damage and sink ships. NATO [4, page 3] defines a naval mine as follows:

*“An naval mine is an explosive device laid in the water, on the seabed or in the subsoil therefore, with the intention of damaging or sinking ships or deterring shipping from entering an area.”*

There are a number of types of naval mines known in the literature. They are categorized in following four classes:

- **Moored Mines:** These are tethered to the bottom of the sea bed by an anchor and hover beneath the sea surface. In general detonation takes place when a ship comes in contact with the mine. This implies that this type of mines can only be used in shallow waters up to 200 meters to ensure possible contact with the hull of a vessel.
- **Drifting mines:** As the name suggests, these mines are not anchored to the seabed and can move freely in the water. It is clear that such mines impose a huge risk to unintended targets as one cannot control the location of the mine accordingly.
- **Bottom mines:** Nowadays, technologically advanced mines called multi-influence mines are deployed on the sea bed and can operate completely autonomously. These mines can sense the surrounding using magnetic, electric, acoustic, seismic and pressure signal in order to determine if a naval ship is near. On the basis of this information, a mine can decide to actuate. These mines are most effective when used in shallow waters up to 200 meters.
- **Rising and rocket mines:** These are highly advanced mines moored to the bottom of the sea bed. Because of their design, these mines can be used effectively at depths up to 2000 meters.

The effects of an underwater explosion on a ship is a complex phenomenon that involves both the environmental conditions in the which the explosion occurs, propagation of the detonation wave, energy dissipation to the environment (absorption of energy by the water),



Figuur 1.1: On February 18th 1991, the USS “Tripoli” LPH-10, an Iwo Jima-class amphibious assault ship, hit a LUGM-145 mine in the Persian Gulf. The resulting explosion made a breach of 16 by 20 meters. The mine weighted 145 kg and its price was below \$1000. The repair costs at that time amounted to 3.5 million dollars. Source [23].

reflection of the shock wave from the bottom of the seabed, currents in the sea, wave interferences of the initial detonation wave and its reflection, cavitation in the sea, the location of the explosion with respect to the location of the vessel, the mass of explosive material and more [23].

For bottom mines such as multi-influence mines the explosion itself does not directly damage a vessel due to the relatively large distance, but the induced shock wave is the main source for potential damage. During an explosion, the solid state of the explosive material rapidly transforms, within a time span of  $10^{-7}$  seconds, into a gas at an initial temperature of approximately 3300 Kelvin and pressures reaching up to 14000 MPa. The resulting spherical shock wave propagates through the water at a speed of 5000 – 8000 meters per seconds; such waves decay in strength proportional to the travelled distance. The pressure at the front of a shock wave is a leading measure to indicate how severe the damage will be. As explained in [23], pressures of at least 27 MPa will likely result in the sinking of the ship, but pressures of approximately 6 – 12 MPa can already have devastating effects on the electronics of a vessel and crack the hull, taking away (combat) capabilities of a vessel. In Fig. 1.1 an example of the effects of an exploding naval mine is shown. It is a well-known case to illustrate the threat of naval mines.

## 1.2. THE SIGNATURE OF A NAVAL VESSEL

As mentioned already, a modern influence mine uses sensors to measure signals in order to determine whether or not a vessel is near. If indeed a vessel is near, an influence mine can decide to actuate. For naval mines, the following underwater signals are the most interesting:

- A **magnetic field** surrounding a vessel that locally disturbs the Earth magnetic field. This disturbance is caused by the ferromagnetic material in the construction of the vessel, steel equipment on board of the vessel and weaponry.
- An **electric field** is partially caused by on-board equipment that works on electricity.

Also the motion of the vessel in a background field generates a small contribution to the electrical field. The main cause however is the cathodic protection of the system: using electricity to avoid corrosion of the vessel's hull and propellers. A current along the vessel's hull induces also a contribution to the magnetic field that surrounds the vessel. However, such magnetic fields are small.

- Sources for **Acoustic waves** are the on-board machinery, noise from the propeller, flow noise and the Target Echo Strength.
- Pressure waves are generated by the water displacement by the vessel. As a result, a wake is created behind the vessel, which is a contribution to the Radar Cross Section (RCS) of the vessel.

Thus, the existence of these signals makes vessels susceptible to threats of a potential adversary. Besides the obvious threat of a naval mine, the risk of being detected is in some cases an equal threat. To protect naval vessels to the threat of a naval mine, it is important to know how strong these signals are, how they propagate through the surrounding media to be able to minimize and control the signals as good as possible.

It is clear that these signals depend uniquely on the ship's design, the environment, location and use of the naval vessel. Therefore we define the **signature** of a naval vessel as this complete "picture" of these signals in its surroundings. The reduction of these signals increases the probability of mission success of a naval vessel. We speak of the **magnetic signature** whenever we consider the magnetic distortion field of a naval vessel with respect to the Earth magnetic field.

### 1.2.1. THE MAGNETIC SIGNATURE OF A NAVAL VESSEL

In our current research we solely consider the magnetic signature of a naval vessel. The steel structure of the naval vessel acts as a magnet, and therefore creates a magnetic field surrounding the vessel. By approximation, we may assume that the Earth's magnetic field is uniform locally. It is therefore a logical choice to talk about a distortion of the Earth magnetic field by a naval vessel, yielding the possibility to identify the presence of a naval ship based on measurements of the magnetic field. It is therefore important to reduce magnetic signatures to an acceptable level to ensure safety. One can distinguish a number of sources that contribute to the magnetic signature, in order of significance:

- (1) The **interaction** between the steel ship structure and the static Earth's magnetic field;
- (2) The use of **cathodic protection** to control the corrosion of the metal surface of a naval vessel and propellers;
- (3) **Eddy currents** in the vessel's hull by the motion of the vessel in Earth's magnetic field;
- (4) **Stray fields** generated by electrical equipment, cabling and weaponry on the vessel.

In this thesis, we limit ourselves to the first contribution, that is, the interaction between the steel ship construction and the Earth's magnetic field.

The interaction of Earth's background field and the steel construction of a vessel is a complex phenomenon and its nature is based on physical principles on a microscopic level

called *ferromagnetism*. Concepts and models describing ferromagnetism will be explained in Chapter 3, where a number of potential ferromagnetic models are investigated and compared.

In more detail, ferromagnetic behaviour of steel consists of the following properties and effects (see Chapter 3):

- **Hysteresis:** the *magnetic memory* of steel constantly changes the instantaneous response of steel to an applied field. It is indicated by a non-linear relationship between the internal magnetic field and magnetic induction field inside ferromagnetic material. The evolution of the magnetisation in time depends on the the past values of the applied magnetic field.
- **Magneto-Mechanical effects:** The behavior and properties of steel change due to mechanical stress. Examples of mechanical stress are for example bending/welding of steel plates or damage to the vessel's hull due to military weapons.

### 1.2.2. MAGNETIC SIGNATURE RESEARCH

Signature research is an important field for many nations worldwide. Due to technological developments in the field of electronics, robust sensors with increasing sensitivity are being developed with decreasing costs. Therefore, signature reduction requires constant attention. Unfortunately, due to its classified nature, scientific developments in this field are not always shared in (peer-reviewed) papers and thus it is not always clear what state-of-the-art developments are.

## 1.3. MINE COUNTER MEASURES

As mention in Section 1.1, there is a need for mine counter measures to protect both the military vessels and civilians in both peace and war time. A signature management system is potentially a great counter measure against mine threats, but requires both good (mathematical) models that describe signatures in an accurate way and knowledge about environmental parameters such as the location of mine fields.

Since the use of influence mines in the second world war, effective counter measures have been developed. After the allied forces in the war discovered the extensive use of the magnetic signatures in sea mines, they started with investigating means to avoid the detonation of sea mines. This led to the notions of *deperming* and *degaussing*.

### 1.3.1. INDUCED AND PERMANENT MAGNETISATION

In the field of magnetic signatures, it is common practice to linearise the complex ferromagnetic behaviour by the superposition of permanent magnetisation (constant in time) and induced magnetisation due to a linear response of the steel material to the earth magnetic field (see Chapter 3 for an explanation about this separation into a permanent- and induced magnetisation.). For this induced magnetisation, the permeability of the material is important. In the case of steel, the **relative permeability**  $\mu_r$  is in the order of  $100 - 10^6$ . Therefore, a vessel's induced magnetisation changes significantly over time while moving through the earth magnetic field. A schematic overview of the magnetic signature in the Earth magnetic field can be found in Fig. 1.2. The signature is orientated in the same

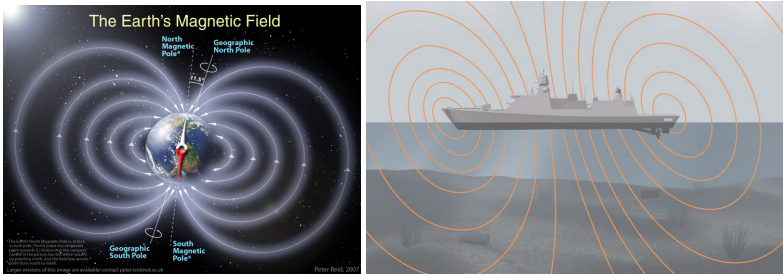


Figure 1.2: (left) A schematic overview of the Earth magnetic field. Note that the geomagnetic north pole lies near the geographic south pole, as the fields lines are pointing outward. source: <http://www.nasa.gov>. (right) The induced magnetic signature of a steel vessel at the Northern Hemisphere. The Earth magnetic field pointing vertically inwards the Earth, and therefore the vertical component of the magnetic signature is dominant.

direction as the Earth magnetic field. Measures are required to reduce the contributions of permanent and induced magnetisation to the magnetic signature to keep the magnetic signature below acceptable levels to remain magnetically unobservable.

### 1.3.2. DEPERMING A NAVAL VESSEL

One of the most effective ways to reduce the magnetic signature of a naval vessel, is the use of a deperming treatment<sup>2</sup>. After the construction of a vessel, a (strong) magnetic signature is unavoidable due to the mechanical stresses that build up in the material during construction. The ferromagnetic nature of steel and the internal mechanical stresses lead to a *permanent magnetisation* of the vessel's structure.

Deperming, or demagnetisation of the vessel, is a treatment that is typically done a few times in the lifetime of a naval vessel. Depending on the deperming range, a vessel is either positioned within a coil system, or coils are wrapped around the vessel. In Fig. 1.4 the Lambert Point Deperming Facility is shown. During deperming, an alternating decaying current in the coils generates a magnetic field reduces the permanent magnetisation. Sometimes a number of such treatments are required to obtain the necessary reductions. Unfortunately, it is observed that the permanent magnetisation grows over time when a vessel is moving in the Earth magnetic field. Therefore after some time another deperming treatment may be necessary.

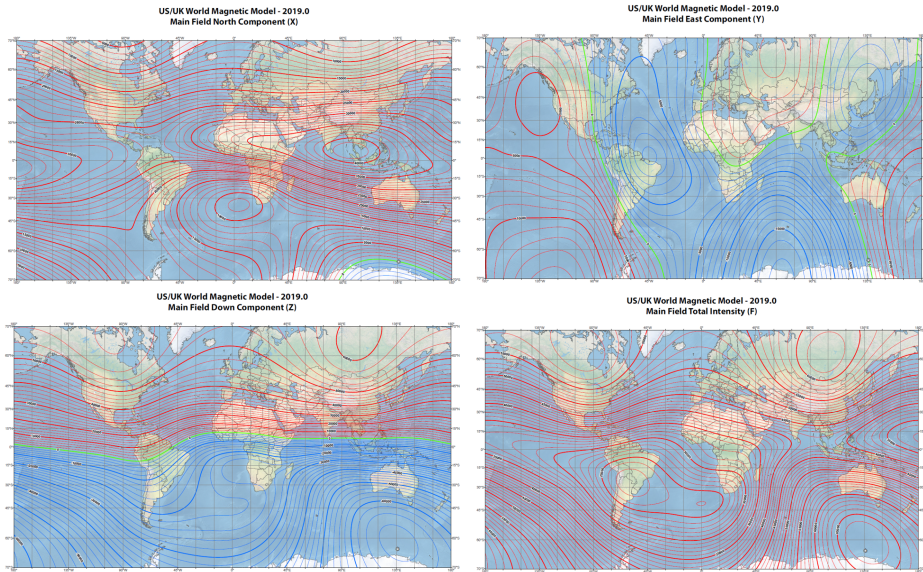
### 1.3.3. DEGAUSSING

After a deperming treatment, the permanent magnetisation is reduced to an acceptable level. However, due to the ferromagnetic nature of steel, the steel hull of a vessel magnetises over time when it moves through the Earth magnetic field. This implies that the magnetic signature may still exceed certain norms, leading to vulnerable platforms and possible risks to mission success.

The term *degaussing*<sup>3</sup> was first coined by then-Commander Charles F. Goodeve, RCNVR during World War II. The Axis forces developed a naval mine with a detonation

<sup>2</sup>Building ships from nonmagnetic material is an even better way to reduce magnetic signatures, but there may exist restrictions on the vessel's capabilities and its operational purposes that make this choice of unfavourable.

<sup>3</sup>Source: <https://en.wikipedia.org/wiki/Degaussing>.



Figur 1.3: US/UK World Magnetic Model (WMM). Every five years, a model for the magnetic field of the Earth is updated. WMM2020 consists of a degree 12 spherical harmonic model of the Earth's magnetic main field. This model is calibrated using a large number of measurements of the magnetic field using both ground and satellite data. Note that the magnetic field varies significant across the planet, which a clear distinction of the  $z$ -component in the Northern and Southern Hemisphere. The values of Earth's magnetic induction field varies between  $\pm 60$  microtesla. A red line indicates easterly changes, a blue line westerly changes and green zero change. The contour plots indicates that the geomagnetic south pole of the Earth's magnetic fields lies close the North Pole and vice versa. Source: <https://geomag.bgs.ac.uk/research/modelling/WorldMagneticModel.html>.

mechanism that uses the magnetic field as a measure for detonation. When a steel vessel was near such a mine, the vertical component of the magnetic field, measured by the mine, significantly increased and detonation then followed. In turn, the use of these mines was an effective measure to counter the British Fleet. Admiralty scientists such as Goodeve, developed a system that induced a strong "N-pole up" field, to reduce the strong vertical field of the vessel, meaning that the sum of the two fields (the measured magnetic field and the "N-pole up" field) of the vessel was approximately the same as the Earth magnetic background field. Since the Axis used the gauss as the unit of the strength of the magnetic field, Goodeve referred to the various processes to counter their mines as "degaussing".

A degaussing system is thus the collection of large coils (in three directions) inside the ship's hull, where the currents in each of the coil are controlled. The currents are used to reduce the magnetic signature of the vessel. In the calibration of this degaussing system, two steps are distinguished. First, values for the coil currents are determined to minimise the contribution of permanent magnetisation to the magnetic signature. Note that in traditional systems, the permanent magnetisation is assumed to be constant in time, and therefore the found values only need to be computed once. To compensate the contribution of the induced magnetisation, the values of the coil currents are computed through a simple linear model, that uses the Earth magnetic field as input. An extensive explanation can be found in [11].



Figur 1.4: The Lambert Point Deperming Facility located in the Elizabeth River just off Lambert's Point, Norfolk, Virginia, United States.

## 1.4. MATHEMATICAL FORMULATION OF THE PROBLEM

In the previous section, separation of the magnetic signature into a permanent- and induced part was mentioned. The resulting simple model is used to define a degaussing system that can reduce the magnetic signature. It is observed that the permanent magnetisation in a vessel changes significantly over time [26], and therefore the reduced magnetic signature may exceed its required norm. In order to take the change of permanent magnetisation into account, a more sophisticated mathematical model is required that also describes the dynamics of permanent magnetisation of a naval ship. The model must include the use of data of the ship's motion, sensor data of on-board sensors, historical data and other measurement data, to come up with a correct estimation of the changes in the permanent magnetisation, to control the degaussing currents in the correct way. This model plays a key role in the closed-loop degaussing methodology.

In the development of a mathematical model for the closed-loop degaussing system, the following aspects need to be addressed.

### 1.4.1. MATHEMATICAL- PHYSICAL MODEL

In this thesis, advanced (mathematical) models are considered to capture the complexity of ferromagnetic behavior. The notion of an induced and permanent magnetisation is loosened, as permanent magnetisation is no longer considered "permanent". Instead, the generalisation to magnetic hysteresis is included in the proposed mathematical-physical models, called *ferromagnetic models*. To understand how ferromagnetic hysteresis works, Madelung [15, 17, 30] investigated this behaviour and derived a number of rules that are obeyed by ferromagnetic material. These rules play a starting point in the derivation of mathematical and physical models for ferromagnetism. This results in numerous proposed models in the literature. Examples are the mathematical models by Preisach [25] and Play-& Stop models [1, 18, 19], the hysteresis model proposed by Tellinen [24, 31], a formalism that is

based on physical concepts described by Jiles and Atherton [13, 29], the energy-variational model by Henrotte et al. [10, 16, 22] and simplistic models such as the hysteresis model by Lord Rayleigh [14] and by Zirka and Moroz [30] based on transplantation of the major curve branches.

The above-mentioned models describe ferromagnetism on a material level by a set of parameters. To describe the ferromagnetic behavior of a large structure, the coupling with a finite-element environment or boundary element environment is necessary. In magnetostatics, the Method of Moments is a well known method to describe the strong inter-coupling effects within a magnetic structure. Note that this method is similar to the boundary element method. Examples of the application of the Method of Moments can be found in e.g. [2, 3, 20, 21, 28].

### 1.4.2. INVERSE MODELING

In order to use a ferromagnetic model, the initial magnetic state of a ferromagnetic structure must be determined. The initial magnetic state consists of (1) the magnetisation of the structure and (2) the values of the material parameters. To obtain values for material parameters in the hysteresis model, an inverse modeling framework must be invoked.

To understand this inverse modeling framework, the notions of forward and inverse problems must be understood first. A forward problem is the process of calculating the resulting effects from a set of causes. Contrary to the forward problem, the inverse problem is the process of computing the causal factors from a set of observations. While mathematically speaking, forward problems are well-posed, an inverse problem is typically ill-posed. Hadamard [5, page 31] defined a forward problem to be well-posed if (1) for all admissible data, a solution exists, (2) for all admissible data, the solution is unique, and (3) the solution depends continuously on the data, are all satisfied. A problem is ill-posed if one of the above criteria is not met. As a result, well-posed problems are in general “easy” to solve, while ill-posed problems are typically hard.

In this thesis, the magnetisation of a large structure is found by solving an inverse problem based on measurements of the magnetic induction field in the vicinity of the structure. Such measurements can be used to find either the magnetisation inside the object, or the material parameters of the underlying ferromagnetic hysteresis model. The determination of the magnetisation based on measurements of the magnetic induction field for one fixed setting is called a static inverse problem, while the determination of the values of the material parameters involves capturing the temporal behaviour of the material, and therefore measurements in time are required in order to retrieve these values.

Inverse problems in magnetostatics are mathematically ill-posed. This is related to the smoothing-properties of the Green’s function of the underlying Poisson’s equation. One can prove [27, Section 3.6] that the corresponding bounded linear function  $T$  is compact with finite-dimensional range. Therefore the pseudo-inverse  $T^\dagger$  is discontinuous which finishes the proof. As a direct implication, resulting solutions are very likely to be (numerically) unstable, and hard to solve. In order to resolve such issues regularisation of the problem is required.

### 1.4.3. REGULARISATION

In order to solve an inverse problem, additional information can be added to the problem to prevent overfitting or to reduce the dimensions of the solution space of the problem, therefore making it easier to obtain a solution to the problem. This is called regularisation, see [7].

Regularisation is used in the cases where the inverse problem is either ill-posed or ill-conditioned (in the case of a linear inverse problem). In machine learning applications, regularisation plays an important role in for example classification. Also, regularisation is often applied in continuous optimisation problems. For linear problems, regularisation can be related to the adaptation of singular values of the corresponding singular value decomposition of the linear operator, enforcing the adapted problem to have larger singular values to improve and ensure numerical stability, while reducing the non-uniqueness of the solution as the dimension of the kernel of the linear operator is reduced. Techniques such as Tikhonov regularisation [9], [5, Chapter 5] and truncated singular value decomposition [5, Section 3.3] modify the singular values.

More advanced regularisation techniques tend to include a priori information about the solution that is sought. For example, a smoothness condition can be imposed as a regularisation term to enforce a smooth solution.

### 1.4.4. DATA ASSIMILATION

In general, a mathematical model does not capture all aspects of a physical phenomenon, due to insufficient knowledge about the underlying physical principles, limited computation power, or due to intentionally neglected small effects in the modeling phase. In such cases, the resulting mathematical model is uncertain with limited predictive power to represent the real world accurately. Even if the model itself perfectly represents the real world, solutions will not describe reality due to inaccurate initial or boundary conditions [6, Introduction]. To increase the predictive power of a model, measurement data can be assimilated to update the model parameters. This is called data assimilation.

In mathematics, data assimilation methods are divided into two categories: sequential data assimilation and variational data assimilation. The Kalman filter and Ensemble Kalman filter are well known sequential data assimilation methods, in which the state-vector of a model is updated by assimilation of measurement data using the covariance matrices of the uncertainties in both the model and state vector. The Kalman filter is a robust method for high-dimensional systems, Particle filters or Sequential Monte Carlo (SMC) methods are also sequential methods. However, particle filter methods do not perform well when applied to very high-dimensional systems. Variational data assimilation methods such as 3DVAR and 4DVAR are successfully used in weather forecasting.

In this thesis, however, we follow a more heuristic approach when applying the concept of data assimilation. This is based on the principles behind Kalman filtering, but any statistical considerations are neglected. Using sensor data, discrepancies between the predicted fields on the sensor data by the model and the measured values, are assumed to be related to a change in magnetisation that is not captured by the model. Using a regularised inversion, a change in magnetisation is computed to minimise this discrepancy.

## 1.5. OUTLINE OF THIS THESIS

### 1.5.1. RESEARCH OBJECTIVES

The objectives of this thesis are the development of two models:

- (M1) A **monitoring model** for accurately describing the magnetic signature of naval ships.
- (M2) A **closed-loop degaussing algorithm** for optimal reduction of the magnetic signature.

It is important to note that the two goals are intertwined: the monitoring model takes part in this complex closed-loop degaussing algorithm, because the coil system also affects the magnetic signature and magnetic state of a vessel. To achieve the above-mentioned goals, we distinguish the following research questions in this thesis:

- (RQ1) Investigate the state-of-the art developments in the field of ferromagnetism. Which hysteresis model should we choose for our mathematical-physical model?
- (RQ2) How can we determine the initial magnetic state of a vessel?
- (RQ3) Is it possible to obtain an efficient numerical model that describes the temporal dynamics of the ferromagnetic behavior of a large structure?
- (RQ4) What is the added value of data-assimilation in magnetostatic?

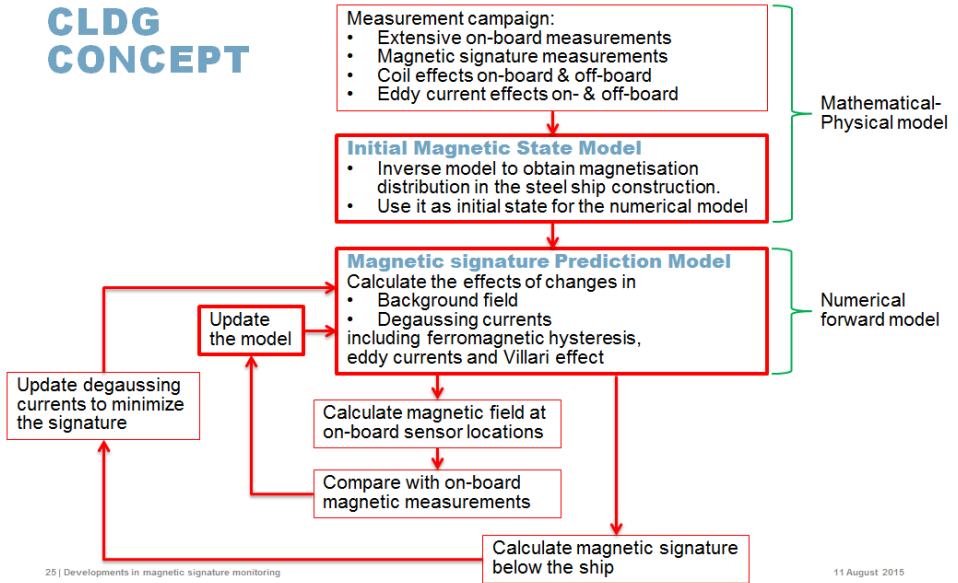
### 1.5.2. REQUIRED MODELS IN CLOSED-LOOP DEGAUSSING

In Figure 1.5 a concept of Closed-Loop DeGaussing (CLDG) is presented. The principle idea behind CLDG is the use of on-board sensor data to update the underlying mathematical model and degaussing currents for optimal reduction of the magnetic signature at any time. The closed-loop degaussing system should update the degaussing currents autonomously on the basis of on-board sensor data and a numerical model. In order to calibrate the degaussing system for a naval vessel correctly, an extensive measurement campaign is necessary to obtain values for the parameters in the numerical model and to determine the initial magnetic state of the vessel.

The system mainly consists of two mathematical-physical models:

1. The first model, called the **Initial Magnetic State Model**, is an inverse model that determines the initial magnetic state of the steel structure of a naval vessel. Such a model uses a large data set of (on-board) measurements of the magnetic field.
2. The second model, called the **Magnetic Signature Prediction Model**, predicts the change in the magnetic signature, based on on-board data such as magnetic measurements, ship's motion and location of the ship. The prediction of the magnetic signature is used for the reduction of the signature by the degaussing system algorithm.

The two models are represented in the Fig. 1.5 by larger red boxes. In the update-step of the degaussing currents, a more sophisticated minimization algorithm should be implemented to automate this process of minimizing the current magnetic signature.



Figuur 1.5: Concept of CLDG, version 2015.

## 1.6. ORGANISATION OF THE THESIS

The thesis is organised as follows. Chapters 3 to 6 are based on papers and hence some overlap is present. Therefore we have chosen to include in each chapter an abstract and a reference list with the corresponding literature that is used in that chapter.

Chapter 2 describes fundamental aspects of magnetism and its origin. It provides the reader with background information on the topic of magnetism. Important quantities and formulas that are used throughout the thesis are explained briefly. Chapter 3 deals with a literature study and assessment of a number of models that describe ferromagnetism. Experimental data is compared to the performance of these models to show resemblance in order to pick the best model for our closed-loop degaussing methodology. In Chapter 4 a magnetic susceptibility estimator in magnetostatics is proposed based on experimental data with an application of the adjoint method to speed up the performance of the involved optimisation algorithm. Chapter 5 proposes a parameter estimation method for the Jiles-Atherton model in weak fields. The method is tested on thin steel sheets. In Chapter 6 we propose a data-driven model for magnetostatics based on a simple data assimilation filter. The addition of data-assimilation allows the model to take into account changes in the permanent magnetisation, based on on-board measurements. Finally, Chapter 7 summarises the conclusions in this thesis and gives recommendations for further study.

## REFERENCES

- [1] S. Bobbio, G. Miano, C. Serpico and C. Visone. Models of Magnetic Hysteresis Based on Play and Stop Hysterons. *IEEE Trans. on Magn.*. Vol. 33, No. 6, November 1997.
- [2] O. Chadebec, J. L. Coulomb, J. P. Bongiraud, G. Cauffet, and P. Le Thiec. Recent improvements for solving inverse magnetostatic problem applied to thin shells. *IEEE Trans. Magn.*, vol. 38, no. 2, pp. 1005–1008, March 2002.
- [3] O. Chadebec, J. L. Coulomb, G. Cauffet, and J. P. Bongiraud. How to Well Pose a Magnetization Identification Problem. *IEEE Trans. Magn.*. vol. 39, no. 3, pp. 1634–1637, Mar. 2003.
- [4] Chatham House. International Law Applicable to Naval Mines. The Royal Institute of International Affairs, International Security Department. Workshop Summary. October 2014.
- [5] H. W. Engl, M. Hanke and A. Neubauer. Regularization of Inverse Problems. Mathematics and Its Applications, Vol. 375. Kluwer Academic Publishers. 2000.
- [6] G. Evensen. Data Assimilation: *The Ensemble Kalman Filter*. 2nd edition. Springer-Verlag New York. 2009.
- [7] P. C. Hansen. Discrete Inverse Problems: Insight and Algorithms. SIAM. Fundamentals of Algorithms. 2010.
- [8] Peace convention, 36 Stat. 2332; Treaty Series 541. The Hague, The Netherlands. October 18. 1907
- [9] P. C. Hansen and D. P. O’leary. The use of the L-curve in the regularization of discretization of discrete ill-posed problem. *SIAM. J. Sci. Comput.* Vol:14. pp. 1487–1503. 1993.
- [10] F. Henrotte and K. Hameyer. A Dynamical Vector Hysteresis Model Based on an Energy Approach. *Trans. on Magn.*. Vol. 42. No. 4. 2006.
- [11] John. J. Holme. Reduction of a Ship’s Magnetic Field Signatures. Morgan & Claypool publ. 2008.
- [12] A. Iványi (Ed.). Preisach Memorial Book. Akadémiai Kiadó. Budapest 2005.
- [13] D. Jiles and D. Atherton. Theory on Ferromagnetic Hysteresis, *Journal of Magnetism and Magnetic Materials* 61, Vol: 48. 1986.
- [14] M. Kachniarz, R. Szewczyk. Study on the Rayleigh Hysteresis Model and its Applicability in Modeling Magnetic Hysteresis Phenomenon in Ferromagnetic Materials. *Acta Physica Polonica A*. vol. 131. no. 5. pp. 1244-1249. 2017.
- [15] K. Kuhnen. Modeling, identification and compensation of complex hysteretic nonlinearities: A modified Prandtl-Ishlinskii approach. *Eur. J. Control.* Vol:9. pp:407–418. 2003.

- [16] V. François-Lavet, F. Henrotte, L. Stainier, L. Noels, and C. Geuzaine. An energy-based variational model of ferromagnetic hysteresis for finite element computations. *Journal of Computational and Applied Mathematics*. Vol: 246. pp 243-250. 2013.
- [17] E. Madelung. Über Magnetisierung durch schnellverlaufende Ströme und die Wirkungsweise des Rutherford-Marconischen Magnetdetektors. *Annalen der Physik. IV*.
- [18] T. Matsuo, D. Shimode, Y. Terade and M. Shimasaki. Application of Stop and Play Models to the Representation of Magnetic Characteristics of Silicon Steel Sheet. *IEEE Trans. on Magn.*. Vol: 39. No. 3. 2003.
- [19] T. Matsuo, Y. Terada, M. Shimasaki. Representation of minor hysteresis loops of a silicon steel sheet using stop and play models. *Phys. B.* Vol: 372. pp 25 – 29. 2006.
- [20] X. Brunotte, G. Meunier. Line Element for Efficient Computation of the Magnetic Field Created by Thin Iron Plates. *IEEE Trans. on Magn.*. Vol. 26. No. 5. 1990.
- [21] A. Morandi, M. Fabbri and P. L. Ribani. A Modified Formulation of the Volume Integral Equations Method for 3-D Magnetostatics. *IEEE Trans. on Magn.*. Vol. 46. No. 11. 2010.
- [22] L. Prigozhin *et al.* On the Energy-Based Variational Model for Vector Magnetic Hysteresis. *IEEE. Trans. on Magn.*. Vol. 52. No.12. 2016.
- [23] B. Szturomski. The Effect of an underwater explosion on a ship. *Scientific journal of Polish naval academy*. Vol. 2, No. 201. pp 57 – 73. 2015.
- [24] J. Tellinen. A Simple Scalar Model for Magnetic Hysteresis. *IEEE. Trans. on Magn.*. Vol. 34. No. 4. 1998.
- [25] E. Della Torre. *Magnetic Hysteresis*. Wiley-IEEE Press. 1999.
- [26] R. Wingo and M. H. Lackey. World Wide Permanent Magnetisation Changes on a Surface Ship. NATO Electromagnetic Silencing Symposium, Berlin 2003 (presentation).
- [27] A.R.P.J. Vijn. Inverse modeling for magnetic signature monitoring of naval ships. Master's thesis. University of Technology Delft. 2016.
- [28] Y. Vuillermet, O. Chadabec, J. L. Coulomb, J. P. Bongiraud, G. Cauffet and P. Le Thiec. Scalar Potential Formulation and Inverse Problem Applied to Thin Magnetic Sheets. *IEEE Trans. Magn.*. Vol. 44. No. 6. 2008.
- [29] S. E. Zirka *et al.*. On physical aspects of Jiles-Atherton models. *Journal of Applied Physics*. Vol: 112. 2012
- [30] S.E. Zirka, Y.I Moroz. Hysteresis modeling based on transplantation. *IEEE Trans. Magn.* Vol: 31, No: 31. pp: 3509—3511. 1995.
- [31] J. Ziske and T. Bödrich. Magnetic Hysteresis for Modelica. *Proceedings of the 9th International Modelica Conference*. 2012.

# 2

## A CRASH COURSE IN MAGNETISM

Magnetism<sup>1</sup> was discovered a very long time ago, even back to the Ancient period. Around 2000 BC, people noticed that lodestones (which are naturally magnetised pieces of mineral magnetite  $\text{Fe}_3\text{O}_4$ ) could attract iron. Such magnetised lodestones were used in the first simple magnetic compasses, by suspending the lodestone such it could rotate freely. In ancient Greece, Aristotle was one of the first philosophers that started a scientific discussion of magnetism, together with Thales of Miletus in the year 625BC to about 545BC. The word magnet stems from the Greek term *magnētis lithos*, which means “the Magnesian stone”. It is interesting to note that around the same time, Indian surgeon Sushruta already used magnets for surgical purposes.

All materials exhibit magnetism at some level, but the magnetic behavior depends on the electron configuration of atoms and the temperature. Therefore, in a macroscopic world, many materials do not show magnetic properties because the strength of the magnetisation is simply too weak to observe. Above the so-called *Curie temperature*, most material spontaneous lose their permanent magnetic properties; the magnetisation becomes unordered yielding a vanishing average magnetisation.

In this chapter, we briefly discuss the basic notions of magnetism. The notions of *magnetisation* and a *magnetic field* are introduced, and we discuss what causes magnetic fields in our physical world. The concept of *magnetic induction* or magnetic flux density, allows us to measure the effects of magnetism indirectly. After the introduction of what magnetisation is, we formulate the *Maxwell equations* that serve as fundamental laws for our work. By means of these equations, we are able investigate magnetic fields that stem from magnetisation distributions in magnetised bodies, even though in general descriptions of such magnetic fields are complex. It is worth mentioning that there are many well written books about magnetism, see for example books on (electromagnetism) by Jackson [2], Coey [1] and Zangwill [4]. This section is based on these books.

---

<sup>1</sup>source: <https://www.thoughtco.com/>

## 2.1. WHAT IS THE NATURE OF A MAGNETIC FIELD?

The magnetic field is the most fundamental idea in magnetism, and magnetism is caused by the electromagnetic force, which is one of the four fundamental forces along with the strong force that holds nuclei together, the weak force that controls the decay of unstable subatomic particles and the gravitational force between masses.

### MOVING ELECTRIC CHARGE

When an electric charge is moving, it generates a magnetic field perpendicular to the velocity vector of the electron or current. An example for which electrical charge is moving is a current in a wire. The magnetic force that exists due to charge in motion, can be explained by application of the relativistic Lorentz transformation to the Coulomb force between the charges. The magnetic force is therefore a relativistic one. Recall that when charges are at rest, the only force between the charges is the electrostatic Coulomb force. This force is described by Coulomb's inverse-square law and reads

$$F = k_e \frac{q_1 q_2}{r^2} \quad (2.1)$$

where  $k_e \approx 9 \cdot 10^9 \text{ Nm}^2\text{C}^{-2}$  is Coulomb's constant,  $q_1$  and  $q_2$  are the signed magnitudes of the charges and  $r$  is the distance between the charges in meters. The magnetic field can therefore be seen as a correction to the electrostatic Coulomb force.

### PERMANENT MAGNETS

In the case of a permanent magnet, there is no moving electrical charge on a macroscopic scale such as currents in wires or metal sheets. However, the orbital angular momentum and spins of electrons within the magnetic material (the so-called Amperian currents) lead to a net magnetisation within the geometry, and causes a magnetic field (outside the geometry). To illustrate the appearance of magnetisation due to orbital motion, consider the derivation of the magnetic moment of a single electron with charge  $-e$  in orbiting around in an hydrogen atom. Please refer to Fig. 2.1 for a sketch of the situation.

Consider a hydrogen atom positioned at the origin and suppose an electron is orbiting around the nucleus (in blue) in a circular orbit with a velocity of  $\mathbf{v}$  clock-wise; the charge of the nucleus is  $+e$ . The mass and charge of an electron and the Bohr radius<sup>2</sup> in a classical sense are given by

- $m_e := 9 \cdot 10^{-31} \text{ kg}$  (the mass of an electron)
- $e := 1.6 \cdot 10^{-19} \text{ C}$  (the charge of an electron)
- $R_{a_0} := 5 \cdot 10^{-11} \text{ m}$  (the Bohr radius of an hydrogen atom)

The electron causes an effective current  $I$  running counter-clockwise around the nucleus. The Coulomb force between the electron and the nucleus (2.1) is given by

$$F = k_e \frac{e^2}{4\pi R^2} \quad (2.2)$$

<sup>2</sup>The Bohr radius of an hydrogen atom is the most probable distance between the nucleus and the electron in a hydrogen atom in its ground state.

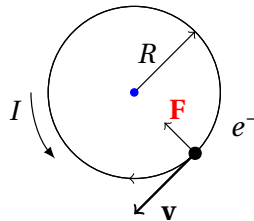
Observe that in this example the centripetal force  $F_c = \frac{mv^2}{R}$  equals the Coulomb force. Therefore the velocity  $v$  is computed through

$$F_c = F \quad \Leftrightarrow \quad k_e \frac{e^2}{4\pi R^2} = \frac{mv^2}{R} \quad \Rightarrow \quad v = \sqrt{\frac{k_e e^2}{4\pi m R}} \approx 2.3 \cdot 10^6 \text{ m/s} \quad (2.3)$$

Note that the velocity of the electron is small compared to the speed of light, therefore we may neglect any relativistic effects. Now that the velocity of the electron is known, the current that the electron induces is computed. Note that current is by definition the amount of charge per unit time, i.e.,  $I = \frac{e}{T}$ , where  $e$  is the charge of the electron and  $T$  is the period of the electron traveling a full orbit. Because the orbit is a circle with radius  $R$ , the period is  $T = 2\pi R/v \approx 1.4 \cdot 10^{-16}$  seconds. Therefore, the current produced by the single electron is given by  $I \approx 1.1 \cdot 10^{-3} \text{ A}$ , which is approximately 1 mA. Because there is a current in the circular loop, a magnetic moment  $\hat{\mu}$  is produced,  $\hat{\mu} = I\mathbf{A}$ , where  $\mathbf{A} = A\mathbf{n}$  is the vector area,  $A$  is the area of the circle and  $\mathbf{n}$  is the normal vector pointing upwards. The existence of such a magnetic moment is due to the law of Biot-Savart (see Section 2.2). The magnetic moment is given by

$$\mu = IA = (1.1 \cdot 10^{-3})(\pi R^2) = 9.3 \cdot 10^{-24} \text{ Am}^2 \quad (2.4)$$

In atomic physics this is called the Bohr magneton, denoted by  $\mu_B$ . To conclude that the angular momentum of an orbit is related to the magnetic moment, observe that  $\mathbf{L} = \mathbf{r} \times (m_e \mathbf{v})$  defines the angular momentum. We then may write [2, Chapter 5.6, page 148]  $\mu = \frac{q}{2m_e} \mathbf{L}$ , where the charge  $q = -e$  now has *negative* sign to correct the orientation of the angular momentum.



Figuur 2.1: An electron in an orbit.

In both cases, the magnetic field is generated in space. The magnetic field exerts a force on a moving charge called the *Lorentz force*. The Lorentz force, is the combination of the electric and magnetic force on a point charge. For a particle with charge  $q$  moving with a velocity in an electrical field  $\mathbf{E}$  and magnetic induction field  $\mathbf{B}$  the force that it experiences reads

$$\mathbf{F} = q\mathbf{E} + q(\mathbf{v} \times \mathbf{B}) \quad (2.5)$$

The above explanation is within a classical framework. However, magnetism is in fact a quantum-physical phenomenon. In the remaining chapter, it will become clear what we mean by a magnetic induction field  $\mathbf{B}$ . But first we discuss the magnetic field  $\mathbf{H}$  arising from a current in a wire, whose value is determined by the law of Biot-Savart.

## 2.2. BIOT-SAVART LAW

The law of Biot-Savart allows us to compute the magnetic field  $\mathbf{H}$  that is generated by an electrical current. Note that this law was merely a statement of experimental observation, first demonstrated by Ørsted, and that it may be derived from Ampere's law. In differential form, the law of Biot-Savart gives the field contribution  $\delta\mathbf{H}$  to the magnetic field  $\mathbf{H}$  generated by a current flowing through an infinitesimal length of a conductor. See Fig. 2.2. The magnetic field  $\delta\mathbf{H}$  is given by

$$\delta\mathbf{H}(\mathbf{P}) = \frac{1}{4\pi} J \left[ \delta\mathbf{l} \times \frac{\mathbf{P} - \mathbf{l}}{\|\mathbf{P} - \mathbf{l}\|^3} \right] \quad (2.6)$$

where  $J$  is the current in Amps flowing in an infinitesimal length  $\delta\mathbf{l}$ ,  $\|\mathbf{x}\| = \|\mathbf{P} - \mathbf{l}\|$  is the radial distance between the point of observation  $\mathbf{P}$  and the position of the infinitesimal length of a conductor  $\mathbf{l}$ . In its integral form, the law of Biot-Savart for the magnetic field  $\mathbf{H}(\mathbf{r})$  at the observation point  $\mathbf{P}$  reads

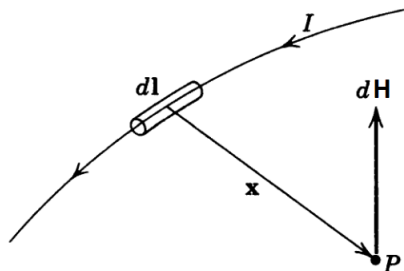
$$\mathbf{H}(\mathbf{P}) = -\frac{1}{4\pi} \int_{\gamma} J(\mathbf{l}) \left[ \frac{\mathbf{r} - \mathbf{l}}{\|\mathbf{P} - \mathbf{l}\|^3} \times d\mathbf{l} \right] \quad (2.7)$$

where  $\gamma$  describes the contour of the conductor. For a circular coil, the magnetic field produced by a running current is orthogonal to the cross section of the enclosed area. In Fig. 2.2, using the Right-hand rule, the orientation of the magnetic field is upward.

Consider the application of the Biot-Savart law for a circular coil of  $N$  turns with a radius of  $a$  meters. The coil is carrying a current of  $I$  amps. To find the magnetic field at the center, we divide the coil into  $n$  elements with arc length  $\delta\mathbf{l}$ . Note that  $(\delta\mathbf{l})_i \times \mathbf{l} = (\delta l)_i \mathbf{u}_z$ , where  $\mathbf{u}_z$  is the unit vector pointing in the  $z$ -direction. Furthermore, the total current flowing through the coil reads  $J = NI$  amperes. Applying the Biot-Savart law, we find the magnetic field

$$\mathbf{H} = \frac{NI\mathbf{u}_z}{4\pi a^2} \sum_{i=1}^n (\delta l)_i \rightarrow \frac{NI}{2a} \mathbf{u}_z \quad (\text{as } n \rightarrow \infty) \quad (2.8)$$

in Amps per meter. Observe that the magnetic field strength of a circular coil of  $N$  turns is directly proportional to both the current  $I$  and the number of turns  $N$ . This observation is crucial for designing *degaussing coils*.



Figur 2.2: The law of Biot-Savart. Here, the contribution  $d\mathbf{H}$  of a current  $I$  in an infinitesimal unit of length  $d\mathbf{l}$  to the magnetic field at location  $P$  is depicted. Source: [2].

## 2.3. DEFINITION OF THE MAGNETIC FIELD

Based on our previous finding for the magnetic field at the center of a circular coil with one turn, we define the unit of the magnetic field  $\mathbf{H}$ . The magnetic field has as unit **ampere per meter** [A/m], which is the magnetic field strength of 1 A/m that is produced at the center of a single circular coil of diameter 1 meter when it carries a current of 1A. Note that it is implicitly assumed that we work with (SI) units.

Note that in this definition the unit of the magnetic field is associated with a current. In subsection 2.1 it was observed that a magnetic field can also be produced without an effective current distribution, but rather by angular momentum of electrons. In table<sup>3</sup> 2.1 one can find the magnetic field strengths in various situations. It is worth noticing that Earth's magnetic field at the surface is relatively weak, of the order of 50 up to 100 A/m.

Field Strength [A/m]	Application
$10^{14}$	Surface of neutron stars
$10^8$	Implosive magnets (microsecond duration)
$2 - 5 \times 10^7$	Pulsed electromagnets (microsecond duration)
$1 - 3 \times 10^7$	High field electromagnets
$1 - 1.5 \times 10^7$	Superconducting magnets
$1 - 2 \times 10^6$	Laboratory electromagnets
$1 \times 10^6$	Strongest permanent magnets
$10^2$	Earth's magnetic field on the surface
10	Stray fields from electrical machinery
1	Urban magnetic noise level
$5 \times 10^{-2}$	Contours for geomagnetic anomaly maps
$10^{-4}$	Magnetocardiograms
$10^{-5}$	Fetal Heartbeat
$10^{-6}$	Magnetic field from human brain
$10^{-8}$	Limits of detection for superconducting quantum interference devices

Table 2.1: Magnetic field Strengths (A/m) in a variety of situations, showing a range of 19 orders of magnitude. Source: [3, Chapter 1, page 9].

## 2.4. MAGNETIC INDUCTION FIELD AND FLUX

To understand what a magnetic induction field is, we first discuss the discovery of Michael Faraday. He demonstrated the converse effect that Ørsted shown: varying magnetic fields induce electrical currents in a wire. Although at that time people were not impressed, this discovery was a crucial step to the development of generators and power plants. This principle of inducing electrical currents is called *magnetic induction*.

The magnetic induction field is a measure of how much magnetic field is “flowing” through a unit volume. In order to capture this idea, we have to generalize the notion of *flux*. Traditionally, flux is an important notion in, for example, flow theory. But in such cases, there are real particles such as sand or water molecules moving around, which inducing a flux. In the case of magnetism, there are no “magnetic particles” moving around, but still it

<sup>3</sup>table taken from [3], page 9.

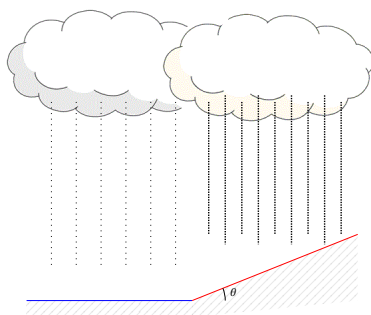


Figure 2.3: Example of flux

is interesting and important to think about such imaginary particles that are moving around due to the presence of a magnetic field.

As an illustration for traditional flux, we consider the situation where rain is falling vertically on two rectangular tiles (in a garden). For clarification, see Fig. 2.3. We ask ourselves how much rain hits this tile. This depends on three things, namely:

- the amount of rain falling per unit of time,
- the size of the tile,
- the orientation of the tile relative to the rain.

We consider each of these dependencies. If it rains is dense, then a lot of rain will hit a tile, and if it is raining weakly, then also a smaller amount of rain hitting a tile. Of course, if a tile is larger, then more rain will hit the tile compared with a smaller tile. Lastly, the orientation of the tile relative to the velocity of the rain plays an important role. In the extreme case that  $\theta = 90^\circ$ , then no rain will hit the tile, and for  $\theta = 0$  the amount of rain that hits the tile is optimal.

## 2.5. MAXWELL'S EQUATIONS

One of the greatest scientific breakthroughs in science was achieved in the nineteenth century, by the Scottish scientist James Clerk Maxwell (1831 - 1879). He combined the previously seemingly unrelated and mysterious phenomena of electricity, magnetism and (what is now known as) electromagnetic radiation together in a very elegant theory, following the work of Faraday, Ampère and Ørsted. The four coupled partial differential equations, known as Maxwell's Equations, describe the behaviour of electric and magnetic fields in both vacuum and matter:

$$\nabla \cdot \mathbf{D} = \rho$$

**Gauss' law:** electrical fields are produced by electrical charges

$$\nabla \cdot \mathbf{B} = 0$$

**Gauss' law:** there exist no magnetic monopoles

$$\nabla \times \mathbf{E} = -\frac{\partial \mathbf{B}}{\partial t}$$

**Faraday's law of induction:** changing magnetic fields produce electric fields

$$\nabla \times \mathbf{H} = \frac{\partial \mathbf{D}}{\partial t} + \mathbf{J}$$

**Ampère's law:** magnetic fields result from currents and changing electric fields

In these equations  $\mathbf{E}$  stands for the electric field intensity [V/m] and  $\mathbf{B}$  stands for the magnetic induction field intensity [T]. One observes two extra vector fields in the differential formulation of Maxwell's equations. These so-called auxiliary fields take physical matter into account and are defined as follows:

$$\mathbf{D} = \epsilon_0 \mathbf{E} + \mathbf{P}, \quad (2.9)$$

$$\mathbf{H} = \frac{1}{\mu_0} \mathbf{B} - \mathbf{M}. \quad (2.10)$$

The quantities  $\mathbf{D}$  [C/m<sup>2</sup>] and  $\mathbf{H}$  [A/m] stand for the electric and magnetic flux densities respectively. The electric charge density [coulomb/m<sup>3</sup>] is given by  $\rho$  and  $\mathbf{J}$  stands for the electric current density measured in [A/m<sup>2</sup>].

We see that in general the electric and magnetic fields are coupled by the above equations. We therefore speak of the electromagnetic field. When we assume that the fields are **static**, i.e., the fields do not change in time, then the four equations decouple into two sets of two equations that describe the electric field and the magnetic field. Assuming that there are no currents present ( $\mathbf{J} \equiv \mathbf{0}$ ), the *static magnetic field* is described by

$$\nabla \cdot \mathbf{B} = 0, \quad (2.11)$$

$$\nabla \times \mathbf{H} = \mathbf{0}, \quad (2.12)$$

$$\mathbf{B} = \mu_0 (\mathbf{H} + \mathbf{M}). \quad (2.13)$$

We call this set of equations the *magnetostatic field equations*. If the magnetisation of an object is prescribed, then these equations fully describe the resulting magnetic field, also called the *reduced magnetic field*. Throughout this thesis, these equations are used to model the magnetic state and magnetic signature of a naval vessel.

## 2.6. SOLVING THE MAGNETOSTATIC FIELD EQUATIONS

In this section the magnetostatic field equations are solved. The forward problem is the determination of the magnetic induction field  $\mathbf{B}$  that is produced by some *known* magnetization  $\mathbf{M}$  in a magnetised object  $\Omega$ .

This problem can be solved in two ways: by means of a scalar potential or via a vector potential. Here, we note that a scalar potential exist because  $\mathbf{H}$  is irrotational, and that a vector potential exists due to the solenoidal field  $\mathbf{B}$ . The Helmholtz theorem plays an important role in solving the forward problem.

Moreover, solving the magnetostatic field equations becomes much more complex when one also takes into account hysteresis. If an object is made from ferromagnetic material, then the response due to an external field is described by the magnetostatic field equations in an implicit way. This aspect is postponed to Chapter 3 and 6.

### 2.6.1. THE HELMHOLTZ THEOREM

The Helmholtz Theorem [4] states an important decomposition that holds for all (smooth) vector fields. If  $\mathbf{C}$  is a smooth vector field, then the vector field can be decomposed into the sum of two fields, namely

$$\mathbf{C} = \mathbf{C}_\perp + \mathbf{C}_\parallel, \quad (2.14)$$

where  $\mathbf{C}_\perp$  is divergence-free and  $\mathbf{C}_\parallel$  is an irrotational field. In particular the decomposed fields are (under suitable conditions) uniquely determined by a vector potential and scalar potential.

$$\mathbf{C}_\perp = \nabla \times \mathbf{F} \quad (2.15)$$

$$\mathbf{C}_\parallel = -\nabla\varphi \quad (2.16)$$

where the quantities  $\mathbf{F}$  and  $\varphi$  are given by

$$\mathbf{F}(\mathbf{r}) = \frac{1}{4\pi} \iiint_{\mathbb{R}^3} \frac{(\nabla' \times \mathbf{C})(\mathbf{r}')}{\|\mathbf{r} - \mathbf{r}'\|} d\Omega' \quad \text{and} \quad \varphi(\mathbf{r}) = \frac{1}{4\pi} \iiint_{\mathbb{R}^3} \frac{(\nabla' \cdot \mathbf{C})(\mathbf{r}')}{\|\mathbf{r} - \mathbf{r}'\|} d\Omega' \quad (2.17)$$

In other words, a smooth vector field is completely determined by the curl and divergence of the vector field.

### 2.6.2. SOLUTION BASED ON A SCALAR POTENTIAL

In the absence of a current density, the magnetostatic field equations can be solved via a scalar potential. The Helmholtz theorem can be used to derive an analytical expression for the scalar potential solution in terms of the magnetisation. Recall that in the absence of a current density, the magnetostatic field equations reads

$$\nabla \cdot \mathbf{B} = 0, \quad \nabla \times \mathbf{H} = \mathbf{0}, \quad \text{and} \quad \mathbf{B} = \mu_0(\mathbf{H} + \mathbf{M}) \quad (2.18)$$

Combining the first and third identity, we find that from  $\nabla \cdot \mathbf{B} = \nabla \cdot (\mu_0 \mathbf{H} + \mathbf{M}) = 0$  it follows that  $\nabla \cdot \mathbf{H} = -\nabla \cdot \mathbf{M}$ . The curl and divergence of  $\mathbf{H}$  are now known, therefore we can apply Helmholtz theorem on  $\mathbf{H}$  to find an analytical expression for  $\mathbf{H}$ . Note that in (2.17),  $\mathbf{F} = \mathbf{0}$  as  $\mathbf{H}$  is irrotational, which implies that  $\mathbf{H}_\perp = \mathbf{0}$ . In turn, the decomposition of Helmholtz for  $\mathbf{H}$  reduces to  $\mathbf{H} = \mathbf{H}_\parallel = -\nabla\varphi$ . Looking at  $\mathbf{H}_\parallel$ , we observe that the scalar potential in (2.17) can be expressed as follows:

$$\varphi(\mathbf{r}) = -\frac{1}{4\pi} \iiint_{\mathbb{R}^3} \frac{(\nabla' \cdot \mathbf{M})(\mathbf{r}')}{\|\mathbf{r} - \mathbf{r}'\|} d\Omega' \quad (2.19)$$

Thus, the divergence of the magnetisation serves as the source of the magnetic field. The magnetic field  $\mathbf{H}$  is now given by

$$\mathbf{H}(\mathbf{r}) = -\nabla \left( -\frac{1}{4\pi} \iiint_{\mathbb{R}^3} \frac{(\nabla' \cdot \mathbf{M})(\mathbf{r}')}{\|\mathbf{r} - \mathbf{r}'\|} d\Omega' \right). \quad (2.20)$$

In the next step, the expression for  $\mathbf{H}$  is simplified, this is done by switching the order of the differentiation and integration. Note that the  $\nabla$  operator only applies to  $\mathbf{r}$ , and so it is allowed to bring it inside the integral. Using the identity

$$\nabla \left( \frac{1}{\|\mathbf{r} - \mathbf{r}'\|} \right) = -\frac{\mathbf{r} - \mathbf{r}'}{\|\mathbf{r} - \mathbf{r}'\|^3}, \quad (2.21)$$

the final expression for  $\mathbf{H}$  is obtained, namely

$$\mathbf{H}(\mathbf{r}) = -\frac{1}{4\pi} \iiint_{\mathbb{R}^3} \frac{\mathbf{r} - \mathbf{r}'}{\|\mathbf{r} - \mathbf{r}'\|^3} (\nabla' \cdot \mathbf{M})(\mathbf{r}') d\Omega'. \quad (2.22)$$

Following [2, Section 5.9, page 197], it is convenient to further assume that magnetisation falls suddenly to zero on the boundary surface of the object  $\Omega$ . Using a pill-box argument, the magnetic surface-density

$$\sigma = \mathbf{n} \cdot \mathbf{M} \quad (2.23)$$

can be defined, where  $\mathbf{n}$  is a normal vector pointing outwards. Then the magnetic field can be written as

$$\mathbf{H}(\mathbf{r}) = -\frac{1}{4\pi} \iiint_{\Omega} \frac{\mathbf{r} - \mathbf{r}'}{\|\mathbf{r} - \mathbf{r}'\|^3} (\nabla' \cdot \mathbf{M})(\mathbf{r}') d\Omega' + \frac{1}{4\pi} \iint_{\partial S} \frac{\mathbf{r} - \mathbf{r}'}{\|\mathbf{r} - \mathbf{r}'\|^3} (\mathbf{n}' \cdot \mathbf{M})(\mathbf{r}') dS'. \quad (2.24)$$

Note that both domains of integration are now bounded subsets of  $\mathbb{R}^3$ . The magnetic induction field outside the magnetised object satisfies  $\mathbf{B} = \mu_0 \mathbf{H}$ , and thus reads

$$\mathbf{B}(\mathbf{r}) = -\frac{\mu_0}{4\pi} \iiint_{\Omega} \frac{\mathbf{r} - \mathbf{r}'}{\|\mathbf{r} - \mathbf{r}'\|^3} (\nabla' \cdot \mathbf{M})(\mathbf{r}') d\Omega' + \frac{\mu_0}{4\pi} \iint_{\partial S} \frac{\mathbf{r} - \mathbf{r}'}{\|\mathbf{r} - \mathbf{r}'\|^3} (\mathbf{n}' \cdot \mathbf{M})(\mathbf{r}') dS'. \quad (\mathbf{r} \notin \Omega) \quad (2.25)$$

In Chapter 4, a Method of Moments is derived on the basis of these expressions for the magnetic (induction) field.

### 2.6.3. SOLUTION BASED ON A VECTOR POTENTIAL

The magnetic scalar potential  $\mathbf{H} = -\nabla\varphi$  is not valid whenever a current density is present in the space of interest. A more general approach is then to exploit the divergence-free condition on  $\mathbf{B}$ . This approach also works in the absence of a current density.

The idea is to apply the Helmholtz theorem to the magnetic induction field  $\mathbf{B}$ . In (2.18) it is already given that  $\nabla \cdot \mathbf{B} = 0$ . To obtain an expression for  $\nabla \times \mathbf{B}$ , we combine the second and third identity to obtain  $\nabla \times \mathbf{B} = \mu_0 \nabla \times \mathbf{M}$ . Observe that in this case,  $\varphi = 0$  as  $\mathbf{B}$  is divergence-free. Thus,  $\mathbf{B} = \nabla \times \mathbf{F}$ . The vector potential  $\mathbf{F}$  immediately follows:

$$\mathbf{F}(\mathbf{r}) = \frac{\mu_0}{4\pi} \iiint_{\mathbb{R}^3} \frac{(\nabla' \times \mathbf{M})(\mathbf{r}')}{\|\mathbf{r} - \mathbf{r}'\|} d\Omega' \quad (2.26)$$

Hence, the magnetic induction field  $\mathbf{B}$  reads

$$\mathbf{B}(\mathbf{r}) = \frac{\mu_0}{4\pi} \nabla \times \iiint_{\mathbb{R}^3} \frac{(\nabla' \times \mathbf{M})(\mathbf{r}')}{\|\mathbf{r} - \mathbf{r}'\|} d\Omega' \quad (2.27)$$

In Chapter 6, this alternative expression is used to derive a Method of Moments for our Hybrid model.

## REFERENCES

- [1] J. M. D. Coey. Magnetism and magnetic materials. Cambridge University Press. 2009.
- [2] J. D. Jackson, *Classical Electrodynamics*, 3rd edition. New York: John Wiley & Sons. 1999.
- [3] D. Jiles, *Introduction to Magnetism and Magnetic Materials*, third edition. CRC Press. 2016.
- [4] A. Zwangwill. Modern Electrodynamics. 1st edition. Cambridge University Press. 2013.



# 3

## FERROMAGNETIC MODELS FOR MAGNETIC SIGNATURE PREDICTION: A STUDY TO SELECT THE RIGHT MODEL

*This chapter is based on:*

*Aad Vijn and Henk Jongbloed. Ferromagnetic Hysteresis Models for Magnetic Signature Prediction: a study to select the right model. Marelec Conference, Marine Biological Laboratory, Woodshole (Boston), 22-25 October 2019.*

### ABSTRACT

*The development of a closed-loop degaussing system for naval vessels requires modeling of the complex ferromagnetic behaviour of the steel structure of the ship. Our ambition is to describe the nonlinear hysteretic behaviour of the steel structure by means of a mathematical-physical model. A number of hysteresis models have been introduced in the past century. Examples of such hysteresis models are the mathematical model by Preisach, the quasi-physical model by Jiles and Atherton, the simplistic model by Lord Rayleigh and the more recent energy variational model that describes hysteresis by an energy minimisation. These models have shown their potential in the past year, but all have their own difficulties in delivering a complete description of vectorial ferromagnetic behaviour. In this chapter we give an overview of three of the above hysteresis models. In particular, we analyse these models by considering the model complexity, to what extent these models can be extended to incorporate properties such as inhomogeneity and anisotropy, the applicability of the model in large-scale applications, the (numerical) complexity of their computational burden, and their necessary parameter estimations. In addition, we illustrate the performance of these*

*models by numerical examples and we relate the above models to experimental data of a small scale ferromagnetic object.*

### 3.1. INTRODUCTION

To come up with an accurate model to predict the magnetic signature of naval vessels, the choice of a model that describes ferromagnetic behaviour is both interesting and important. From a theoretical point of view, there is an obvious need to describe ferromagnetic behaviour as complete as possible. However, such a model is (probably) very complex and increases the numerical burden of finite element implementations and thus predictions. Furthermore, the model should feed the degaussing-algorithm for the determination of optimal current settings in a fast and efficient way. Therefore, a trade-off between a sufficiently complete model and numerical aspects has to be considered.

This Chapter is structured as follows. Section 3.2 covers a brief explanation of ferromagnetism. In Section 3.3, four models that describe behaviour of ferromagnetism are discussed. In all four cases, we discuss the underlying assumptions that serve as the fundamentals for these models. It is important to notice that in this section we only consider behaviour at a *mesoscopic* level. This means that the behaviour is considered on a material level, and that no geometrical dimensions are considered. Therefore a demagnetising field introduced by a magnetised body is absent. Illustrations of hysteresis curves by these models are shown.

After the introduction of four models, we assess their strengths and weaknesses in Section 3.4. The main question that we will try to answer in this Chapter is:

*“Which model that describes ferromagnetic hysteresis for weak fields should we select as a basis for the development of closed-loop degaussing?”*

In fact, from the authors’ point of view, we will argue that the energy-variational model is potentially the best model to describe the ferromagnetic behaviour in weak fields regarding the hysteretic, anisotropic and numerical properties of the model.

In Section 3.5, we extend the hysteresis models by introducing a demagnetising magnetic field that arises from a ferromagnetic body and we illustrate the above-mentioned models in comparison with experimental data of a ferromagnetic scale object. We conclude this chapter with a discussion based on the central question in Section 6.11.

### 3.2. FERROMAGNETISM

In a nutshell, ferromagnetism means that there is a nonlinear relationship describing the response of ferromagnetic material to a changing magnetic background field. The origin of the word *hysteresis* traces back to the ancient Greek *hysteros* which means ‘later’, ‘second’ or ‘after’, and was later incorporated in the English language as ‘lagging behind’ or ‘shortcoming’. It was coined around 1890 by Sir James Alfred Ewing to describe the behaviour of magnetic materials [15]. Magnetic hysteresis implies that magnetisation is not only a result of the applied background field at this moment, but also depends on the history of the magnetic background field that preceded. This history-dependent aspect causes hysteresis to be an intriguing and complex phenomenon to describe.

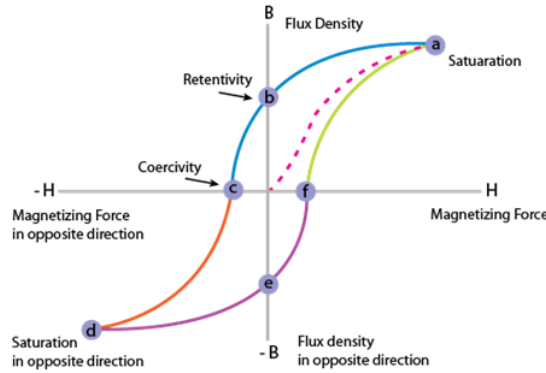


Figure 3.1: An example of a  $H-B$  hysteresis curve. In this figure, the major loop of the hysteresis curve is shown. Clearly, the nonlinearity can be observed if one considers the particular shape of the curve. The size of the area enclosed by the hysteresis curve shows how strong hysteresis effects are. If a hysteresis curve of a ferromagnetic material have a small coercivity value, then it is called a soft material. Such materials are easy to magnetise or demagnetise. On the contrary, hard materials have typically larger values of retentivity like permanent magnets. Furthermore, this also implies that the slope near the retentivity is small, therefore these materials keep their magnetisation for a long time, under varying magnetic conditions. Source: <http://electricalacademia.com/>

Magnetic hysteretic behaviour is dependent on many different material properties of the magnetisable material. Besides properties that describe the internal crystallographic structure of the material, other aspects such as temperature-dependence [21], frequency of alternating fields [17], and applied stress [5] are important.

The microscopic and mesoscopic origins of hysteresis can be explained by magnetic domain behaviour, which actually can be observed using an electron microscope, see Fig. 3.2. Details on the material properties due to ferromagnetism may be found in Coey [10] and Chikazumi and Charap [9]. Hysteretic behavior is the result of imperfections in crystalline structures on the nano- and microscale, giving rise to material anisotropy. The manufacturing process of real-life materials involves complicated and random processes, introducing certain distributions of mesoscopic magnetic domains inside a material, and mechanical stresses that are build up in the material giving rise to additional magneto-mechanical effects. Even more fundamental theory on the occurrence of magnetism may be found in a standard work on solid state physics and statistical thermodynamics.

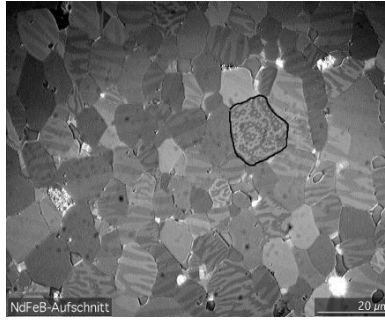
To model ferromagnetic behaviour based on these material-specific properties, one has to derive a macroscopic or mean-field description of the relation between different magnetic quantities. The basic constitutive equation

$$\mathbf{B} = \mu_0(\mathbf{M} + \mathbf{H}) \quad (3.1)$$

always holds. In order to be able to solve the Maxwell equations, an extra constitutive relation of the form

$$\mathbf{B} = \mathcal{F}(\mathbf{H}) \quad (3.2)$$

is required, which is well known in the literature to complete the set of PDE's for quantities  $\mathbf{B}$ ,  $\mathbf{H}$  and  $\mathbf{M}$ , see Jackson [14, Chapter 5]. For example, note that for paramagnetic material



Figur 3.2: An example of a distribution of magnetic domains within a piece of  $\text{Nd}_2\text{Fe}_{14}\text{B}$  alloy. source: [https://en.wikipedia.org/wiki/Magnetic\\_domain](https://en.wikipedia.org/wiki/Magnetic_domain).

this relationship is given by

$$\mathbf{M} = \chi \mathbf{H} \quad (3.3)$$

which describes the response of material to a present magnetic field, in terms of the *magnetic susceptibility*. Recall that the relative magnetic permeability  $\mu_r$  and the magnetic susceptibility  $\chi$  are related to each other through

$$\mu_r = 1 + \chi \quad (3.4)$$

and therefore these notions are interchangeable. In the case of ferromagnetic material, a constitutive relation such as stated in (3.2) cannot be found, because there is no one-to-one mapping between the internal fields  $\mathbf{H}$  and  $\mathbf{B}$ . Depending on the magnetic history, the relation between these fields change. Therefore, a hysteresis model is required to take ferromagnetism into account to solve the magnetostatic field equations. Different hysteresis models exist in the literature relating  $\mathbf{B}$ ,  $\mathbf{H}$  and  $\mathbf{M}$  and including the dependence on the magnetic history in some way. All models produce typical hysteresis curves as depicted in Fig. 3.1.

As shown in Fig. 3.1, there are a number of important values within the hysteresis curve that characterise the ferromagnetic behaviour of a material. Hilda Sung and Czeslaw Rudowicz [36] wrote a nice survey on the misconceptions and misinterpretations in textbooks regarding the interpretation of hysteresis curves. For example, Fig. 3.1 suggests that there is a saturation value for  $\mathbf{B}$  for sufficiently large values of  $\mathbf{H}$ . However, as the applied magnetic background field is further increased, the magnetic induction field also increases. This is a misconception, as only the magnetization of material saturates<sup>1</sup>. Furthermore, they give an extensive explanation in general of the notions of coercivity, retentivity and saturation in different hysteresis curves.

### 3.3. MATERIAL MODELS

In this section we introduce four different approaches to describe ferromagnetic behaviour. The four models are of increasing complexity and are defined by a number of material pa-

<sup>1</sup>Some papers indicate that after saturation, magnetisation of some materials can still increase in strong applied fields.

rameters. In each case, we should understand how the corresponding hysteresis curves look like. The models are described in the original papers by Rayleigh [34], Jiles and Atherton [15] and Bergqvist [3]. A discussion of these models follow in more detail, stating the main equations, considerations and (dis)advantages as well as model parameter estimation techniques. Furthermore, the approximation of magnetisation by an induced and permanent part (see Section 1.3.3) is also included as a model. Although this model does not describe hysteresis, it is a model that is often used to approximate magnetic behaviour, especially in weak background field conditions it approximates the ferromagnetic behavior to a certain accuracy.

First the model that considers magnetisation as the superposition of a linear part (induced magnetisation) and a constant offset (permanent magnetisation) is explained in Section 3.3.1. This is abbreviated as the **IP** model. Then, the order of complexity is increased by one and this leads to the model first proposed by Lord Rayleigh in Section 3.3.2, which is denoted by Rayleigh Model **RM**. Next, the well known hysteresis model by Jiles and Atherton is discussed in Section 3.3.3, which in principle describes also higher order terms of ferromagnetic behaviour and in particular is able to describe saturation values of magnetisation. The model of Jiles and Atherton will be denoted by **JA**. Finally, in Section 3.3.4 a more recently proposed model to describe ferromagnetic behaviour, using a energy-variational approach is explained. This is denoted by **EV**.

In the cases of the models **RM** and **IP**, we work towards a constitutive relationship for ferromagnetic behaviour that we can use to complete the magnetostatic equations; for **IP** this constitutive relationship is already given. In particular, we find expressions for the incremental permeability given by

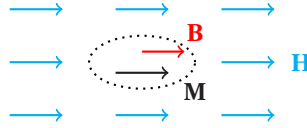
$$\frac{\partial \mathbf{B}}{\partial \mathbf{H}} = \mu(\mathbf{H} | \text{magnetic history}) \quad (3.5)$$

inside the material, where we assume that the magnetic history of the material is (partially) accessible. Here,  $H$  is the present magnetic field. At a material level, we could simply speak of the applied field (or effective field in the formulation of **JA**), but on a macroscopic scale the  $H$ -field must be interpreted as the internal field, in which a demagnetising field also plays an important role in describing coupling effects within a ferromagnetic body.

## ASSUMPTIONS

Throughout this chapter, the following assumptions hold:

- *Temporal behaviour of ferromagnetic material* is neglected, such as eddy currents, relaxation and magnetic viscosity. We only consider instantaneous relationships in ferromagnetic material;
- We do not consider any *geometrical dependencies*. This implies that there is no demagnetizing field present inside the material. Therefore, the magnetic field  $\mathbf{H}$  throughout this chapter equals the applied magnetic field;
- There is a *uniform applied magnetic field*  $\mathbf{H}_{app}$  present in the neighbourhood of an infinitesimal small unit volume of ferromagnetic material.



Figur 3.3: A grain of ferromagnetic material in a uniform applied magnetic field  $\mathbf{H} = \mathbf{H}_a$ .

- Due to the ferromagnetic behaviour, the material *responds* to the above-mentioned  $\mathbf{H}$ -field (by absorbing the energy that is produced by the work of the applied field) and introduces a magnetisation  $\mathbf{M}$  of the infinitesimal unit volume, and a magnetic induction field  $\mathbf{B}$  as a result of this response. These quantities are the output of our hysteresis models. Indeed, a magnetisation also introduces a magnetic distortion field, but for now we focus only on quantities  $\mathbf{M}$  and  $\mathbf{B}$ .

Although we do not consider geometrical dependencies, one could think that we consider a grain of ferromagnetic material as representation of a unit volume of ferromagnetic material, and that there is a net magnetisation  $M$ , magnetic field  $H$  and magnetic induction field  $B$  present within this grain. Such a grain is depicted in Fig. 3.3.

To describe the behaviour of large ferromagnetic structures, an extension with a finite element method (FEM) or boundary element method (BEM) is necessary. Such an extension is nontrivial and involves implicit relationships between the internal magnetic field  $\mathbf{H}_i$  and the internal magnetic induction field  $\mathbf{B}_i$ , namely described via the incremental magnetic permeability tensor quantity (3.5). The Method of Moments is a well known method in magnetostatics to describe in an explicit way how the applied magnetic background field and the magnetisation are spatially related. However, this is not trivial at all.

### 3.3.1. MODEL OF INDUCED AND PERMANENT MAGNETISATION (IP)

The simplest approach to describe ferromagnetic behaviour, which is well-known [13], is to approximate the nonlinear behaviour of ferromagnetism by a linearisation. We assume that the magnetisation  $\mathbf{M}$  can be split into two parts, the induced magnetisation ( $\mathbf{M}_{ind}$ ) and the permanent magnetisation  $\mathbf{M}_{per}$ :

$$\mathbf{M}[\mathbf{H}] = \mathbf{M}_{ind}[\mathbf{H}] + \mathbf{M}_{per}. \quad (3.6)$$

The induced magnetization is the linear response of the material to the present magnetic field  $\mathbf{H}$ . For this component we simply assume that the material behaves like *paramagnetic material*. For paramagnetic materials it holds that

$$\mathbf{M}_{ind} = \chi \mathbf{H}. \quad (3.7)$$

Here  $\chi$  is the magnetic susceptibility of the material. This quantity is actually a tensor, and depending on the entries of this tensor, one can describe either isotropic or anisotropic material. It is assumed that  $\chi$  is independent of  $\mathbf{H}$ .

The permanent part  $\mathbf{M}_{per}$  is the magnetization that is still present when there is no applied field. Traditionally, it is assumed that the permanent magnetisation does not change over time. In practice, this component paradoxically does change (slowly) over time. Therefore, **IP** entails a categorical error in describing ferromagnetic behaviour and is only applicable locally (close to the calibrated initial state of the model).

To illustrate the nature of the above separation of magnetisation into an induced and permanent magnetisation, observe the following reasoning. Consider the one-dimensional constitutive relationship between  $M$  and  $H$  and a Taylor expansion of  $M(H)$  about the point  $(H_0, M_0)$ . We find the following expansion:

$$M(H) \approx M_0 + \left. \frac{dM}{dH} \right|_{H=H_0} (H - H_0) + \text{h.o.t.} \quad (3.8)$$

When higher order terms (h.o.t.) are ignored it can be seen that indeed  $M(H)$  is linear around  $H = H_0$ . If one defines the magnetic susceptibility  $\chi$  by

$$\chi := \left. \frac{dM}{dH} \right|_{H=H_0} \quad (3.9)$$

then we may rewrite (3.8) as

$$M(H) \approx (M_0 - \chi H_0) + \chi H + \text{h.o.t.} \quad (3.10)$$

The magnetic susceptibility is a dimensionless material property that indicates the degree of magnetization in response to the applied field. A large value of  $\chi$  implies that many field lines are attracted by the material, resulting in a large induced magnetisation. Note that in (3.10) it follows that the magnetisation can be approximated by the sum of a constant component and a linear component. These observations and results from [35] support the assumption that the induced and the permanent magnetization can be considered separately.

To summarise the main features of the **IP** approach, we find that **IP**

- approximates the ferromagnetic behaviour by a linearisation, which is a rough approximation. It is expected that this approach only holds locally because for small variations the hysteresis effects are neglectable;
- is applicable to both isotropic and anisotropic material. However, calibrating the model to anisotropic material is complex and challenging. A sophisticated parameter estimation algorithm is required to obtain the tensor  $\chi$ , see [42].

Because the **IP** approach does not include any hysteresis effects, the model is neglected in the remaining part of this chapter.

### 3.3.2. RAYLEIGH HYSTERESIS MODEL (RM)

Rayleigh's hysteresis model approximates the nonlinear behavior of ferromagnetic materials in weak applied fields. The Earth magnetic field (up to approximately  $50\mu\text{T}$  in strength) is considered a weak field. Recall that in this thesis, the emphasis lies on modeling the magnetic signature of steel ships. Although the Earth magnetic field is considered weak, the internal magnetic fields in the steel structure of a ship are likely stronger due to the demagnetising field in the macroscopic structure and the presence of degaussing coils that produce strong magnetic fields in the vicinity of the steel structure. Therefore the applicability of the Rayleigh Model may not hold. In the case of higher field strengths, a different more general model such as the Jiles-Atherton model or the energy-variational model is required to describe the hysteresis effects. However, Rayleigh's model gives a fairly simple way to model the hysteresis effects by approximating branches of the hysteresis curve by quadratic functions.

### SCALAR RM EQUATIONS

The initial magnetisation curve of ferromagnetic material is given by

$$B(H) = \mu_0 \mu_i H + \mu_0 \alpha_R H^2 \quad \text{for } H > 0, \quad (3.11)$$

where  $\mu_0 = 4\pi \cdot 10^{-7} \text{ H/m}$  is the *vacuum permeability*,  $\mu_i$  is called the *initial relative permeability* and  $\alpha_R$  is called the Rayleigh constant. For negative values the initial magnetisation curve can be extended as an odd function because  $B(-H) = -B(H)$  holds. Both values can be found experimentally from the measured initial magnetisation curve.<sup>5</sup> The initial magnetization curve is based on following a linear dependence between  $\mu_r(H)$  and  $H$ , namely

$$\mu_r(H) = \mu_i + \alpha_R H. \quad (3.12)$$

The minor loops within the hysteresis curve are based on approximation by quadratic functions. More specifically, to include the dependence on the magnetic history, the modulus value of the field value  $H_m$  at the turning point of such branches is introduced.

The above considerations lead to the following set of equations that describe the increasing and decreasing branches within the hysteresis curve. For any *increasing branch* ( $H \nearrow H_m$ ) where the field strength increases we have

$$B(H) = \mu_0 \left[ (\mu_i + \alpha_R H_m) H - \frac{\alpha_R}{2} (H_m^2 - H^2) \right] \quad (3.13)$$

and for *decreasing branches* ( $H \searrow H_m$ ) where the field strength decreases we find that

$$B(H) = \mu_0 \left[ (\mu_i + \alpha_R H_m) H + \frac{\alpha_R}{2} (H_m^2 - H^2) \right]. \quad (3.14)$$

Whenever there is a change in sign in the change of the magnetic field, the hysteresis follows a new increasing or decreasing branch that is defined by the last field turning point  $H_m = H_{last}$ .

Along the increasing and decreasing branches, we may compute the incremental permeability. It follows that

$$\mu' = \frac{\partial B}{\partial H} = \begin{cases} \mu_0 [(\mu_i + \alpha_R H_m) - \alpha_R H] & (H \nearrow H_m) \\ \mu_0 [(\mu_i + \alpha_R H_m) + \alpha_R H] & (H \searrow H_m) \end{cases} \quad (3.15)$$

Note the change of signs in the above expressions for increasing and decreasing branches. Also, if  $H$  changes sign, then the incremental permeability makes a discontinuous jump in the model, which may lead to gaps in the minor branches. This behavior is not favorable. This problem is easily resolved when the Rayleigh model is defined as an ordinary differential equation and solved using a numerical scheme. Hence, we have found a constitutive relation for the incremental permeability that describes the hysteretic effect of ferromagnetism, which in turn can be coupled to a FEM/BEM to describe ferromagnetic behavior of larger structures.

### VECTORIAL EXTENSION OF RM

We propose the following vectorial extension of **RM**. Using the relationship  $B = \mu_0(H+M)$ , one is able to derive a  $M-H$  relation:

$$M(H) = \frac{1}{\mu_0} B(H) - H \quad (3.16)$$

$$= ((\mu_i - 1) + \alpha_R H_m) H \pm \frac{\alpha_R}{2} (H_m^2 - H^2) \quad (3.17)$$

for increasing or decreasing branches. Taking the partial derivative with respect to  $H$  while inserting the Rayleigh  $B-H$  relation yields for the increasing-decreasing branches:

$$\frac{\partial M}{\partial H} = \mu_i - 1 + \alpha_R H_m \pm \alpha_R H \quad (3.18)$$

(compare with 6.42), which is conveniently generalized to the incremental expression

$$d\mathbf{M} = \left( \underline{\boldsymbol{\mu}}_i - \underline{\mathbf{1}} + \text{diag}(\underline{\boldsymbol{\alpha}}_R \mathbf{H}_m) \right) d\mathbf{H} + \text{diag}(\underline{\boldsymbol{\alpha}}_R (\sigma(d\mathbf{H}) \otimes \mathbf{H})) \quad (3.19)$$

where  $\underline{\boldsymbol{\mu}}_i$  and  $\underline{\boldsymbol{\alpha}}_R$  are diagonal tensors that introduces anisotropy in the model,  $\underline{\mathbf{1}}$  is the identity tensor and  $\otimes$  denotes component-wise multiplication. This anisotropic extension only includes anisotropic behavior in the three independent principal directions. The reason for this is that one should give a meaning to the square of a magnetic field  $H^2$  in a vectorial sense. Furthermore,

$$\sigma(d\mathbf{H}) := \begin{pmatrix} \text{sgn}(d\mathbf{H}_x) \\ \text{sgn}(d\mathbf{H}_y) \\ \text{sgn}(d\mathbf{H}_z) \end{pmatrix} \quad (3.20)$$

which is a vector containing the sign of the change in magnetic field. The incremental expression (3.19) can be used to derive the Rayleigh incremental susceptibility

$$\underline{\boldsymbol{\chi}}_{RA} := \frac{\partial \mathbf{M}}{\partial \mathbf{H}} \quad (3.21)$$

which is a  $3 \times 3$  Jacobian matrix of the magnetisation. The incremental susceptibility is useful for modeling the magnetic behaviour of the ferromagnetic bodies in a FEM/BEM environment (see also formula (3.9) for a general definition of the susceptibility). To conclude this paragraph, we observe that the extension to a vectorial model necessarily introduces an increase of the number of material parameters. However, the number of parameters remains relatively small: only 6 parameters are required to describe vectorial behavior within the Rayleigh model.

### PARAMETER ESTIMATION FOR RM

In [34], a recipe for the identification of parameters of different materials is proposed on the basis of measuring pairs of values  $(H_m, B_m)$ , where

$$B_m = B_{incr}(H_m) = B_{decr}(H_m) = \mu_0(\mu_i + \alpha_R H_m) H_m \quad (3.22)$$

according to the Rayleigh model. Measuring different pairs of  $(H_m, B_m)$  and fitting them to (3.22) using a least squares approach, yields estimates for the parameters in the Rayleigh model. Useful strategies for estimating the Rayleigh parameters in the vectorial case could be:

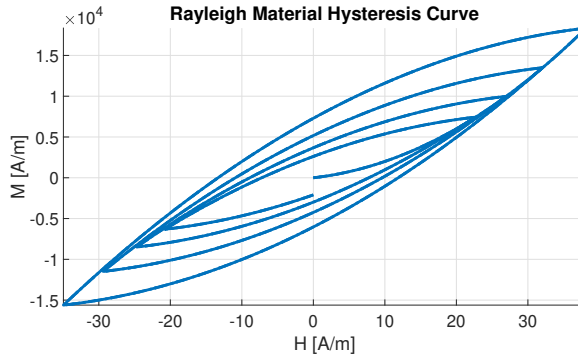


Figure 3.4: Example of a hysteresis curve within the Rayleigh Hysteresis Model. The curve is the result of a magnetic deperming signal for the applied background field  $H$ . Note that the resulting shape of the minor loop curves are quadratic. Therefore, such loops only represent hysteresis for weak applied fields  $H$ .

- Employing the approach above, under the assumption of sinusoidal driving field and isotropy.
- Using a gradient and/or adjoint approach to obtain some form of gradient-based error minimization.
- Using a smart genetic algorithm.

Since the Rayleigh model only has a relatively small number of parameters, the second approach could still be feasible. Since the model is also relatively computationally efficient, the genetic-algorithm approach could also result in a useful parameter estimation scheme.

#### EXAMPLE OF THE RM

To illustrate the performance of the Rayleigh Model, we consider the following scalar example depicted in Fig. 3.4. Here, we consider the following material parameters

$$\mu_i = 100 \quad \text{and} \quad \alpha_R = 10. \quad (3.23)$$

Note that these values do not necessarily represent a specific ferromagnetic material at hand, but were chosen such that the resulting hysteresis loop as shown in Fig. 3.4 is clearly interpretable. More realistic values for  $\mu_i$  and  $\alpha_R$  can be found in [19], where the authors found material parameters for **RM** for four different ferromagnetic materials.

Next, a sinusoidal deperming signal  $H_{dep}$  with decaying amplitude is used as input for **RM** to compute the response  $M$  of the model to this deperming signal. This results in higher-order reversal curves with 8 turning points, starting at the demagnetised state (the origin).

### SUMMARY OF RM

To summarise this paragraph:

- The Rayleigh model is a second order approximation of ferromagnetism, including quadratic descriptions of minor loops.
- Extensions to a vectorial model are possible, in which anisotropic descriptions of  $\mu_i$  and  $\alpha_R$  can be included. However, this is not yet investigated intensively in literature.
- Only a fairly small number of material parameters have to be determined to calibrate the model to experimental data.
- A number of estimation strategies can be used to find the material parameters based on experimental data.

### 3.3.3. JILES ATHERTON HYSTERESIS MODEL

The original **JA** model [15] is a pseudo-physics based scalar model, where some of the nonlinear phenomena of magnetic hysteresis are considered. These phenomena are the domain wall motion, rotation and bending, and magnetic moment interactions.

#### SCALAR JA EQUATIONS

Starting point is the theory of Langevin for paramagnetic materials, which is extended by Weiss to ferromagnetic materials. The original Langevin function is given by

$$\mathcal{L}(x) = \coth(x) - \frac{1}{x} \quad (3.24)$$

from which the anhysteretic magnetisation curve is derived:

$$M_{an}(H) = M_{sat} \mathcal{L}\left(\frac{H}{a}\right) = M_{sat} \left[ \coth\left(\frac{H}{a}\right) - \frac{a}{H} \right]. \quad (3.25)$$

The model is based on an effective field approximation. In the literature a lot of research can be found on the famous model of Jiles and Atherton, see for example [2, 6, 15, 16, 23–25, 27, 28, 30, 39, 44].

Weiss introduced the concept of “Molecular field” ( $H_M$ ), not to be confused with  $H_m$  in the Rayleigh model, in order to express the strong interaction between elementary moments in ferromagnetic material. He defined that  $H_M$  (an internal **fictitious** field) is directly proportional to  $M$ , which, in turn, adds to  $H$ . The effective field is given by:

$$H_e = H + H_M = H + \alpha M(H). \quad (3.26)$$

It is then assumed that the anhysteretic behavior is described by the Langevin’s function as function of the effective field  $H_e$ . The hysteresis behaviour is deduced from an energy balance, derived by Jiles and Atherton, between the magnetic energy supplied by an external source ( $M_{ext}$ ), the change in stored magnetostatic energy and the hysteresis loss, related to the irreversible magnetization  $M_{irr}$ . For initially demagnetized material ( $M_{ext} = M_{an}$ ), this balance reads

$$\mu_0 \int M_{an} \cdot dH_e = \mu_0 \int M \cdot dH_e + \mu_0 k(1-c) \int \delta \frac{dM_{irr}}{dH_e} \cdot dH_e \quad (3.27)$$

where  $k$  is the pinning parameter (due to pinning domain wall effect, as a consequence of material imperfections in its crystal structure), related to the energy dissipated due to hysteresis. Furthermore,  $\delta := \text{signum}(dH_e)$ . The value  $c \in [0, 1]$  is a measure for the reversible change of magnetization within the ferromagnetic material. Because we are considering quasi-static equilibrium conditions (there is still a time-dependence in the applied field), the energy losses occur only due to changes in  $M_{irr}$ . Considering the irreversible ( $M_{irr}$ ) and reversible ( $M_{rev}$ ) components of magnetization, we define

$$M = M_{irr} + M_{rev}. \quad (3.28)$$

If one differentiates the energy balance with respect to the effective field  $H_e$  we find

$$M_{an} = M_{rev} + M_{irr} + k(1-c)\delta \frac{dM_{irr}}{dH_e}. \quad (3.29)$$

If  $c = 0$  and  $M_{rev} = 0$  then we find that

$$M_{irr} = M_{an} - k\delta \frac{dM_{irr}}{dH_e}. \quad (3.30)$$

This leads to the following important description of reversible magnetization

$$M_{rev} = c(M_{an} - M_{irr}). \quad (3.31)$$

Bergqvist observed that whenever  $(M_{an} - M_{irr})dH_e < 0$  then there is no domain wall motion (displacement) and therefore  $dM_{irr} = 0$ . This implies that the differential equation for  $M_{irr}$  should be slightly modified into

$$dM_{irr} = \frac{1}{k\delta} [(M_{an} - M_{irr})dH_e]^+. \quad (3.32)$$

Here, the operator  $[x]^+$  is used to take into account the observation by Bergqvist and reads

$$[x]^+ = \begin{cases} x & \text{if } x \geq 0 \\ 0 & \text{if } x < 0 \end{cases}.$$

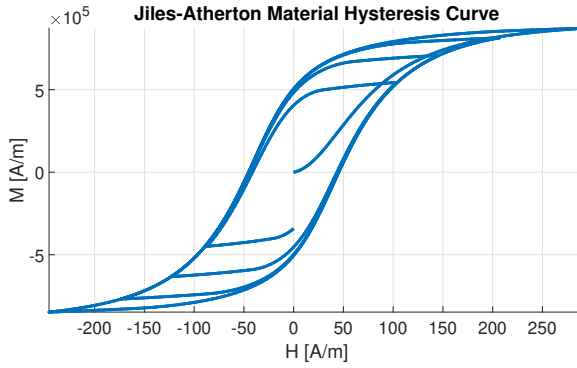
#### DERIVATION OF INCREMENTAL PERMEABILITY

We now derive a differential equation for  $M(H)$ , from which the incremental permeability follows directly. We start by looking at the differential

$$\begin{aligned} dM &= dM_{rev} + dM_{irr} \\ &= c(dM_{an} - dM_{irr}) + dM_{irr}. \\ &= cdM_{an} + (1-c)dM_{irr} \end{aligned} \quad (3.33)$$

Now combining (3.32) and (3.33) leads to

$$dM = cdM_{an} + \frac{1}{k\delta} [(1-c)(M_{an} - M_{irr})dH_e]^+. \quad (3.34)$$



Figur 3.5: Example of a hysteresis curve by the Jiles and Atherton Model. The curve is the result of a magnetic deperming signal for the applied background field  $H$ . Note that the applied signal is strong initially, and therefore the major loop of the hysteresis curve is visible.

Observe that, using (3.31), we may rewrite the second term in the RHS of (3.34) as

$$\begin{aligned}
 (1-c)(M_{an} - M_{irr}) &= M_{an} - M_{irr} + cM_{an} + cM_{irr} \\
 &= M_{an} - (M_{irr} + c(M_{an} - M_{irr})) \\
 &= M_{an} - (M_{irr} + M_{rev}) \\
 &= M_{an} - M
 \end{aligned} \tag{3.35}$$

Therefore (3.34) is equivalent to

$$dM = cdM_{an} + \frac{1}{k\delta} [(M_{an} - M)dH_e]^+ \tag{3.36}$$

Note that by the chain-rule and (3.26) we have that

$$\begin{aligned}
 dM_{an} &= \frac{dM_{an}}{dH_e} dH_e \\
 &= M'_{an}(H + \alpha M) (dH + \alpha dM)
 \end{aligned} \tag{3.37}$$

where  $M'_{an}(H + \alpha M) := \left. \frac{dM_{an}}{dH_e} \right|_{H_e=H+\alpha M}$ . For a further deduction we write (3.36) as

$$dM = c \frac{dM_{an}}{dH_e} (dH + \alpha dM) + \frac{1}{k\delta} [(M_{an} - M)(dH + \alpha dM)]^+ \tag{3.38}$$

We now focus on formula (3.38) and consider two cases as observed by Bergqvist.

*Case 1:* In the case that  $(M_{an} - M)dH_e > 0$ , formula (3.38) simplifies to

$$dM = c \frac{dM_{an}}{dH_e} (dH + \alpha dM) + \frac{1}{k\delta} (M_{an} - M)(dH + \alpha dM) \tag{3.39}$$

In equation (3.39) divide both sides by  $dH$  and use the result in (3.37) to obtain the following ODE for  $\frac{dM}{dH}$ :

$$\frac{dM}{dH} = \frac{cM'_{an}(H + \alpha M) + \frac{1}{k\delta}(M_{an} - M)}{1 - \alpha \left( cM'_{an}(H + \alpha M) + \frac{1}{k\delta}(M_{an} - M) \right)}. \quad (3.40)$$

Case 2: Developing (3.38) when  $(M_{an} - M)dH_e \leq 0$  gives

$$dM = c \frac{dM_{an}}{dH_e} (dH + \alpha dM) \quad (3.41)$$

using a similar reasoning we find the following ODE for  $\frac{dM}{dH}$ :

$$\frac{dM}{dH} = \frac{cM'_{an}(H + \alpha M)}{1 - c\alpha M'_{an}(H + \alpha M)}. \quad (3.42)$$

#### INCREMENTAL PERMEABILITY WITHIN THE JA MODEL

Based on the effective field description  $H_e$  one also introduces the corresponding effective magnetic induction field

$$B_e = \mu_0(H_e + M). \quad (3.43)$$

Taking the derivative with respect to the applied field yields

$$\frac{dB_e}{dH} = \mu_0 \left( 1 + (1 + \alpha) \frac{dM}{dH} \right). \quad (3.44)$$

We now **postulate** that the above-mentioned effective induction field  $B_e$  equals the magnetic induction field  $B$  within a material. We may therefore write

$$\mu = \frac{dB_e}{dH} = \mu_0 \left( 1 + (1 + \alpha) \frac{dM}{dH} \right). \quad (3.45)$$

Note that the incremental permeability may be computed solely in a numerical scheme to solve the differential equation for  $M(H)$ .

#### VECTORIAL EXTENSION OF THE JA MODEL

A vectorial Jiles-Atherton model was proposed by Bergqvist [2]. In this paper, Bergqvist first explained that there was an undesired behaviour present in the original model of Jiles and Atherton. He noted that, near turning points in high-order minor curves, the magnetisation and the magnetic field had opposite signs, and hence introduce an error in the model. This is easily resolved by introducing the positive-part operator as mentioned in (3.32). He

proceeds by considering the parameters  $c$  and  $k$ , from the original scalar JA, as symmetric tensors yielding the vectorial equation

$$d\mathbf{M} = \frac{\underline{\chi}_f}{\|\underline{\chi}_f\|} (\underline{\chi}_f \cdot d\mathbf{H}_e)^+ + \underline{c}\underline{\xi} d\mathbf{H}_e \quad (3.46)$$

where

$$\begin{cases} \underline{\chi}_f & := \underline{k}^{-1} (\mathbf{M}_{an}(\mathbf{H}_e) - \mathbf{M}) \\ \underline{\xi}_{ij} & := \frac{\partial \mathbf{M}_{an,i}}{\partial \mathbf{H}_{e,j}} \end{cases} \quad (3.47)$$

and the anhysteretic magnetisation reads

$$\mathbf{M}_{an}(\mathbf{H}_e) = M_s \left( \coth \frac{\|\mathbf{H}_e\|}{A} - \frac{A}{\|\mathbf{H}_e\|} \right) \frac{\mathbf{H}_e}{\|\mathbf{H}_e\|}. \quad (3.48)$$

From these two equations, any increment in  $\mathbf{M}$  can be computed from an increment in  $\mathbf{H}$ , the driving magnetic field. However, the above equation is implicit in case  $\underline{\alpha} \neq \mathbf{0}$ . Since  $d\mathbf{H}_e = d\mathbf{H} + \underline{\alpha} d\mathbf{M}$ , the quantity of interest  $d\mathbf{M}$  appears on both sides of the equation and should be solved in a ‘separation of cases’ or iterative way.

Another approach to a vectorial extension of the Jiles-Atherton model was given by Szymanski and Waszak [37]. Bergqvist does not address anisotropic materials explicitly and only considers uniaxial anisotropic materials. As a result, the number of parameters in the vectorial JA model by Bergqvist increases from 5 to a total of 15. Szewczyk [38] does give a full extension of the JA model. Note that each parameter involves a  $3 \times 3$  symmetric matrix. Hence, the full model is described by 30 parameters.

### STRATEGIES FOR PARAMETER ESTIMATION

Many different methods of finding the Jiles-Atherton material parameters exist in literature. The earliest parameter identification procedures were devised by Jiles and Atherton themselves. Thereafter, Jiles [16] proposed a parameter estimation method to estimate the parameters  $a, \alpha, k$  and  $c$  using readily available material properties. Based on the shape of experimental hysteresis curves, he managed to estimate the parameters with an error of only a few percent. Various intercepts and slopes (incremental susceptibility) were used in determining the parameters. However, this method relies on the choice of anhysteretic curve and is only applicable to material-isotropic materials.

Pop and Caltun [30] essentially perform the same procedure, with a very thorough description of their approach. Leite et al. [24] employed a genetic algorithm to obtain the classical Jiles-Atherton parameters. In their approach, the aim is to ensure minor loop closure when finding the parameters. This is done by the introduction of a dissipative factor  $R$ . During the parameter estimation, a number of minor loops are used to obtain the set of material parameters and an  $R - (H, B)$  relation, which indicates the difficulty of estimating the ‘variable’ parameter  $R$ . They used polynomial regression to obtain good results of the parameter fit.

Three other parameter estimation methods were found in literature. Firstly, a differential evolution algorithm was employed by Biedrzycki et al. [4], which gave good and efficient results, even in the anisotropic, vectorial case with 9 parameters. They describe

their method in detail. In his Msc. thesis, Olivier Baas [1] has fitted the Jiles-Atherton model to experimental data using the so-called ‘Shuffled Frog-Leaping Algorithm’, introduced in [27]. Lastly, an adjoint method of finding the parameters of the Jiles-Atherton model while incorporating the positive susceptibility criterion was proposed by Zaman et al. in 2016 [44]. This methodology allowed them to efficiently compute the gradient of the cost function with respect to the Jiles-Atherton parameters, and by employing a conjugate gradient-type algorithm, significantly lowered the computational time of arriving at optimal parameters.

3

### 3.3.4. ENERGY-BASED VARIATIONAL MODEL (EV)

Another approach, similar to **JA**, is to describe ferromagnetic behavior by the dissipation of energy based on a dry-friction representation. This approach leads to the energy-based variational model, which we will abbreviate by **EV**. This subsection is mainly based on the work of Leonid Prigozhin et al. We refer to [33] for more details and an in-depth analysis of anisotropic properties of the model. An explanation of the **EV** model below is also based on that paper. To ensure readability, the notation below coincides with [33].

#### MODEL EQUATIONS

Starting point is the first law of thermodynamics. The conservation of energy for magneto-statics states that the total energy is the sum of the empty space energy, depending on the magnetic field  $\mathbf{H}$  and the internal energy  $U(\mathbf{M})$ , determined by the magnetisation  $\mathbf{M}$ . This is captured by the following formula

$$W = \frac{1}{2} \mu_0 \|\mathbf{H}\|^2 + U(\mathbf{M}). \quad (3.49)$$

The change in empty space energy is  $\mathbf{H} \cdot \dot{\mathbf{B}}$ , where  $\mathbf{B}$  is the magnetic induction field. Furthermore, we assume that the change in internal energy can be written as  $\|r\dot{\mathbf{M}}\|$ , where  $r$  is some positive-definite friction tensor. Note that this assumption incorporates the dry-friction representation of the dissipation of energy. This approach was originally introduced by Bergqvist [3] to describe the dissipation of energy in material to ensure that minor loops are always closed. Hence, we write

$$\dot{W} = \mathbf{H} \cdot \dot{\mathbf{B}} + \|r\dot{\mathbf{M}}\|. \quad (3.50)$$

An important difference between the Jiles-Atherton model and the energy-based variational model is that here the magnetic field  $\mathbf{H}$  is written as the sum of two fields, namely a reversible magnetic field  $\mathbf{H}_r = \mathbf{f}(\mathbf{M})$  and an irreversible magnetic field  $\mathbf{H}_i = \mathbf{H} - \mathbf{H}_r$ . It is assumed that magnetic work is fully converted into internal energy, and therefore no internal energy dissipates. Dissipation of energy can be completely contributed to the irreversible field.

The separation law transforms the above equation (3.50) into an equation relating the irreversible magnetic field and the rate of change of magnetization.

$$\mathbf{H}_i \cdot \dot{\mathbf{M}} = \|k\dot{\mathbf{M}}\|. \quad (3.51)$$

Observe that in the isotropic case ( $k \in \mathbb{R}^+$ ), sufficient for equation (3.51) to be satisfied are

the following conditions on  $\mathbf{H}_i$  and  $\dot{\mathbf{M}}$ :

$$\begin{cases} (i) & \|\mathbf{H}_i\| \leq k \\ (ii) & \|\mathbf{H}_i\| < k \Rightarrow \dot{\mathbf{M}} = \mathbf{0} \\ (iii) & \dot{\mathbf{M}} \neq \mathbf{0} \Rightarrow \dot{\mathbf{M}} \parallel \mathbf{H}_i \end{cases} \quad (3.52)$$

Here, by  $\dot{\mathbf{M}} \parallel \mathbf{H}_i$  one means that  $\dot{\mathbf{M}} = a\mathbf{H}_i$  for some  $a \geq 0$ . The implication (3.52)  $\Rightarrow$  (3.51) is trivial in the case of  $\|\mathbf{H}_i\| < k$ . If  $\|\mathbf{H}_i\| = k$  and  $\dot{\mathbf{M}} \neq \mathbf{0}$ , we have  $\dot{\mathbf{M}} = a\mathbf{H}_i$  for some  $a > 0$  and thus

$$\mathbf{H}_i \cdot \dot{\mathbf{M}} = a\|\mathbf{H}_i\|^2 = ak^2 = k\|a\mathbf{H}_i\| = k\|\dot{\mathbf{M}}\| = \|k\dot{\mathbf{M}}\|, \quad (3.53)$$

which proves the implication. The ‘dry friction conditions’ (3.52) can be cast into a more convenient form with the help of some concepts from analysis.

Firstly, for a natural number  $n \in \mathbb{N}$  define the  $\mathbb{R}^n$ -closed ball  $\tilde{K} := \overline{B(0, k)} = \{\mathbf{u} \in \mathbb{R}^n : \|\mathbf{u}\| \leq k\}$  with the origin as center and radius  $k$ . Furthermore, define for any convex function<sup>2</sup>  $f : \mathbb{R}^n \rightarrow \mathbb{R} \cup \{\infty\}$  the *sub differential set* of  $f$  at the point  $\mathbf{x} \in \mathbb{R}^n$

$$\partial f(\mathbf{x}) := \{\mathbf{p} \in \mathbb{R}^n : (\forall \mathbf{y} \in \mathbb{R}^n) (f(\mathbf{y}) \geq f(\mathbf{x}) + \mathbf{p} \cdot (\mathbf{y} - \mathbf{x}))\} \quad (3.54)$$

This notion is an extension of the ordinary derivative of differential functions. To illustrate this concept, consider the function

$$g : \mathbb{R} \rightarrow \mathbb{R}, x \mapsto |x|. \quad (3.55)$$

Clearly, this function is not differentiable in  $x = 0$ . For any point  $x \neq 0$ , we easily find that the subdifferential coincides with the derivative. For  $x = 0$  we see that the subdifferential of  $f$  at point 0 is the interval  $[-1, 1]$ . To conclude

$$\partial g(x) = \begin{cases} \{-1\} & \text{if } x < 0 \\ [-1, 1] & \text{if } x = 0 \\ \{1\} & \text{if } x > 0 \end{cases} \quad (3.56)$$

The subdifferential set of any convex function is always closed and convex. Because we want to express the dry-friction conditions in mathematical terms so that we derive a way to test if these conditions are satisfied, we take a look at a modified indicator function. The subdifferential set of this function on the compact set  $\tilde{K}$ , defined by

$$I_{\tilde{K}}(\mathbf{x}) = \begin{cases} 0 & \text{if } \mathbf{x} \in \tilde{K} \\ \infty & \text{if } \mathbf{x} \notin \tilde{K} \end{cases} \quad (3.57)$$

is given by

$$\partial I_{\tilde{K}}(\mathbf{x}) = \begin{cases} \{\mathbf{0}\} & \text{if } \mathbf{x} \in \tilde{K}^o \\ \{\mathbf{ax} : a > 0\} & \text{if } \mathbf{x} \in \partial \tilde{K} \\ \emptyset & \text{if } \mathbf{x} \in \tilde{K}^C \end{cases} \quad (3.58)$$

<sup>2</sup>A function  $f : \mathbb{R} \rightarrow \mathbb{R}$  is *convex* if for any distinct two points  $x, y \in \mathbb{R}$ ,  $f(tx + (t-1)y) \leq tf(x) + (t-1)f(y)$  for any  $t \in [0, 1]$ .

where  $\tilde{K}^o = \{\mathbf{x} \in \mathbb{R}^n : \|\mathbf{x}\| < k\}$ ,  $\partial\tilde{K} = \{\mathbf{x} \in \mathbb{R}^n : \|\mathbf{x}\| = k\}$  and  $\tilde{K}^C = \{\mathbf{x} \in \mathbb{R}^n : \|\mathbf{x}\| > k\}$  are the interior, boundary and complement of set  $\tilde{K}$  respectively.

Indeed, for  $\mathbf{x} \in \tilde{K}^o$  we see that  $\mathbf{p} \in \partial I_{\tilde{K}}(\mathbf{x})$  if and only if  $\mathbf{p} \cdot (\mathbf{y} - \mathbf{x}) \leq 0$ . Obviously  $\mathbf{p} = \mathbf{0}$  works. If  $\mathbf{p} \neq \mathbf{0}$  then we find that for a sufficiently small number  $c \in \mathbb{R}$  the vector  $\mathbf{y} = c\mathbf{p} + \mathbf{x} \in \tilde{K}$  and

$$\mathbf{p} \cdot (c\mathbf{p} + \mathbf{x} - \mathbf{x}) = \mathbf{p} \cdot (c\mathbf{p}) = c\|\mathbf{p}\|^2 > 0$$

and therefore  $\mathbf{p} \neq \mathbf{0}$  is not an element of  $\partial I_{\tilde{K}}(\mathbf{x})$ . For  $\mathbf{x} \in \partial\tilde{K}$  we find that vectors of the form  $\alpha\mathbf{x} \in \partial I_{\tilde{K}}(\mathbf{x})$  for  $\alpha > 0$ . Indeed, if we take  $\mathbf{p} = \alpha\mathbf{x}$  for  $\alpha > 0$  then we find that  $\mathbf{p} \in \partial I_{\tilde{K}}(\mathbf{x})$  if and only if  $\mathbf{p} \cdot (\mathbf{y} - \mathbf{x}) \leq 0$ . Writing out this expression we find that this is equivalent to

$$\alpha [\mathbf{x} \cdot \mathbf{y} - k^2] \leq 0 \quad (3.59)$$

Because  $\mathbf{x}, \mathbf{y} \in \tilde{K}$  it follows from Cauchy-Schwartz that

$$\|\mathbf{x} \cdot \mathbf{y}\| \leq k^2$$

and hence (3.59) is satisfied for all  $\mathbf{y} \in \tilde{K}$ . Finally, whenever  $\mathbf{x} \notin \tilde{K}$  then it follows evidently that  $\partial I_{\tilde{K}}(\mathbf{x}) = \emptyset$  because  $f(\mathbf{x}) = +\infty$  and  $f(\mathbf{y}) = 0$  for all  $\mathbf{y} \in \tilde{K}$ .

Now, by (3.52) we have  $\mathbf{H}_i \in \tilde{K}$ . The dry friction law (3.52) can thus be conveniently expressed as

$$\dot{\mathbf{M}} \in \partial I_{\tilde{K}}(\mathbf{H}_i). \quad (3.60)$$

It was proven [26] that this characterization of the dry friction force follows from basic thermodynamic principles of admissible irreversible fields, which in retrospect justifies our postulation of the specific dry friction conditions (3.52). In the anisotropic case,  $k$  denotes a symmetric positive definite matrix, which is invertible. The  $k$ -dependent ball  $\tilde{K}$  is then generalised to

$$\tilde{K} := \{\mathbf{u} \in \mathbb{R}^n : \|k^{-1}\mathbf{u}\| \leq 1\} \quad (3.61)$$

With the above definition, (3.60) still holds in anisotropic material. The dry friction force conditions in the anisotropic case are:

$$\begin{cases} (i) & \|k^{-1}\mathbf{H}_i\| \leq 1 \\ (ii) & \|k^{-1}\mathbf{H}_i\| < 1 \quad \Rightarrow \dot{\mathbf{M}} = \mathbf{0} \\ (iii) & \dot{\mathbf{M}} \neq \mathbf{0} \quad \Rightarrow k\dot{\mathbf{M}} \parallel k^{-1}\mathbf{H}_i \end{cases} \quad (3.62)$$

where  $(k\dot{\mathbf{M}} \parallel k^{-1}\mathbf{H}_i)$  means that the change  $\dot{\mathbf{M}}$  is in the direction of  $\mathbf{H}_i$  (note that  $k$  is positive definite). This yields the variational inequality problem at time  $t$ :

$$\begin{aligned} \text{Find } \mathbf{H}_r \in \tilde{K}(t) \text{ such that for all } \mathbf{u} \in K(t), \\ (\nabla S(\mathbf{H}_r) - \overline{\mathbf{M}}) \cdot (\mathbf{u} - \mathbf{H}_r) \geq 0. \end{aligned} \quad (3.63)$$

Solving variational inequality problems can be challenging. However, using that  $\nabla S(\mathbf{u}) - \overline{\mathbf{M}}$  is integrable we find that a sufficient condition for  $\mathbf{u}^*$  to solve (3.63) is that it is the minimiser of the optimisation problem

$$\mathbf{H}_r(t) = \underset{\mathbf{u} \in K(t)}{\operatorname{argmin}} \{S(\mathbf{u}) - \overline{\mathbf{M}} \cdot \mathbf{u}\} \quad (3.64)$$

Indeed, to find the implication of (3.64) to (3.63) we note that the minimiser  $\mathbf{u}^*$  of the optimisation problem satisfies

$$\nabla(S(\mathbf{u}) - \overline{\mathbf{M}} \cdot \mathbf{u})|_{\mathbf{u}=\mathbf{u}^*} = \mathbf{0} \quad (3.65)$$

from which it immediately follows that  $\nabla S(\mathbf{H}_r) - \overline{\mathbf{M}} = \mathbf{0}$  and therefore (3.63) is satisfied by  $\mathbf{u}^*$ .

This minimization problem has a unique solution, provided that the derivative  $M'_{an} > 0$  on its domain. This is the case for any realistic anhysteretic curves, which is further substantiated by measurements and experimental data. Let us look more deeply into the minimization problem (3.64). The unconstrained problem

$$\mathbf{H}_r(t) = \underset{\mathbf{u} \in \mathbb{R}^3}{\operatorname{argmin}}\{S(\mathbf{u}) - \overline{\mathbf{M}} \cdot \mathbf{u}\} \quad (3.66)$$

is a minimiser at a point  $\mathbf{u} \in \mathbb{R}^3$  where the gradient

$$\nabla(S(\mathbf{u}) - \overline{\mathbf{M}} \cdot \mathbf{u}) = \nabla S(\mathbf{u}) - \overline{\mathbf{M}} = \mathbf{0}.$$

By definition, we have  $\mathbf{u} = \overline{\mathbf{H}_r}$ . If it is the case that this minimum is also contained in the interior of set  $K(t)$ , we have found our unique solution to the constrained minimization problem. So  $\mathbf{H}_r = \overline{\mathbf{H}_r}$ . Otherwise, the minimum is attained at the boundary of  $K(t)$  where it holds that  $\|k^{-1}(\mathbf{H}_r - \mathbf{u})\| = 1$ . This expression can be used to find the minimiser of the minimisation problem numerically [33]. Solving the minimisation problem (3.63) therefore leads to a new value for the magnetisation via

$$\mathbf{M} = \nabla S(\mathbf{H}_r) \quad (3.67)$$

in terms of a changing magnetic field  $\mathbf{H}$ . Further details on the numerical procedures to find solutions of the minimisation problem are omitted here, and the author refers to [33].

One of the elegant properties of the **EV** model is that the model is intrinsically vectorial and that the model describes change of magnetisation in terms of minimisation problems rather than PDE's. Although PDE's can be used to directly compute solutions, the minimisation alternative seems to reflect the very nature of ferromagnetism more precisely. In particular, the **principle of minimum energy** is a direct consequence of the second law of thermodynamics, and therefore it seems a good step to describe ferromagnetic behaviour using such energy minimisation principles.

### EV MODEL EXTENSIONS

It is stated in the paper that describing the change of magnetisation using the above methodology does not lead to a realistic hysteresis curve. Therefore, the authors introduce two essential modifications to the model:

- A *superposition of cells*, where each cell represents a part of the magnetisation based on a dry-friction tensor.

- The *effective field*  $\mathbf{H}_e = \mathbf{H} + \underline{\alpha}\mathbf{M}$  is introduced, bringing about an extra parameter  $\underline{\alpha}$ . This effective field is reminiscent of the effective field in  $\mathbf{JA}$ , and couples the total magnetization  $\mathbf{M}$  to the magnetic field, bringing about an interconnection between cells.

Each cell is assigned a cell magnetization  $\mathbf{M}_c^\ell$  and a weight  $\omega^\ell$ , where the cell magnetisation evolution is governed by the cell-specific friction coefficient. The total system magnetisation is then written as a linear combination of cell magnetisations:

$$\mathbf{M} = \sum_{\ell=1}^{N_c} \omega^\ell \mathbf{M}_c^\ell \quad (3.68)$$

One must thus keep track of all cell data during a simulation. The new magnetisation at each time step is now given by the above superposition, and the magnetic field  $\mathbf{H}$  in the above model derivation is replaced by the effective field  $\mathbf{H}_e$ , yielding the incremental formulation

$$\begin{cases} \mathbf{M}_{new} &= \sum_{\ell=1}^{N_c} \omega^\ell \mathbf{M}_c^\ell = \sum_{\ell=1}^{N_c} \omega^\ell \mathbf{M}_{an}(\|\mathbf{H}_r^\ell\|) \frac{\mathbf{H}_r^\ell}{\|\mathbf{H}_r^\ell\|} \\ \mathbf{H}_r^\ell &= \operatorname{argmin}_{\mathbf{u} \in K^\ell(t)} \{S(\mathbf{u}) - \mathbf{M}_{c,old}^\ell \cdot \mathbf{u}\} \\ S(\mathbf{u}) &= \int_0^{|\mathbf{u}|} M_{an}(s) ds \\ K^\ell(t) &= \{\mathbf{u} \in \mathbb{R}^3 : \|(\mathbf{k}^\ell)^{-1}(\mathbf{u} - \mathbf{H}_e^\ell)\| \leq 1\} \end{cases} \quad (3.69)$$

where the optimisation step can be done by gradient descent or Newton minimisation, by first writing the problem in an equivalent way using spherical coordinates. Furthermore, a choice for the description of the anhysteretic magnetisation  $\mathbf{M}_{an}$  has to be made. Popular choices are the arctangent or the Langevin-function. More recent research showed that the ‘‘anisotropic extension function-based model’’ for the anhysteretic magnetisation curve describes the anhysteretic behaviour in the best way [29].

#### EXAMPLE OF A HYSTERESIS CURVE USING THE ENERGY-VARIATIONAL MODEL

To illustrate the energy-variational model, we show hysteresis curves for different cells. Here, the values for the dry-friction tensors  $\underline{\mathbf{k}}_1, \dots, \underline{\mathbf{k}}_{N_c}$  are all diagonal and isotropic and linearly distributed in the range  $[0, k_m \alpha x]$ . Furthermore, the model weights are given by  $\omega^\ell = 1/N_c$  and  $N_c$  is varied per simulation.

#### STRATEGIES FOR PARAMETER ESTIMATION

In the Energy-Variational model as described by Prigozhin et al. [33], parameter estimation was performed as follows. Under the assumption of material isotropy, a known anhysteretic curve and an assumed linear distribution of  $N = 41$  friction parameters  $k_1, \dots, k_N$ , only the  $N = 41$  weights  $\omega_1, \dots, \omega_N$  had to be estimated. In their procedure, Prigozhin et al. used a cubic spline function as an approximation to the anhysteretic function. By performing several experiments, the anhysteretic curve and the coupling parameter  $\alpha$  could be estimated. Next, a three-level Matlab algorithm was implemented to estimate the weights  $\omega_j$ . In three nested algorithm steps, a least squares-error was minimized using intrinsic Matlab functions. That way, the anhysteretic curve, the value of  $\alpha$  and the weights were estimated

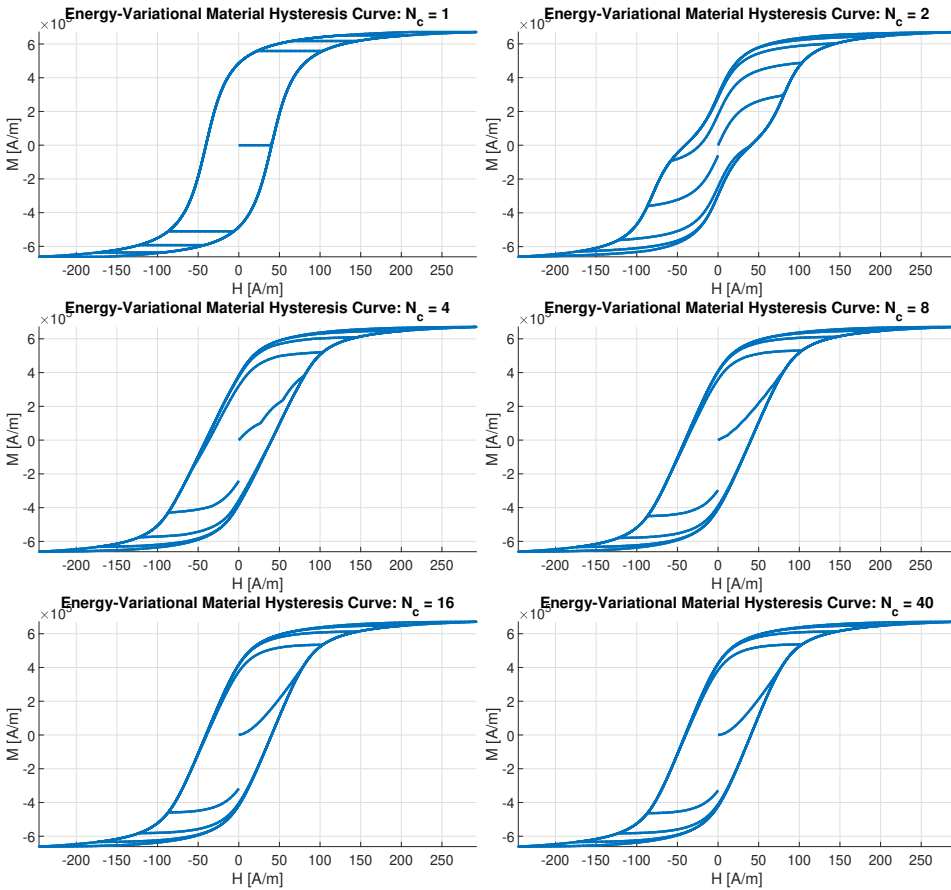


Figure 3.6: Energy variational hysteresis model for various numbers of cells. Note that the number of cells have a direct influence on the shape of minor loops and (higher-order) reversal curves. As the number of cells grows, these curves become more smooth and regular.

using a set of experimental ‘FORCs’ (First-Order Reversal Curves). This is a promising and straightforward approach for parameter estimation, it yielded excellent results on real material [33].

### 3.4. ASSESSMENT OF HYSTERESIS MODELS

In this section we assess the three candidates of models that describe ferromagnetic behaviour. To compare the three models, a list of criteria is defined which can be found in Table 3.1. We will discuss each criterion separately and see how the models compare to each other.

	<b>IP</b>	<b>RM</b>	<b>JA</b>	<b>EV</b>
<b>Orders of physics included</b>	1st order	2nd order	∞th order	∞th order
<b>Temperature dependencies</b>	No	No	Yes	Yes
<b>Hysteresis behaviour</b>	No	Yes	Yes	Yes
<b>Anistropy extensions</b>	Yes	Yes	Yes	Yes*
<b>Number of parameters (scalar)</b>	1	2	5	$2 + 2N_C$
<b>Coupling to FEM</b>	Easy	Moderate	Moderate	Hard
<b>Nonlinear Coil effects possible?</b>	Yes	Yes	Yes	Yes
<b>Computational burden</b>	low	limited	high	very high

Table 3.1: Assessment of four models for ferromagnetic behaviour. \*Note that the **EV** model is intrinsically anisotropic.

3

### 3.4.1. NUMBER OF FREE PARAMETERS

Looking at the three discussed models, it is clear that **EV** is the most complex out of the three, followed by the **JA** model. **RM** is the simplest, but also the most inflexible; it is furthermore only applicable at low to moderate magnetic field strengths. This can be a considerable drawback within the framework of closed-loop degaussing, where strong magnetic fields are often present locally. **RM** and **JA** are both scalar in nature, whereas **EV** is intrinsically vectorial. It is important to grasp this distinction, which can also be understood in the following way. Suppose all tensor parameters of the vectorial hysteresis models are taken isotropic, i.e. of the form  $\underline{\theta} = \gamma \underline{\delta}$ , where  $\gamma \in \mathbb{R}$  and  $\underline{\delta}$  is the unit tensor. Starting from a nonzero initial condition and applying only a magnetic field in (for example) the  $x$ -direction, in the case of **RM** and **JA** only yields a change in  $\mathbf{M}$  in the  $x$ -direction. However, if the applied field is strong enough, **EV** also yields changes in  $\mathbf{M}$  in the  $y$  and  $z$  directions, due to intrinsic anisotropy in the **EV** model.

In terms of the exact number of free scalar parameters, the following holds: Since all tensors in the hysteresis models are physically required to be symmetric and positive definite, a general  $3 \times 3$  hysteresis tensor consists of 6 free scalar parameters. Now we consider each of the models and identify how many free parameters in the vectorial anisotropic case are actually present:

- The original **RM** has 2 parameters. The three-dimensional **RM** model replaces the two scalar parameters by two (symmetric) tensors, increasing the number of parameters to 12. The quantity  $\mathbf{H}_m$  is not really a parameter, but rather a property and consequence of the applied field.
- The original **JA** has 5 parameters. Not all these parameters are transformed to vectors or tensors in the vectorial case. Bergqvist [2] indicates that in the vectorial case, the parameters  $\alpha$ ,  $k$  and  $c$  become symmetric tensors, bringing the total number of parameters to 20. As [38] indicates, the anhysteretic curve parameters can also be taken anisotropic, introducing the two parameter vectors  $a = (a_x a_y a_z)$  and  $M_s = (M_{sx} M_{sy} M_{sz})$ . Furthermore, the minor loop closure parameter  $R$  needs to be estimated for any minor loop, making it a ‘pseudo-parameter’, comparable to but more complex than  $H_m$  in the **RM**. All in all, 24 free scalar parameters are needed for the fully anisotropic **JA**.
- **EV** has two anhysteretic curve-vectors, just as the **JA** model. The effective field para-

meter  $\underline{\alpha}$  introduces another 6 free parameters. When  $N_c$  pseudo-particles are used in modeling the hysteresis behavior,  $N_c$  weights and  $6N_c$  scalar friction parameters are needed, bringing the total number of free scalar parameters to  $12 + 7N_c$ .

### 3.4.2. COMPUTATIONAL COMPLEXITY

In terms of computational complexity, the following can be stated. Firstly, let us consider the material case, in which no demagnetization fields or geometrical considerations play a role. When written in incremental form, a step of the **RM** can be taken by firstly checking the sign change of the driving magnetic field. Thereafter, the incremental susceptibility is given by a simple function of  $\mathbf{H}$  and the change  $\dot{\mathbf{H}}$  in time. The values for  $\mathbf{H}_m$  need to be stored. Roughly the same can be said about **JA**, however, the anhysteretic function and its derivatives must be evaluated a considerable number of times, yielding larger computation time. In contrast, both of these models are vastly more computationally efficient than **EV** which, in order to find a new value for the magnetization, needs to solve a nonlinear minimization problem  $N_c$  times (on average); this depends on whether irreversible changes occur in the magnetisation in **EV**. In all these hysteresis models, the value of the ‘new’ magnetization is only dependent on the previous state. However, storing the previous model state is much more expensive in **EV** than in **RM** and **JA**, which can be a model choice consideration in large-scale simulations. Loosely speaking, this ‘Markov property’ is in contrast to for example the Preisach model, in which all previous model states have to be taken into account.

Secondly, for large magnetic simulations on a macroscopic scale, a Finite Element of Boundary Element approach can be taken. Focusing on the FEM for now, one can say that the numerical complexity of material models can roughly be multiplied by the number of ferromagnetic material nodes in the finite element mesh, thus scaling the model time accordingly to the dimensions of the spatial discretisation in the FEM environment. In addition, all of these models are cast in either incremental or forward form, which is convenient when large magnetic simulations are integrated using a numerical scheme. However, in the case of **JA** and **EV**, an extra internal iterative scheme is necessary to impose extra numerical stability to ensure inner convergence of the models.

### 3.4.3. PARAMETER ESTIMATION OF MODELS

In the previous section, we have discussed the complexity of finding the correct material parameters based on measurement data. It was stated that the parameter estimation for **RM** and **JA** is well known and many parameter estimation methods are proposed in the literature. However, for the more recent energy-variational model, **EV**, little is known about how to effectively compute the material parameters. The authors have a need to develop such a parameter estimator in the near future. One of the open problems is how to compute the anisotropic material parameters from measurement data. What measurement data is required to obtain anisotropic parameter values, and is it even observable in measurement data alone?

We conclude that, based on the assessment, the energy-variational model is very promising, but requires additional research to define parameter estimations and to understand its predictive power.

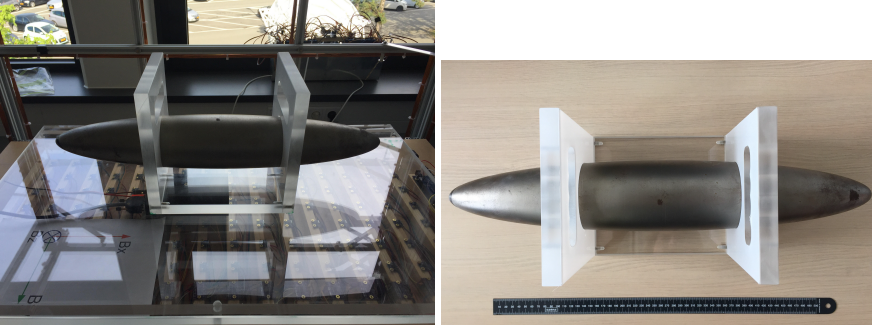


Figure 3.7: A steel prolate spheroid above the sensor-array and a top view of the ellipsoid. The solid spheroid is 580 mm long along the main axis and 95 mm in diameter along the two minor axes. It is placed inside a coil system that is used to change the local applied magnetic field and is placed 56 mm above the sensor array. The global coordinate frame is indicated on the A4 paper. To measure the magnetic induction field, HMC5983 Triple Axis Compass magnetometers are used. Depending on the set gain, the sensor noise is approximately  $1 \mu\text{T}$  up to  $3 \mu\text{T}$ . Higher gains are used to measure stronger fields, but also introduce a lower signal-to-noise ratio.

### 3.5. COMPARISON OF MODELS TO EXPERIMENTAL DATA

In this last section, we compare the above-mentioned material hysteresis models to experimental data of a case study. In the experiment, we have used a steel prolate spherical ellipsoid as a ferromagnetic body. The solid steel prolate spheroid is 580 mm long along the main axis and 95 mm diameter along the two minor axes. In Fig. 3.7 a picture of this ellipsoid can be found. The prolate spheroid provides an excellent starting point for investigating magnetic hysteresis since a perfect analytical solution for its magnetic field exists.

#### 3.5.1. DEMAGNETISATION FACTORS OF A GENERAL ELLIPSOID

As was briefly discussed Section 3.2, ferromagnetic material can be viewed as consisting of a large collection of micro- or mesoscopic magnetic domains. Locally and averaged over time (neglecting Barkhausen fluctuations), the magnetization due to an applied field can be assumed constant over those subdomains. The net magnetization ‘creates’ small dipoles inside the material, in turn causing a nonzero magnetic field. The magnetic field *inside* a magnetic material, which is thus a consequence of the applied field and magnetization, is in general a complicated function of the geometry of the object, the magnetization distribution and the applied field itself. With this in mind, writing the magnetic field inside a material *locally* as a sum of the applied field  $\mathbf{H}_a(\mathbf{r})$  and the ‘magnetization-caused’ field  $\mathbf{H}_M(\mathbf{r})$ , which is justified by the superposition principle, one can write

$$\mathbf{H}(\mathbf{r}) = \mathbf{H}_a(\mathbf{r}) + \mathbf{H}_M(\mathbf{M}(\mathbf{r}), \mathbf{r}) \quad (3.70)$$

which always holds true. It is also true that (locally speaking)  $\mathbf{H}_M(\mathbf{0}, \mathbf{r}) = \mathbf{0}$ . Now, expanding the magnetization-caused field to first order in  $\mathbf{M}(\mathbf{r})$  yields

$$\mathbf{H}_M(\mathbf{M}(\mathbf{r}), \mathbf{r}) = \mathbf{H}_M(\mathbf{0}, \mathbf{r}) + \frac{\partial \mathbf{H}_M(\mathbf{0}, \mathbf{r})}{\partial \mathbf{M}} \mathbf{M}(\mathbf{r}) + h.o.t. \quad (3.71)$$

$$= \frac{\partial \mathbf{H}_M(\mathbf{0}, \mathbf{r})}{\partial \mathbf{M}} \mathbf{M}(\mathbf{r}) + h.o.t. \quad (3.72)$$

$$(3.73)$$

Defining the *local demagnetization tensor* as

$$\underline{\mathbf{N}}(\mathbf{r}) := -\frac{\partial \mathbf{H}_M(\mathbf{0}, \mathbf{r})}{\partial \mathbf{M}}, \quad (3.74)$$

one observes that the magnetic field inside any magnetized material may be written out locally as

$$\mathbf{H}(\mathbf{M}(\mathbf{r}), \mathbf{r}) = \mathbf{H}_a(\mathbf{r}) + \mathbf{H}_M(\mathbf{M}(\mathbf{r}), \mathbf{r}) \quad (3.75)$$

$$= \mathbf{H}_a(\mathbf{r}) - \underline{\mathbf{N}}(\mathbf{r})\mathbf{M}(\mathbf{r}) + h.o.t. \quad (3.76)$$

Having obtained the nomenclature ‘demagnetization tensor’, the following important result can be stated.

**Theorem [Osborn (1945)].** If a (degenerate) ellipsoidal body is placed in a uniform background field  $\mathbf{H}_a$  and is uniformly magnetized with magnetization  $\mathbf{M}$ , the demagnetization field  $\mathbf{H}_M$  is also uniform. Furthermore, the demagnetization tensor is diagonal and constant across the ellipsoid, with elements that can be calculated explicitly from the ellipsoidal dimensions only:

$$\mathbf{H} = \mathbf{H}_a - \underline{\mathbf{N}}\mathbf{M} \quad (\text{inside the ellipsoid}) \quad (3.77)$$

The diagonal entries of this particular demagnetization tensor are called *demagnetization factors* and an important relationship for these diagonal entries is that in the SI-system,

$$N_{xx} + N_{yy} + N_{zz} = 1. \quad (3.78)$$

The magnetic field inside the ellipsoid is thus uniform. Also,

$$\mathbf{H}(\mathbf{r}) = A(\mathbf{r})\mathbf{M} \quad (\text{outside the ellipsoid}) \quad (3.79)$$

where  $A(\mathbf{r})$  is a  $3 \times 3$  matrix with entries solely depending on the geometry of the ellipsoid and  $\mathbf{r}$ . An analytical expression for  $A(\mathbf{r})$  can be found in [1, Appendix A.3].  $\square$

The above-mentioned theorem is taken from J.A. Osborn [31]. Note that the theorem states an equivalence between (3.76) and (3.77) for which all higher order terms vanishes.

It was Siméon Poisson who already showed that any resulting magnetisation of such an homogeneous ellipsoid in a uniform background field is uniform, but Osborn computed

the resulting demagnetisation factors in an analytical way using expressions in terms of elliptical integrals by Poritsky. In fact we have for prolate spheroids that

$$N_{xx} = \frac{1}{m^2 - 1} \left( \frac{m}{\sqrt{m^2 - 1}} \log \left( m + \sqrt{m^2 - 1} \right) - 1 \right) \quad (3.80)$$

$$N_{yy} = \frac{m}{2m^2 - 2} \left( \frac{m - 1}{\sqrt{m^2 - 1}} \log \left( m + \sqrt{m^2 - 1} \right) \right) \quad (3.81)$$

$$N_{zz} = N_{yy} \quad (3.82)$$

for which  $m = \frac{l}{d}$  where the polar radius  $l$  is greater than the equatorial radius  $d$  ( $l > d$ ). The resulting general analytical expressions for the demagnetisation factors in terms of the radii of the three principal axes are expressed in [31] and a number of tables for demagnetisation factor values are found for prolate and oblate spheroids. Note that for a sphere the demagnetisation factors are

$$N_{xx} = N_{yy} = N_{zz} = \frac{1}{3}$$

using a symmetry argument and the fact that the factors sum up to one. This implies that the internal demagnetising field for a sphere is relatively strong in each direction.

### 3.5.2. MEASUREMENT DATA OF STEEL ELLIPSOID

Returning to our setup and steel ellipsoid, we can determine the demagnetisation factors based on the expressions in [31]. We find that for our ellipsoid we have that

$$N_{xx} \approx 0.0443, \quad \text{and} \quad N_{yy} = N_{zz} \approx 0.4778. \quad (3.83)$$

Based on these values, we observe that the demagnetising field is relatively small in the longitudinal direction, while the field is ten times stronger in the other two principal directions. As a direct consequence we find that nonlinear hysteresis effects are more visible in the longitudinal direction than in the other directions. We will see that this is observed in the measurement data too.

We have collected a dataset of magnetic measurements by varying the magnetic background field in a prescribed scenario, as depicted in Fig. 3.8 in the top-left corner. Initially the magnetic background field was cancelled out, then the background field was varied along the three principal directions  $x$ , and  $z$ . After that, the field is rotated successively in the  $x - y$ ,  $y - z$  and  $x - z$  plane.

The magnetic field is measured at the sensor array in all 121 magnetic sensors. As an illustration, we plot the resulting magnetic distortion field (thus measurements are corrected for the magnetic background field) measurements at position 59 and this plot can be found in the top-right corner of Fig. 3.8. Note that this is a sensor that is directly below the longitudinal symmetry axis of the ellipsoid. In the first part of the scenario ( $0 \leq t < 200$ ), we see that there is a dominant change in the  $x$ -component. This is a direct consequence of a changing magnetization in the  $x$ -direction. Indeed, there are some variations up to 25 microtesla in the  $y$  and  $z$  component, but this is most likely due to misalignment of the sensor with respect to the ellipsoid. Then, the background field rotates which results in

variations in all three components. It is observed that those measured field values can be seen as the sum of measurements in the principal directions in the first part of the scenario. Therefore, we conclude that little anisotropic effects are present in this dataset.

Next, we have computed the magnetic state of the steel ellipsoid at each measurement point in the scenario using an inversion. Here, we assume that the ellipsoid consists of **homogeneous** distribution of ferromagnetic material and that the ellipsoid is **uniformly** magnetised: averaging the magnetisation over the ellipsoid

$$\mathbf{m} = \iiint_{\Omega} \mathbf{M}(\mathbf{r}) d\mathbf{r} \quad (3.84)$$

we have defined a simple magnetic dipole model for the steel ellipsoid. This model is in turn used to compute the magnetic state and the resulting temporal magnetisation can be found in the left-bottom corner of Fig. 3.8. Finally, a  $H - M$  hysteresis plot is shown in the bottom-right corner of Fig. 3.8.

Looking at the magnetisation in the  $x$ -component (the blue line), it is observed that there is a small hysteretic effect present, if one looks at the  $M$  values for  $H = 0$ . Depending on the increasing or decreasing branch, this value at  $H = 0$  may differ slightly. However, the gap is very small, indicating that the measurement hysteresis effects are small. Looking at the other components of the magnetisation, it is clear that there is almost no variations present in the measurement. This also supports the misalignment of the ellipsoid observation in the aforementioned argument.

We want to compare the measurement data with our hysteresis models from Section III. Although we were not able to estimate the material parameters for our steel ellipsoid due to a lack of time, we can illustrate the performance of our hysteresis model when coupled to the demagnetisation factors of the ellipsoid using the averaging model (3.84). In Fig. 3.9 examples of this averaging model can be found for the scalar Rayleigh hysteresis model, the scalar Jiles-Atherton model and energy-variational model (for the  $x$ -component of the magnetisation). Note that in all cases, due to the demagnetising field, the resulting  $H - M$  hysteresis curves have similar shapes and are approximately quadratic in nature. This gives us confidence that values for the parameters in these models can be found to represent the measurement data accurately.

### 3.6. CONCLUSION

In this Chapter we gave an overview of three known hysteresis models. We first described the principles of the Rayleigh hysteresis model, then we explained the physical-based concepts of the Jiles-Atherton model and finally we introduced the energy-variational model. In particular, we analysed these models by considering the model complexity, to what extent these models can be extended to incorporate properties such as inhomogeneity and anisotropy, the applicability of the model in large-scale applications, the (numerical) complexity of their computational burden, and their necessary parameter estimations.

We have illustrated the performance of these models by numerical examples that showed the resulting hysteresis curves, and we have looked at experimental data and related this to the aforementioned hysteresis models to analyse and explain the data in detail.

It is concluded that the energy-variational model is a very promising model for ferromagnetic hysteresis, but requires some additional research in the near future. Furthermore,

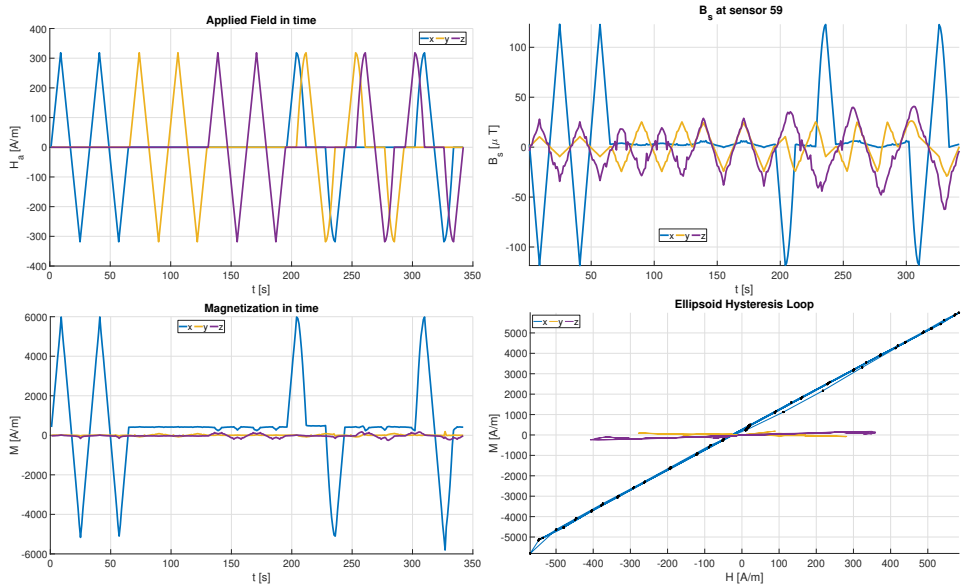


Figure 3.8: Measurements and results based on experimental data collected for a steel ellipsoid. In the top-left corner, the applied background field signal is depicted. The scenario consists of three consecutive saw-type waveforms along each of the principal axes and then a rotating field along the three planes  $x-y$ ,  $y-z$  and  $x-z$ . The magnetic induction field  $B_s$  shown in the field that is measured by sensor 59 after subtraction of the background field, and therefore shows the values of the distortion field caused by the steel ellipsoid. Note that the  $t-M$  relationship is computed using inversion based on analytical expressions for the propagation matrix that translates a magnetisation to the magnetic induction field at the sensor locations. The resulting hysteresis loop  $H-M$  as depicted in the bottom right picture clearly shows the effect of the demagnetisation field on hysteresis effects.

the Rayleigh hysteresis model is a simple model that describes small nonlinear ferromagnetic effects. The model is shown to be feasible for weak applied fields. In our applications, the Earth magnetic field is considered to be weak, and therefore it is expected that the hysteresis model is suitable for the development of a mathematical-physical model for magnetic signature monitoring.

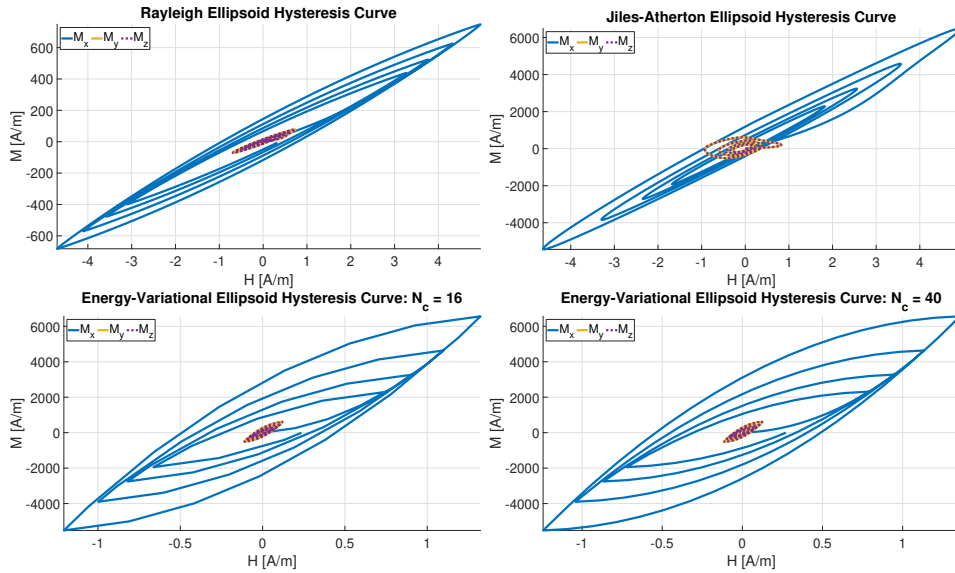


Figure 3.9: Resulting hysteresis curves for a steel ellipsoid. Note that due to the presence of a demagnetising field, the shape of the hysteresis curve is altered in all models. A common fact is that all curves more or less show minor curves that are proportional to second order polynomial curves, as found in the Rayleigh model.

## REFERENCES

- [1] O.C.O. Baas. Nonlinear Behaviour of Ferromagnetic Steel. Master thesis, 2018 <http://resolver.tudelft.nl/uuid:dc977bf0-8154-43ca-abe1-5160c7877ff2>.
- [2] A. J. Bergqvist. A Simple Vector Generalization of the Jiles-Atherton Model of Hysteresis. *IEEE Trans. on Magn.*, Vol: 32. No. 5. pp: 4213 – 4215. 1996.
- [3] A. J. Bergqvist. Magnetic vector hysteresis model with dry friction-like pinning. *Phys. B. Condens. Matter*. Vol. 233. No. 4. pp: 342 – 347. 1997.
- [4] Biedrzycki R., Szewczyk R., Švec P., Winiarski W. Determination of Jiles-Atherton Model Parameters Using Differential Evolution. *Advances in Intelligent Systems and Computing*. Vol 317. 2015.
- [5] D. Burgy. Magnetic and Magnetostrictive Characterization and Modeling of High Strength Steel. Dissertation. 2014.
- [6] K. H. Carpenter. A Differential Equation Approach to Minor Loops in the Jiles-Atherton Hysteresis Model. *IEEE Trans. on Magn.*, Vol: 27. No. 6. pp: 4404 – 4406. 1991.
- [7] O. Chadebec, J. L. Coulomb, J. P. Bongiraud, G. Cauffet, and P. Le Thiec. Recent improvements for solving inverse magnetostatic problem applied to thin hulls. *IEEE Trans. on Magn.*, Vol. 38, no. 2, pp. 1005–1008, 2002.

- [8] O. Chadebec, J. L. Coulomb, G. Cauffet, and J. P. Bongiraud. How to Well Pose a Magnetization Identification Problem. *IEEE Trans. on Magn.*. Vol. 39. No. 3. pp: 1634–1637. 2003.
- [9] Sushin Chikazumi and Stanley H. Charap. Physics of magnetism. Krieger Pub Co. June, 1978.
- [10] J. M. D. Coey. Magnetism and magnetic materials. Cambridge University Press. 2009.
- [11] K. O’Grady and S. J. Greaves. Minor Hysteresis loops effects in magnetic materials. *Journal of Magnetism and Magnetic Materials 138*. pp: L233–L236. 1994.
- [12] K. Hergli, H. Marouani, M. Zidi, Yasser Fouad and Mohamed Elshazly. Identification of Preisach hysteresis model parameters using genetic algorithms. *Journal of King Saud University*. 2017
- [13] John. J. Holmes. Modeling a Ship’s Ferromagnetic Signatures. Morgan & Claypool publ. Inc. 2007.
- [14] J. D. Jackson, *Classical Electrodynamics*. 3rd ed. New York: John Wiley & Sons, Inc. 1999.
- [15] D. Jiles and D. Atherton. Theory on Ferromagnetic Hysteresis. *Journal of Magnetism and Magnetic Materials 61*. Vol: 48. 1986.
- [16] D. Jiles. Numerical Determination of Hysteresis Parameters for the Modeling of Magnetic Properties Using the Theory of Ferromagnetic Hysteresis. *IEEE Transactions on Magnetics*. Vol: 28. No. 1. 1992.
- [17] D. C. Jiles. Frequency Dependence of Hysteresis Curves in “Non-Conducting” Magnetic Materials. *IEEE Trans. on Magn.*. Vol: 29. No. 6. pp: 3490 — 3492. 1993.
- [18] Jianming Jin. The Finite Element Method in Electromagnetics. New York: John Wiley & Sons, Inc. 2002.
- [19] M. Kachniarz, R. Szewczyk. Study on the Rayleigh Hysteresis Model and its Applicability in Modeling Magnetic Hysteresis Phenomenon in Ferromagnetic Materials. *Acta Physica Polonica A*. Vol: 131, No. 5. pp: 1244 – 1249. 2017.
- [20] P.H. Kirkegaard, R. Brincker. On the Optimal Locations of Sensors for Parametric Identification of Linear Structural Systems. *Mechanical Systems and Signal Processing*. Vol: 8. pp: 639 – 647. 1994.
- [21] B. Kvasnica and F. Kundracik. Fitting experimental anhysteretic curves of ferromagnetic materials and investigation of the effect of temperature and tensile stress B. *Journal of Magnetism and Magnetic Materials*. page 162. 2006.
- [22] Muzaffar Eusuff, Kevin Lansey and Fayzul Pasha. Shuffled frog-leaping algorithm: a memetic meta-heuristic for discrete optimization. *Engineering Optimization*. Vol: 38. No.2. pp: 129 – 154. 2006.

- [23] J.V. Leite et al.. The Inverse Jiles-Atherton Model Parameters Identification. *IEEE Trans. on Magn.*. Vol: 39. No. 3. pp: 1397 – 1400. 2003.
- [24] J.V. Leite et al.. Real coded genetic algorithm for Jiles-Atherton model parameters identification. *IEEE Trans. on Magn.*. Vol: 40. No. 2. pp: 888 – 891. 2004.
- [25] J.V. Leite, A. Benabou and N. Sadowski. Accurate minor loops calculation with a modified Jiles-Atherton hysteresis model. *COMPEL*. Vol: 28. No. 3. pp: 741 – 749. 2009.
- [26] J. J. Moreau. Application of convex analysis to the treatment of elastoplastic systems. In: Germain P., Nayroles B. (eds) *Applications of Methods of Functional Analysis to Problems in Mechanics*. Lecture Notes in Mathematics. Vol: 503. Springer, Berlin, Heidelberg. 1976.
- [27] R. Naghizadeh, B. Vahidi and S. H. Hosseinian. Parameter identification of Jiles-Atherton model using SFLA. Vol: 31. No. 3. pp: 1293 – 1309. 2012.
- [28] H.W.L. Naus. Theoretical developments in magnetomechanics. *IEEE Trans. on Magn.*. Vol: 47. No. 9. pp: 2155 – 2162. 2011.
- [29] Michał Nowickim, Roman Szewczyk and Paweł Nowak. Experimental Verification of Isotropic and Anisotropic Anhysteretic Magnetization Models. *Materials*. Vol: 12, pp: 1549. 2019.
- [30] N.C. Pop and O.F. Caltun. Jiles–Atherton Magnetic Hysteresis Parameters Identification. *ACTA PHYSICA POLONICA A*. Vol: 120. No. 3. pp: 491 – 497. 2011.
- [31] J.A. Osborn. Demagnetizing Factors of the General Ellipsoid. *Physical Review*. Vol. 67. No. 11 and 12. 1945.
- [32] C. Papadimitriou, J.L. Beck and S.K. AU. Entropy-Based Optimal Sensor Location for Structural Model Updating. *Journal of Vibration and Control*. Vol: 6. No. 5. pp: 781 – 800. 2000.
- [33] L. Prigozhin, V. Sokolovsky, J. W. Barret, and S. Zirka. On the Energy-Based Variational Model for Vector Magnetic Hysteresis. *IEEE Trans. on Magn.*. Vol: 52. No. 12. 2016.
- [34] Lord Rayleigh. On the behaviour of iron and steel under the operation of feeble magnetic forces. *Philos. Mag.*. Vol: 23 . pp: 225. 1887.
- [35] O. J. G. Somsen, G. P. M. Wagemakers. Separating Permanent and Induced Magnetic Signature: A Simple Approach. *International Journal of Electrical, Computer, Energetic, Electronic and Communication Engineering*. Vol: 9. No. 10. 2015.
- [36] H. W. F. Sung and C. Rudowicz. A closer look at the hysteresis loop for ferromagnets. Department of Physics and Materials Science, City University of Hong Kong.
- [37] G. Szymanski and M. Waszak. Vectorized Jiles–Atherton hysteresis model. *Physica B Condensed Matter*. Vol: 343. No 1. pp: 26 – 29. 2004.

- [38] Szewczyk R. Computational Problems Connected with Jiles-Atherton Model of Magnetic Hysteresis. In: Szewczyk R., Zieliński C., Kaliczyńska M. (eds) Recent Advances in Automation, Robotics and Measuring Techniques. Advances in Intelligent Systems and Computing. Vol 267. Springer. 2014.
- [39] M. Toman, G. Stumberger, and D. Dolinar. Parameter identification of the Jiles-Atherton hysteresis model using differential evolution. *IEEE Trans. on Magn.*. Vol. 44. No. 6. pp: 1098 – 1101. 2019.
- [40] Edward. D. Torre. Magnetic Hysteresis. Wiley-IEEE Press. 1999.
- [41] F.E. Udawadia. Methodology for Optimal Sensor Locations for Parameter Identification in Dynamic Systems. *Journal of Engineering Mechanics (ASCE)*. Vol: 120. No. 2. pp: 368 – 390. 1994.
- [42] A.R.P.J. Vijn, E.S.A.M. Lepelaars, J.B.L. Dubbeldam, M.B. van Gijzen, A.W. Heemink. Magnetic susceptibility Estimation for Magnetostatics. *IEEE Trans. on Magn.*. Vol. 55. No. 3. 2019.
- [43] Y. Vuillermet, O. Chadabec, J. L. Coulomb, J. P. Bongiraud, G. Cauffet and P. Le Thiec. Scalar Potential Formulation and Inverse Problem Applied to Thin Magnetic Sheets. *IEEE Trans. on Magn.*. Vol. 44. No. 6. 2008.
- [44] M. A. Zaman, P. C. Hansen. L. T. Neustock, P. Padhy and L. Hesselink. Adjoint Method for Estimating Jiles-Atherton Hysteresis Model Parameters. *Journal of Applied Physics*. No. 120. 2016.

# 4

## MAGNETIC SUSCEPTIBILITY ESTIMATION FOR MAGNETOSTATICS

*This chapter is based on:*

*Aad Vijn, Eugene Lepelaars, Johan Dubbeldam, Martin van Gijzen, Arnold Heemink.  
Magnetic Susceptibility Estimation for Magnetostatics. IEEE Trans. on Magn.. Vol: 55.  
No. 3. 2019.*

### ABSTRACT

*This chapter presents a parameter estimation method to determine the linear behavior of an metal object build from thin plates. Based on the magneto-static field equations, an integral equation is derived that fully determines the induced magnetization, whenever the spatial magnetic susceptibility distribution is known. This forward problem is used as an underlying physical model for the parameter estimation method. Using near field magnetic measurements around a thin plate, the parameter estimation yields a distribution of the magnetic susceptibility. Furthermore, a sensitivity analysis is performed to understand the behavior of this parameter estimation method.*

### 4.1. INTRODUCTION

Identification of the magnetic state of ferromagnetic objects is in general very difficult. A common approach is to split the total magnetization into two parts: an induced part and a permanent part. The induced magnetization is related to a linear response of the material to the background field, and the permanent part is due to the magnetic history of the material [16]. The magnetic history, also called magnetic hysteresis, is a very complex phenomenon that may be described by means of Preisach models [18] or continuous models such as Jiles

and Atherton [11]. The linear response is described by the magnetic susceptibility and may be complex to describe depending on the material properties. Isotropic material does not have a preferred direction in which it magnetizes, and therefore the magnetic susceptibility is easily described by a scalar quantity. For anisotropic materials, the magnetic susceptibility is harder to describe because of the orientation dependencies within the material.

A related notion to the magnetic susceptibility is the (relative) permeability, which seems to be more relevant in applications. The magnetic susceptibility  $\chi$  and relative permeability  $\mu_r$  are related to the well known identity

$$\chi + 1 = \mu_r$$

Hence, all results in this chapter (in terms of the magnetic susceptibility) can equivalently be expressed in terms of the permeability. From our point of view, we are interested in the magnetic susceptibility, because it links the internal magnetic field inside an object to its magnetization.

A typical application of identifications of magnetic states can be found in the military context. Nowadays, accurate identification of the magnetic state of a military vessel (called the magnetic signature) has become important, as more sophisticated weaponry use different kind of sensors – such as magnetic sensors – to find and destroy their target. It is of utmost importance for the navy to reduce the magnetic signature of their military vessels, to avoid detection and destruction of their vessels [7–9].

The forward computation of the induced magnetization is rather simple, and can be done in a finite-element environment. Such implementations are readily available in many software packages such as Comsol Multiphysics, Cédrat Flux3D and Ansys Maxwell. However, for such computations of the induced magnetization, the value of the magnetic susceptibility  $\chi$  must be known. In the literature, one can find specific values for different materials. In practice, anomalies in materials and the specific composition of the material imply variations in these values. Therefore, one should expect spatial variability of  $\chi$  in an object rather than being a constant. This makes accurate modeling of the forward problem complicated.

Several parameter estimation methods have been proposed for determination of the magnetic susceptibility. Susceptibility estimation is found in the determination of the initial magnetic susceptibility for the “Metal magnetic memory (MMM)” method to passive magnetic nondestructive testing [17]. Even though MRI works with a high frequency signal, a magnetic susceptibility method can be defined in magnetostatics by considering the relationship between the magnetic susceptibility and varying magnetic fields in the frequency domain (for a fixed frequency) [12]. However, for MRI-related applications the values of the magnetic susceptibility are presumed to be small (in the order of  $10^{-3}$ ), which leads to approximately linear estimation models. For ferromagnetic steel, the magnetic susceptibility values are high (in the range of  $10^2 - 10^5$ ), which leads to non-linear magnetic field equations in  $\chi$ . This case is more challenging and the techniques used are more involved.

This chapter considers two topics. Firstly, we derive a magnetic susceptibility estimation method to compute spatial magnetic susceptibility distributions of linearly reacting materials, for which the magnetic susceptibility values are large. This method is based on least-squares optimization and solved using the “Broyden-Fletcher-Goldfarb-Shanno” method [13]. Because approximations of these spatial magnetic susceptibility distributions

may contain errors, we are interested in how these variations relate to the corresponding variations in the induced magnetic induction field. Such insights may also tell us to what extent the parameter estimations must be accurate. It is also important for future work, where we try to describe the magnetic distortion fields of magnetic objects accurately. These sensitivity questions are considered in the second part of this chapter.

This chapter has the following structure. In section II, the methodology behind the derived magnetic susceptibility estimation is discussed. A forward model is derived that fully describes the linear behavior. Several magnetic identification methods are proposed for semi-linearly reacting materials [3, 4, 19]. However, we take another, slightly different, approach to describe the induced magnetization. From a physical point of view, we assume that magnetization is a continuous vector field. Therefore, we expand any magnetization as a function in terms of linear basis functions. This has some advantages, e.g, enabling the use of smoothing regularization operators. Then, using various techniques from variational data assimilation [5, 20] and numerical analysis [6], we solve the proposed nonlinear minimization problem. In section III numerical examples are given that illustrate the forward and magnetic susceptibility estimation. A numerical identical-twin experiment where the true magnetic susceptibility state is assumed to be known is conducted to test the validity of the methodology. In this stage of the research it is essential to consider first a numerical validation of the method, because the true magnetic susceptibility state of magnetic objects are unknown in practice and therefore the performance of the method is hard to analyse. In section IV, a sensitivity analysis is then performed to investigate the behavior of variations in the magnetic susceptibility in forward computations. A conclusion and a discussion of future work for further enhancement of the proposed parameter estimation method are summarized in Section V.

## 4.2. METHODOLOGY

In this section, the methodology behind our proposed parameter estimation method is discussed. Starting with the derivation of the underlying physical model from classical physical principles in magnetostatics, the parameter estimation method is then derived using techniques from variational data assimilation.

### 4.2.1. MAGNETOSTATICS

Suppose that an object is made of linearly reacting and isotropic material, and suppose that the magnetic susceptibility  $\chi$  and the geometry of the object are known. Furthermore, assume that the object is made of thin plates with a thickness  $t$ .

The object is placed in a uniform magnetic background field  $\mathbf{B}_0 = \mu_0 \mathbf{H}_0$ . The background field induces some magnetization denoted by  $\mathbf{M}^{ind}$ . Assume that any permanent magnetization is absent, therefore the magnetization of  $\Omega$  reads

$$\mathbf{M} := \mathbf{M}^{ind}.$$

Due to the induced magnetization, a perturbation arises and this perturbation is called the reduced (or induced) magnetic field, denoted by  $\mathbf{H}_{red}$ . The total magnetic field  $\mathbf{H}$  reads

$$\mathbf{H} = \mathbf{H}_0 + \mathbf{H}_{red}. \quad (4.1)$$

Let  $\Omega \subseteq \mathbb{R}^3$  be the compact volume of the object. The linear behavior in  $\Omega$  is defined through

$$\mathbf{M} = \chi \mathbf{H} \quad (4.2)$$

which defines the coupling between the magnetic field and the magnetization of object  $\Omega$ . Here,  $\chi$  is a dimensionless number which is assumed to be spatially dependent.

To obtain the reduced magnetic field due to  $\mathbf{M}$ , use the magnetostatic field equations:

$$\begin{cases} \nabla \times \mathbf{H} = \mathbf{0} \\ \nabla \cdot \mathbf{B} = 0 \\ \mathbf{B} = \mu_0(\mathbf{H} + \mathbf{M}) \end{cases} . \quad (4.3)$$

In these equations,  $\mathbf{B}$  denotes the magnetic induction field, and  $\mu_0 = 4\pi \cdot 10^{-7} \text{ H/m}$  is the magnetic permeability in vacuum. The magnetostatic equations can be solved via a scalar potential function, see [10, page 194–197]. The reduced magnetic field at point  $\mathbf{r}$  reads:

$$\mathbf{H}_{red}(\mathbf{r}) = -\frac{1}{4\pi} \iiint_{\Omega} \frac{\mathbf{r} - \mathbf{r}'}{|\mathbf{r} - \mathbf{r}'|^3} (\nabla' \cdot \mathbf{M})(\mathbf{r}') d\Omega' + \frac{1}{4\pi} \iint_{\partial\Omega} \frac{\mathbf{r} - \mathbf{r}'}{|\mathbf{r} - \mathbf{r}'|^3} (\mathbf{n}' \cdot \mathbf{M})(\mathbf{r}') dS' \quad (4.4)$$

where  $\mathbf{n}' = \mathbf{n}'(\mathbf{r}')$  is a normal vector, pointing outwards. The differential operator  $\nabla'$  is defined by  $\nabla' = [\partial_{x'}, \partial_{y'}, \partial_{z'}]^T$ . The magnetization  $\mathbf{M}$  is supported on  $\Omega$ , and  $\mathbf{M} \equiv \mathbf{0}$  outside  $\Omega$ .

Combining equations (6.5), (4.2) and (4.4) leads to the following integral equation for  $\mathbf{M}$  (see [19])

$$\frac{1}{\chi(\mathbf{r})} \mathbf{M}(\mathbf{r}) + \frac{1}{4\pi} \iiint_{\Omega} \frac{\mathbf{r} - \mathbf{r}'}{|\mathbf{r} - \mathbf{r}'|^3} (\nabla' \cdot \mathbf{M})(\mathbf{r}') d\Omega' - \frac{1}{4\pi} \iint_{\partial\Omega} \frac{\mathbf{r} - \mathbf{r}'}{|\mathbf{r} - \mathbf{r}'|^3} (\mathbf{n}' \cdot \mathbf{M})(\mathbf{r}') dS' = \mathbf{H}_0. \quad (4.5)$$

Note that this equation is only valid *inside* the object  $\Omega$ . Evaluation of (4.5) in a point  $\mathbf{r} \in \Omega$  is mathematically challenging, since both integrals are singular for  $\mathbf{r}' = \mathbf{r}$ . Equation (4.5) must be reformulated in such a way that these singularities are avoided. This is done after discretization of  $\Omega$ , using Gauss' divergence theorem. See Appendix 4.5.

#### 4.2.2. THE DISCRETE FORWARD PROBLEM

Introduce a triangulation of  $\Omega = \bigcup_{k=1}^{N_e} e_k$  where  $N_e$  is the number of triangular elements. Because  $\Omega$  is thin, we assume in the remainder of this chapter that  $\Omega$  is a two-dimensional surface and that the elements  $e$  are flat triangles. Using demagnetization factors [14] one can derive that in this case the magnetization is approximately tangential to the object and as  $\chi$  is large, the induced magnetization is approximately uniform in the normal direction. In Fig. 4.1 one can find an example of a triangulation of a square plate. Furthermore, assume that  $\chi$  is piecewise constant on each triangular element:

$$\chi = \chi_k \quad \text{on element } e_k, \quad \chi_k \in \mathbb{R}_0^+. \quad (4.6)$$

The next step is to approximate the magnetization  $\mathbf{M}$  on each element. To have a non-trivial description for  $\nabla \cdot \mathbf{M}$ , we assume that  $\mathbf{M}$  is linear on each triangular element  $e$ , hence we

expand  $\mathbf{M}$  in terms of linear basis functions. On a triangular element  $e$  the approximation of  $\mathbf{M}$  is denoted by  $(\mathbf{M})_e$  and reads

$$(\mathbf{M})_e(\mathbf{r}) = \sum_{k=1}^3 \mathbf{M}_k \varphi_k(\mathbf{r}). \quad (4.7)$$

where  $\mathbf{M}_k$  are the values of  $\mathbf{M}$  at the vertices  $\mathbf{v}_1, \mathbf{v}_2$  and  $\mathbf{v}_3$  of the triangular element  $e$  and  $\varphi_1, \varphi_2$  and  $\varphi_3$  are linear basis functions on  $e$  defined by the relations

$$\varphi_i(\mathbf{v}_j) = \delta_{ij}, \quad \text{for } i, j = 1, 2, 3. \quad (4.8)$$

To find a local description of the magnetisation, let  $\mathcal{L}_e = \{\mathbf{s}, \mathbf{t}, \mathbf{n}\}$  be an orthonormal basis for element  $e$ . Such a local description allows one to impose extra constraints on the magnetisation such as a vanishing normal component, as indicated by the demagnetisation factors of a thin sheet. 5Locally, the magnetization at each vertex point is thus reads

$$\mathbf{M}(\mathbf{v}_k) = C\hat{\mathbf{M}}(\mathbf{v}_k) = C\hat{\mathbf{p}}_k, \quad \hat{\mathbf{p}}_k \in \mathbb{R}^2$$

where  $C$  is  $3 \times 2$  the change of basis matrix from the local coordinates to the global ones, which is simply given by  $C = [\mathbf{s} \quad \mathbf{t} \quad \mathbf{n}]$ . Note that  $C$  is constant, because we consider non-curved triangular elements. Therefore, it is straight-forward to construct such local bases for any triangular element in our mesh. The expansion of  $\mathbf{M}$  on  $e$  in terms of the values  $\hat{\mathbf{p}}_k$  is given by

$$(\mathbf{M}(x, y, z))_e = \sum_{k=1}^3 C\hat{\mathbf{p}}_k \varphi_k(x, y, z)$$

Hence, the magnetization  $\mathbf{M}$  on  $e$  is fully determined whenever the six values of  $\hat{\mathbf{p}}_k$  (two on each vertex of element  $e$ ) are known.

Finally, we derive an explicit expression for the divergence of the magnetization  $\mathbf{M}$ . Recall that for any constant vector  $\mathbf{c}$  we have  $\nabla \cdot (\mathbf{c}\psi) = \mathbf{c} \cdot \nabla\psi$ . Using this result, we can derive an elegant expression for  $\nabla \cdot \mathbf{M}$  in terms of the entries of  $\hat{\mathbf{p}}_k$ :

$$\begin{aligned} (\nabla \cdot \mathbf{M})_e &= \nabla \cdot (\mathbf{M})_e \\ &= \nabla \cdot \left( \sum_{k=1}^3 \mathbf{p}_k \varphi_k \right) \\ &= \sum_{k=1}^3 \mathbf{p}_k \cdot \nabla \varphi_k \\ &= \sum_{k=1}^3 (\mathbf{s}[\hat{p}_k]_s + \mathbf{t}[\hat{p}_k]_t + \mathbf{n}[\hat{p}_k]_n) \cdot \nabla \varphi_k \end{aligned}$$

Therefore, the expansion for  $\nabla \cdot \mathbf{M}$  on element  $e$  is given by

$$(\nabla \cdot \mathbf{M})_e = \sum_{k=1}^3 (\mathbf{s} \cdot \nabla \varphi_k) [\hat{p}_k]_s + (\mathbf{t} \cdot \nabla \varphi_k) [\hat{p}_k]_t + (\mathbf{n} \cdot \nabla \varphi_k) [\hat{p}_k]_n \quad (4.9)$$

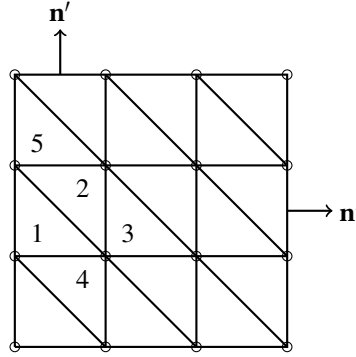


Figure 4.1: Example of a triangulation, with triangular elements  $e_1, \dots, e_5$ . Note that we assume that the normal vector points outward.

4

such that on each element  $e$ , the divergence of  $\mathbf{M}$  is approximated by a constant value, in terms of the entries of  $\hat{\mathbf{p}}$  in each vertex of element  $e$ .

It remains to derive suitable expressions the expansion of  $\mathbf{n}' \cdot \mathbf{M}$  on some line boundary element  $be$  with outward pointing normal vector. Here, the vector  $\mathbf{n}'$  is the normal vector that is perpendicular to  $be$ . We fix some boundary element  $be$  with vertices  $\{\mathbf{v}_1, \mathbf{v}_2\}$  and observe that this element is a face of some triangular element  $e$  with vertices  $\{\mathbf{v}_1, \mathbf{v}_2, \mathbf{v}_3\}$ . We use the local coordinates of this corresponding triangular element to expand  $\mathbf{M}$ . Then we have on  $be$ :

$$(\mathbf{n}' \cdot \mathbf{M})_{be} = \sum_{k=1}^2 (\mathbf{s} \cdot \mathbf{n}') \varphi_k[\hat{p}_k]_s + (\mathbf{t} \cdot \mathbf{n}') \varphi_k[\hat{p}_k]_t + (\mathbf{n} \cdot \mathbf{n}') \varphi_k[\hat{p}_k]_n \quad (4.10)$$

In the case that we consider the expansions in the same global coordinate system using the standard euclidean basis for  $\mathbb{R}^3$ , expression (4.9) simplifies. The divergence of  $\mathbf{M}$  and the flux  $\mathbf{n}' \cdot \mathbf{M}$  are then approximated using these expansions:

$$\begin{aligned} (\nabla' \cdot \mathbf{M})_e(\mathbf{r}') &= \sum_{k=1}^3 \mathbf{M}_k \cdot \nabla' \varphi_k(\mathbf{r}') \\ (\mathbf{n}' \cdot \mathbf{M})_e(\mathbf{r}') &= \sum_{k=1}^3 (\mathbf{n}' \cdot \mathbf{M}_k) \varphi_k(\mathbf{r}'). \end{aligned} \quad (4.11)$$

Using the triangulation and the above expansions for  $\mathbf{M}$ , integral equation (4.5) is reduced to a finite-dimensional system of equations. Due to the small thickness of  $\Omega$ , the volume and surface integrals in (4.5) are reduced to surface and line integrals. After applying a

Galerkin projection method<sup>12</sup>, one obtains the following set of equations:

$$\frac{1}{\chi(\mathbf{r}_i)} (\mathbf{M})_{e_k}(\mathbf{r}_i) + \frac{t}{4\pi} \sum_e \int_{\partial e} \frac{\mathbf{n}'}{|\mathbf{r}_i - \mathbf{r}'|} (\nabla' \cdot \mathbf{M})_e(\mathbf{r}') dS' - \frac{t}{4\pi} \sum_e \int_{\partial \Omega \cap e} \frac{\mathbf{r}_i - \mathbf{r}'}{|\mathbf{r}_i - \mathbf{r}'|^3} (\mathbf{n}' \cdot \mathbf{M})_e(\mathbf{r}') dl' = \mathbf{H}_0 \quad (4.12)$$

for each evaluation point  $\mathbf{r}_i \in e_k$ . The normal vector  $\mathbf{n}'$  is defined as a vector pointing outwards as illustrated in Fig. 4.1. Each evaluation of (4.12) in a point leads to a single equations in terms of the background field  $\mathbf{H}_0$ , the magnetic susceptibility values and magnetization values  $\mathbf{M}_k$  at the grid points.

If the integral equation is evaluated in three points per triangular element  $e_k$  the above integral equation (4.5) can be solved consistently by solving the corresponding discrete system (4.12). Further derivations show that (4.12) can be written as a system of the form

$$\left[ \sum_{k=1}^{N_e} \frac{1}{\chi_k} D_k + A + B \right] \mathbf{M} = \mathbf{h}_0. \quad (4.13)$$

The matrices  $D_k, A, B \in \mathbb{R}^{3M \times 3N}$ , where  $M$  is the number of evaluation points and  $N$  is the number of grid points and  $\mathbf{h}_0 \in \mathbb{R}^{3M}$  is a constant vector that contains the magnetic background field. Vector  $\mathbf{M} \in \mathbb{R}^{3N}$  is now the numerical approximation of the magnetization and contains the values of the magnetization in each of the grid points. Note that this vector suffices to describe the full magnetization through (4.7). Furthermore, the entries of  $D_k, A$  and  $B$  may be computed analytically, or approximated numerically by means of suitable quadrature rules.

Finally, if  $\mathbf{M}$  is obtained after solving (4.13), the same triangulation and expansion is used to compute the (total) magnetic induction field at any observation point via

$$\mathbf{B}^c(\mathbf{r}_k) = \mathbf{B}_0 + \mathbf{B}_{red}(\mathbf{r}_k) \quad (4.14)$$

where  $\mathbf{B}_{red}(\mathbf{r}_k)$  is written as

$$\mathbf{B}_{red}(\mathbf{r}_k) = \mu_0 C(\mathbf{r}_k) \mathbf{M}. \quad (4.15)$$

The matrix  $C(\mathbf{r}_k) \in \mathbb{R}^{3 \times 3N}$  is obtained from (4.4) after applying the discretization and evaluation at  $\mathbf{r}_k$ .

### 4.2.3. INVERSE PROBLEM FORMULATION

Based on the discrete forward problem described in the previous subsection, one can formulate the corresponding (discrete) inverse problem. Suppose that the magnetic induction field of some linearly reacting magnetic object  $\Omega$  is measured, the inverse problem is to determine the magnetic source  $\mathbf{M}^{ind}$ , based on the physical model described in section 4.2.2.

<sup>1</sup>A word of caution on the reduction of the integral equation to the discrete case. Whenever the diameter of the triangular elements  $e_k$  become smaller than the thickness  $t$  of object  $\Omega$ , then approximation (4.12) of integral equation (4.5) becomes invalid.

<sup>2</sup>In the derivation of (4.12), the assumptions are used in a slightly different order. One first start with a discretization of the full three-dimensional object  $\Omega$ , and uses the typical value of the thickness to neglect terms of the equation. One is then left with integrals defined on the surface of the three-dimensional object, as mentioned in (4.12).

If  $\mathcal{M} = \{\mathbf{r}_1, \mathbf{r}_2, \dots, \mathbf{r}_K\}$  denotes a collection of measurement locations, the values of the magnetic induction field in the measurement locations gives rise to a vector  $\mathbf{B}^m \in \mathbb{R}^{3K}$  given by

$$\mathbf{B}^m = [(\mathbf{B}^m(\mathbf{r}_1))_x, (\mathbf{B}^m(\mathbf{r}_1))_y, (\mathbf{B}^m(\mathbf{r}_1))_z, \dots, (\mathbf{B}^m(\mathbf{r}_K))_x, (\mathbf{B}^m(\mathbf{r}_K))_y, (\mathbf{B}^m(\mathbf{r}_K))_z]^T. \quad (4.16)$$

Each measurement is contaminated by noise; in this chapter we assume Gaussian white noise and write

$$\mathbf{B}^m := \mathbf{b}_0 + \mathbf{B}_{red}^e + \mathbf{e}, \quad \mathbf{e} \sim \mathcal{N}(0, \Sigma) \quad (4.17)$$

where  $\Sigma$  is the covariance matrix of  $\mathbf{e}$ ,  $\mathbf{B}_{red}^e$  are the exact values of the reduced magnetic induction field and  $\mathbf{b}_0 \in \mathbb{R}^{3K}$  is a constant vector containing the values of the magnetic background induction field. Similarly, using the discrete forward model, one can compute the magnetic induction field in the measurement locations for some prescribed magnetic susceptibility distribution. This forward computation gives rise to a vector  $\mathbf{B}^c[\chi]$  that is computed via a simple matrix-product:

$$\mathbf{B}^c[\chi] := \mathbf{b}_0 + C(\mathcal{M})\mathbf{M}, \quad (4.18)$$

where  $C(\mathcal{M}) \in \mathbb{R}^{3K \times 3N}$  is built out of block matrices defined in (4.15).

#### 4.2.4. INVERSION, MINIMIZATION PROBLEM

System (4.13) and expressions (4.16) and (4.18) are the starting point of the derivation of the parameter estimation method. The idea is as follows: based on near field measurements of the magnetic field  $\mathbf{B}$ , the task is to find a suitable spatial distribution of  $\chi$  such that there is a good fit between computed values and the measured values. This naturally results in defining the residual

$$\mathbf{Res} := \mathbf{B}^m - \mathbf{B}^c[\chi] \quad (4.19)$$

If the residual is small, a good fit between the measured values and computed values is expected, and the choice of the corresponding spatial distribution of  $\chi$  should be acceptable. Define the residual functional

$$\mathcal{J}(\chi) = \frac{1}{2} \mathbf{Res}^T W \mathbf{Res} = \frac{1}{2} \|\mathbf{Res}\|_W^2. \quad (4.20)$$

where  $W = \Sigma^{-1}$  is the inverse of the covariance matrix. Note that  $\mathcal{J}$  depends on  $\chi$ , although this dependency is not explicitly visible from its definition. The parameter estimation method is based on the iterative minimization of this functional. A solution of the parameter estimation method is found through

$$\chi^* = \underset{\chi \in \mathbb{R}^{N_e}}{\operatorname{argmin}} \mathcal{J}(\chi). \quad (4.21)$$

In practice, measurements are contaminated by noise. Noise typically arises from measurement interference and inaccuracies in the measuring devices; for magnetic field sensors these inaccuracies are e.g. orthogonality errors between axes, temperature dependencies,

hysteresis in the device and scaling errors. This implies that whenever one tends to solve (4.21), a certain tolerance level  $\varepsilon_{tol}$  should be chosen in such a way that it reflects the noise level in the measurements (4.17):

$$\text{stop whenever } |\mathcal{J}(\chi^*)| < \varepsilon_{tol}. \quad (4.22)$$

Otherwise, the minimization will over fit the noise in the measurements, which leads to unsatisfying solutions.

#### 4.2.5. INVERSION, REGULARIZATION

In general the solution of least-squares problem (4.21) is not unique, and  $\mathcal{J}(\chi)$  has many local minima. In order to choose the optimal minimizer, additional information can be added to the least-squares problem to reduce the dimensions of the solution space.

In the literature the values of  $\chi$  for different materials can be found. This information can be used as a prior estimation of the  $\chi$ -distribution in the minimization to guide the search of the solution, denoted by  $\chi_{prior}$ .

In addition, one may require that  $\chi$  satisfies a smoothness condition [2, Chapter 3.2]. Such a condition can be formalized in terms of a smoothing operator, say  $R$ , which originates from application of finite differences to  $\chi$ . Smoothness requirements ensure that the value of  $\chi_k$  on some element  $e_k$  should not differ much from its neighbors  $\chi_j$ . Define the function

$$\varphi: \bigcup_{k=1}^{N_e} \{e_k\} \rightarrow \{1, 2, 3\}, \quad e_k \mapsto \varphi(e_k) \quad (4.23)$$

as the number of adjacent triangular elements  $e_j$ ; call two elements  $e_p$  and  $e_q$  *adjacent* whenever they share a side. The following stochastic equation reflects the smoothness condition:

$$\chi_k = \frac{1}{\varphi(e_k)} \sum_{i=1}^{\varphi(e_k)} \chi_{k_i} + I_k, \quad I_k \sim \mathcal{N}(0, \sigma_k^2) \quad (4.24)$$

for  $k = 1, 2, \dots, N_e$ . Element  $e_{k_i}$  is a neighbors of  $e_k$  and the term  $I_k$  is called an innovation term. The innovation term shows that  $\chi_k$  can vary with respect to its neighbors. The value of  $\sigma_k$  reflects to what extent the value of  $\chi_k$  can differ with respect to the values of its neighbors. To illustrate this idea, apply (4.24) to the elements in Fig. 4.1 to obtain e.g.

$$\begin{aligned} \chi_1 &= \frac{1}{2}(\chi_2 + \chi_4) + I_1, \\ \chi_2 &= \frac{1}{3}(\chi_1 + \chi_3 + \chi_5) + I_2. \end{aligned} \quad (4.25)$$

The set of equations in (4.24) can be written as

$$R\chi = E \quad (4.26)$$

where  $R \equiv (I_{N_e \times N_e} - S)$  and  $E \sim \mathcal{N}(0, \Sigma_{N_e \times N_e})$ . The matrix  $S$  originates from the right-hand side in (4.25). Note that the null space of  $R$  is one-dimensional and consists of all uniform  $\chi$ -distributions. The obtained operator  $R$  is used to regularize the solutions. The stochastic model (4.24) can be used if one defines the minimization problem in terms of a Bayesian framework [2].

In general, if  $\Omega$  is meshed by means of a non-uniform triangulation, smoothness requirement (4.24) must be replaced by e.g.

$$\chi_k = \sum_{i=1}^{\varphi(e_k)} \left( \frac{\mu(e_{k_i})}{\sum_{j=1}^{\varphi(e_k)} \mu(e_{k_j})} \right) \chi_{k_i} + I_k, \quad I_k \sim \mathcal{N}(0, \sigma_k^2) \quad (4.27)$$

where  $\mu(e)$  measures the area of element  $e$ . Note that in the case the triangulation is uniform expression (4.27) reduces to (4.24).

Tikhonov regularization [2, Chapter 6] means that the original problem is replaced by a nearby minimization problem

$$\chi^* = \operatorname{argmin}_{\chi \in \mathbb{R}^{N_e}} \mathcal{J}(\chi) + \lambda^2 \frac{1}{2} \|R(\chi - \chi_{prior})\|_2^2 \quad (4.28)$$

here  $\lambda$  is called the regularization parameter. The regularization parameter should be selected in such a way that for the desired solution, the norm of the vector  $R(\chi - \chi_{prior})$  is not excessively large; whenever  $\|R(\chi - \chi_{prior})\|_2$  is small, it follows that  $\chi$  is relatively smooth. However, it is not desirable that the norm is close to zero, because it would imply that the found solution hardly shows variation.

In general, it is not clear which value for  $\lambda$  is optimal and how to find a suitable value. One heuristic approach is the use of the so-called  $L$ -curve [6]. The most favorable value of  $\lambda$  is the one that corresponds to the corner of the  $L$ -curve, which gives a good balance between the minimization of the residual and the size of the regularization term. However, the computation of this  $L$ -curve is too cumbersome and time-consuming.

#### 4.2.6. INVERSION, SOLVING THE MINIMIZATION PROBLEM

Hereinafter, problem (4.28) is considered. Note that this problem is not linear in  $\chi$ . Therefore the parameter estimation method is based on a nonlinear least-squares problem. A sophisticated (iterative) numerical solver is required to solve this least-squares problem. Recall that a necessary condition for  $\chi^{opt}$  to be a local minimum for  $\mathcal{J}$  is

$$\nabla \left[ \mathcal{J}(\chi) + \lambda^2 \frac{1}{2} \|R(\chi - \chi_{prior})\|_2^2 \right] \Big|_{\chi = \chi^{opt}} = \mathbf{0}. \quad (4.29)$$

In Gauss-Newton-Type methods [13, Chapter 3], one requires these gradients with respect to  $\chi$  for efficient computation of the nonlinear least-squares problem. In general, it is complex to find an analytical expression for this gradient, as the underlying physical model may consist of many nonlinearities. It is favorable to derive analytical expressions for the gradient, as this reduces the computational time significantly. In Appendix 4.5, analytical expressions for the gradient of  $\mathcal{J}$  are derived using the adjoint method.

The quasi-Newton method or ‘‘Broyden-Fletcher-Goldfarb-Shanno’’ [13], with acronym BFGS, is used to solve the minimization problem. The BFGS method is part of the **fminunc** routine in the unconstrained optimization toolbox in MATLAB, and uses the gradient expressions derived for (4.28).

In practice, the value of  $\mathcal{J}$  is rather small, and therefore any pre-programmed tolerance values are already met, terminating the process. Scaling of the problem avoids this problem.

To overcome any numerical problems, we introduce the scaling factor  $\kappa$  in the minimization problem and write

$$\chi^* = \underset{\chi \in \mathbb{R}^{N_e}}{\operatorname{argmin}} \kappa \left[ \mathcal{J}(\chi) + \lambda^2 \frac{1}{2} \|R(\chi - \chi_{prior})\|_2^2 \right]. \quad (4.30)$$

An appropriate choice for scaling factor  $\kappa$  is

$$\kappa = \left( \mathcal{J}(\chi_0) + \lambda^2 \frac{1}{2} \|R(\chi_0 - \chi_{prior})\|_2^2 \right)^{-1} \quad (4.31)$$

for some regularization parameter  $\lambda$  and initial guess  $\chi_0$  in the BFGS method.

#### 4.2.7. MAGNETIC SUSCEPTIBILITY ESTIMATION METHOD

Finally, we present our main result in this chapter. The parameter estimation method, that computes estimations of spatially magnetic susceptibility distributions, is called the ‘‘Magnetic Susceptibility Estimation Method’’. We abbreviate our parameter estimation method by **MSEM** and it is defined as follows: Based on an initial guess for  $\chi$ , say  $\chi_0$ , solve problem (4.28) for  $\lambda = 0$  to obtain a solution of the original problem without any regularization. Then, the obtained solution acts as initial guess for the full problem described in (4.28), for some nonzero  $\lambda$ . The obtained solution is the estimation for  $\chi$ . Pseudo-code for this method can be found in Fig. 4.2.

It is observed that residual functional (4.20) is quite insensitive to variations in  $\chi$ , which makes the search for an optimal solution difficult. This is due to the asymptotic behavior of forward model (4.13) for  $\chi \rightarrow \infty$ . Rescaling the problem via (4.30) and (4.31) allows the BFGS method to find a local optimal solution. This solution is then used in the **MSEM** to find a more optimal regularized solution.

### 4.3. NUMERICAL EXAMPLES

In this section two numerical examples are given. First, the integral equation is solved for a square plate to obtain the induced magnetization  $\mathbf{M}$ , and then the corresponding reduced magnetic field is computed in a plane above the plate. The typical shape of the solution  $\mathbf{M}$  shows that the integral equation is implemented correctly. Then, an identical-twin experiment is conducted to test the methodology.

#### 4.3.1. SOLVING THE INTEGRAL EQUATION

Consider the following simple example: a square plate  $\Omega$  that is 1m long and 10 mm thick is placed in a uniform external magnetic field given by

$$\mathbf{B}_0 = [60, 0, 0]^T \quad (\mu T). \quad (4.32)$$

Suppose that the magnetic susceptibility is uniform on  $\Omega$  and  $\chi \equiv 100$ ; the plate is meshed into 50 triangular elements. The condition number of system (4.13) is approximately 28, which means that the system is well conditioned. Therefore, the problem may be solved using an *LU* or SVD decomposition. The resulting magnetization distribution  $\mathbf{M}$  is shown

**Magnetic Susceptibility Estimation Method:****Input:** Set  $\chi_0 \in \mathbb{R}^{N_e}$ ,  $\varepsilon_{tol} \in \mathbb{R}^+$ ,  $\chi_{prior}$  and  $\kappa, \lambda \geq 0$ **Output:** Minimizer  $\chi^*$  of problem (4.28)1: **function** PARAMETERESTIMATION2: Use **fminunc**( $\chi_0, \varepsilon_{tol}$ ) to solve

$$\hat{\chi} = \underset{\chi \in \mathbb{R}^{N_e}}{\operatorname{argmin}} \mathcal{J}(\chi)$$

3: Use **fminunc**( $\hat{\chi}, \varepsilon_{tol}$ ) to solve

$$\chi^* = \underset{\chi \in \mathbb{R}^{N_e}}{\operatorname{argmin}} \mathcal{J}(\chi) + \lambda^2 \frac{1}{2} \|R(\chi - \chi_{prior})\|_2^2$$

4: **return**  $\chi^*$ 5: **end function**

Figur 4.2: Magnetic Susceptibility Estimation Method.

in Fig. 4.3. Note that the induced magnetization is more or less parallel to the background field, as expected. At 5 cm above  $\Omega$  the corresponding magnetic field is computed. The results are shown in Fig 4.4.

**4.3.2. TWIN EXPERIMENT FOR PARAMETER ESTIMATION**

Identical-twin experiments [1] use a model to generate a set of “observations”, add random noise to the simulated observations, and then try to estimate the true model parameters, using these noisy observations and the **same** model. This type of experiment is a natural first step, because it limits the sources of errors to a minimum and it enables us to understand whether or not the estimation method acts consistently to simulated data.

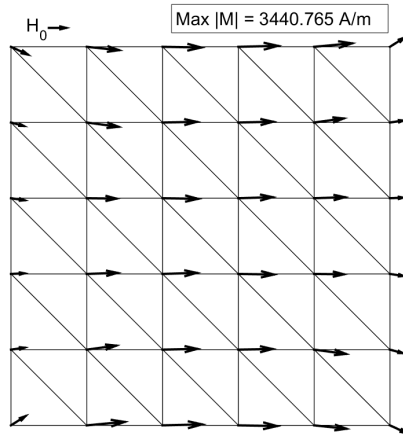
Our estimation method is tested on a square steel plate using an identical-twin experiment. Start with a plate with a length  $L$  of 1 meter, a width  $W$  of 1 meter and 10 mm thickness. Suppose a continuous  $\chi$  distribution is given by

$$\chi(\mathbf{r}) = 70 + 30 \cos(2\|\mathbf{r} + \mathbf{c}\|_2), \quad \mathbf{c} = \frac{1}{2}[L, L]^T. \quad (4.33)$$

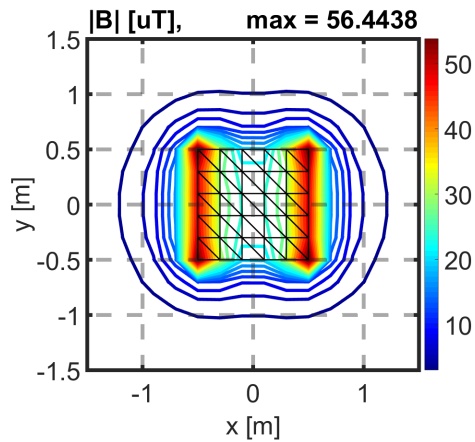
The vector  $\mathbf{c}$  indicates the center of the plate. The above definition of  $\chi$  defines a smooth varying  $\chi$ -pattern of the plate. The plate is meshed into  $N_e = 200$  triangular elements. In each element we compute the value  $\chi$  using (4.33). This leads to the true model parameters  $\chi_{true} \in \mathbb{R}^{200}$ , as depicted in Fig. 4.5a.

For the above mentioned plate with magnetic susceptibility  $\chi_{true}$ , generate a set of  $M = 225$  measurements of the reduced near field in a uniform sampling grid  $\frac{1}{2}[-L, L]^2$  at  $z = 1$  cm above the plate and form  $\mathbf{B}_c^m \in \mathbb{R}^{3M}$  using (4.13), (4.14) and (4.16). Gaussian white noise is added to each component of  $\mathbf{B}_c^m$ :

$$\mathbf{B}^m = \mathbf{B}_c^m + \mathbf{e}, \quad \mathbf{e} \sim \mathcal{N}(0, \sigma^2 I_{3M \times 3M}). \quad (4.34)$$



Figuur 4.3: Induced magnetization on a square plate for  $\chi \approx 100$ , placed in a uniform background field  $\mathbf{H}_0 = 50\mathbf{u}_x$  A/m.



Figuur 4.4: Reduced magnetic induction field 5 cm above the plate.

We choose  $\sigma = 10^{-6}$  in the above error vector, which means that there is approximately  $3\mu T$  variation in each component. In practice, magnetic sensors have a measurement error in the order of  $1nT$ , but in this twin experiment we want to push the boundaries of the performance of **MSEM**. Set

$$\chi_0 \equiv 70, \quad \chi_{prior} \equiv 0, \quad \lambda = 10^{-11}, \quad (4.35)$$

and apply the **MSEM** to the above set of noisy measurements. The results of  $\hat{\chi}$  and  $\chi^*$  are depicted in Fig. 4.5b and 4.5c. Note the influence of regularization on the obtained estimate  $\chi^*$ . Regularization not only steers the iterative solver to a better minimizer, but we are even able to reconstruct the true  $\chi$ -pattern with a high accuracy. In Fig. 4.7 and 4.8 the iterative process in the second step of **MSEM** is shown. Note that, for a nonlinear problem, the convergence of the problem is sufficiently fast.

In Fig. 4.5d and 4.5e the difference and relative error between  $\chi_{true}$  and  $\chi^*$  are depicted; the relative error is point-wise defined by

$$\tau = \frac{|\chi^* - \chi_{true}|}{|\chi_{true}|}. \quad (4.36)$$

A maximum relative error 0.05 is quite acceptable. Based on these results, we conclude that the twin experiment is successful.

### 4.3.3. EXPERIMENT DESIGN

Based on the numerical identical-twin experiment, a real experiment for the characterization of the magnetic materials can be designed as follows. The performance of the estimation method is dependent on the chosen measurement configuration. The twin experiment could be used to determine the optimal sensor configuration. Start with defining a true magnetic susceptibility pattern  $\chi_{true}$ . If no a priori knowledge about the material is known (such as anomalies in the material), the pattern  $\chi_{true}$  should be chosen uniformly. For given sensor configuration  $S$ , let  $\chi_S$  denote the corresponding solution of the **MSEM**. To find an optimal sensor configuration, we could solve the following minimization problem

$$S^* = \underset{S \in \mathcal{S}}{\operatorname{argmin}} V_N(S) \quad (4.37)$$

where  $N$  is the size of the susceptibility pattern (dependent on the chosen mesh),  $\mathcal{S}$  is the set of all possible sensor configurations, and

$$V_N(S) = \sum_{i=1}^N (\chi_S(i) - \chi_{true}(i))^2 \quad (4.38)$$

is the empirical variance in the susceptibility pattern. Note that the solution depends on the chosen true pattern  $\chi_{true}$ .

Furthermore, as a rule of thumb the measurements should take place near the magnetic object, and in such a way that the shape of the induced magnetic field is represented in the data set. If the measurements take place too far away from the magnetic object, than the method is not able to determine the local variations of the  $\chi$ -pattern inside the magnetic

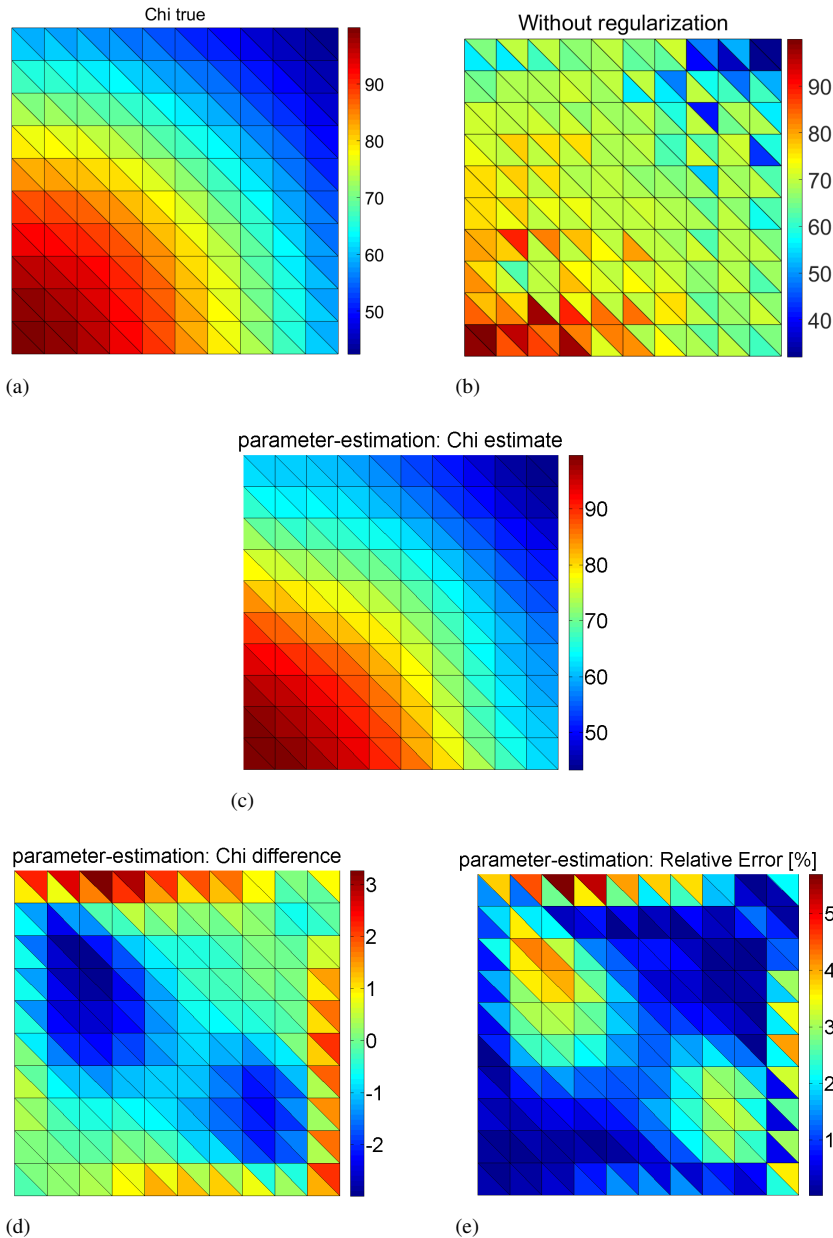
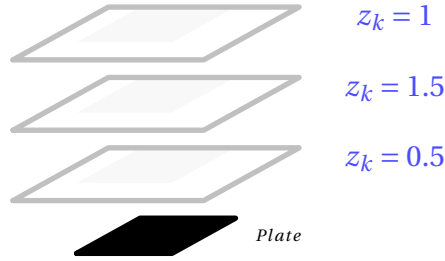


Figure 4.5: Twin-experiment results for **MSEM**: spatial distributions (a)  $\chi_{true}$ , (b)  $\hat{\chi}$  (without regularization), (c)  $\chi^*$  (with regularization), (d) absolute error  $\chi^* - \chi_{true}$ , (e) relative error  $(\chi^* - \chi_{true})/\chi_{true}$ .



Figuur 4.6: Measurements planes above plate for several values of  $z$ .

4

object. If an optimal sensor configuration is found using this routine, a real experiment can be defined to determine the magnetic susceptibility of a real magnetic object.

Lastly, note that we have assumed that there is no permanent magnetization present in the magnetic object. In practice, there is a permanent component present. Therefore, any data set of measurements of the magnetic field is spoiled by this component. One should filter out this contribution in the data set first, before it can be used in the **MSEM** method. This is easily done by considering two measurements of the magnetic object in different background fields. By a suitable subtraction one is left with a data set that is related to the linear behavior and can be used for the estimation method.

#### 4.4. SENSITIVITY ANALYSIS

In the identification of magnetic states of objects it is evident that an accurate estimation of  $\chi$  is required. By means of the **MEMS** method, we can estimate the true  $\chi$ -distribution in some magnetic object. However, small differences between the estimation and the true distribution will remain, and it is important to understand how this difference propagates in the reduced magnetic field at larger distances. The purpose of this section is to understand the statistical properties of the forward model described in (4.12).

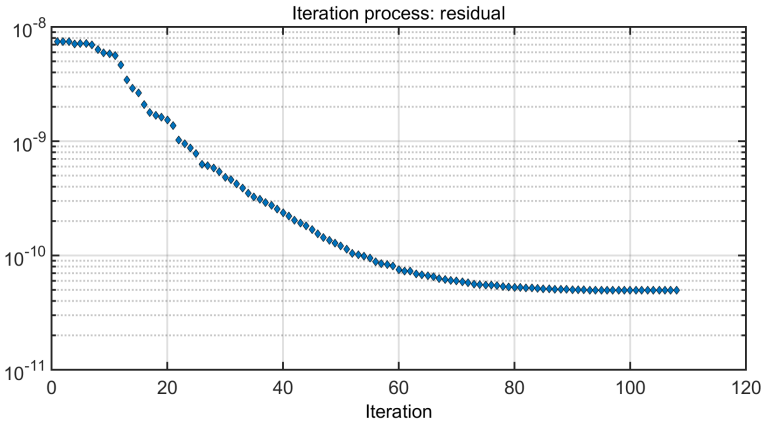
##### 4.4.1. FORWARD PROPAGATION OF MAGNETIC SUSCEPTIBILITY

We investigate the statistical properties of the forward problem, by means of a Monte Carlo simulation. As before, consider a square plate with sides of 1 meter and a thickness of 10 mm. Discretize the square plate into 200 triangular elements and assume that the magnetic susceptibility is 100 on each triangular element; denote this magnetic susceptibility distribution by  $\chi_0$ . Define a realization of the magnetic susceptibility in the Monte Carlo simulation by

$$\chi_k = \chi_0 + (\Delta\chi)_k, \quad (\Delta\chi)_k \sim \mathcal{N}(0, \sigma^2) \quad (4.39)$$

for each  $k = 1, 2, \dots, N$ , where  $N$  denotes the sample size in the Monte Carlo simulation. In our Monte Carlo simulation we set  $N = 1000$ . For  $\chi_0$  and each realization  $\chi_k$  we compute the reduced magnetic induction field in a several planes above the plate. See Fig. 4.6.

In each plane, we compare the magnetic induction field corresponding to  $\chi_0$ , denoted by  $\mathbf{B}_0^z$ , with the magnetic induction fields  $\mathbf{B}_k^z$  of the realizations at height  $z$ . These comparisons



Figur 4.7: Values of the residual function during the iterative process.

give rise to the relative error and maximum error at height  $z$  defined by

$$\tau_k^z = \frac{\|\mathbf{B}_0^z - \mathbf{B}_k^z\|_2}{\|\mathbf{B}_0^z\|_2} \quad (4.40)$$

and

$$\varepsilon_k^z = \|\mathbf{B}_0^z - \mathbf{B}_k^z\|_2 \quad (4.41)$$

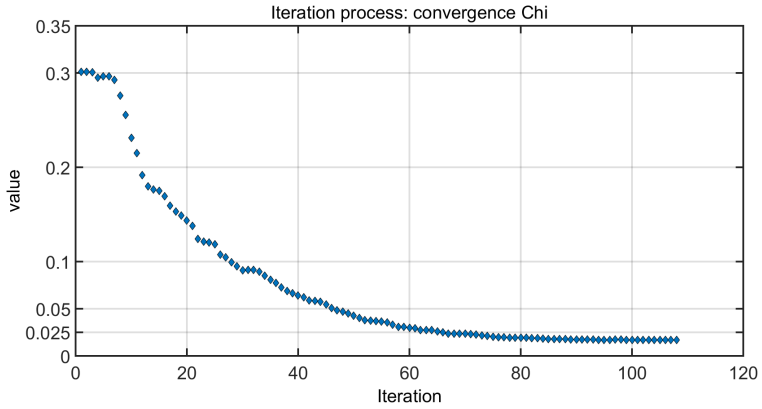
for each realization  $k = 1, 2, \dots, N$ . The mean values

$$\tau^z = \frac{1}{N} \sum_{k=1}^N \tau_k^z \quad \text{and} \quad \varepsilon^z = \frac{1}{N} \sum_{k=1}^N \varepsilon_k^z \quad (4.42)$$

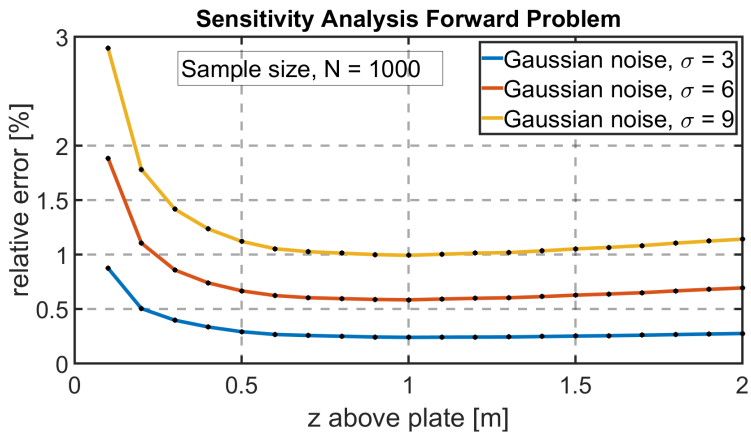
are shown in Fig. 4.9 and Fig. 4.10, for several values of  $\sigma$ . In this analysis we considered the values  $\sigma = 3, 6, 9$ . Using a rule of thumb for Gaussian distributions this implies that the variations  $(\Delta\chi)_k$  falls within the interval  $[-3\sigma, 3\sigma]$  with a probability of 0.99. This means that we consider variations in each component in the order of 10, 20 and 30 nanotesla respectively.

Note that the absolute error vanishes for increasing  $z$ , as expected. For  $z \geq 1$  m the variations  $(\Delta\chi)_k$  are not visible anymore. However, if we look at the relative errors, the relative error becomes constant<sup>3</sup> for larger  $z$ . This is also as expected, as the magnetic intensity of the field decreases as  $\frac{1}{r^3}$ , where  $r$  is the distance from the source.

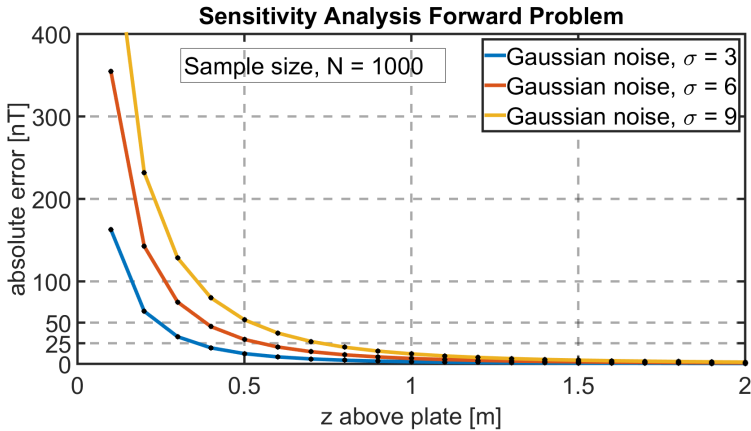
<sup>3</sup>Indeed, the values for the relative errors at  $z = 2$  are slightly higher, but this is probably due to numerical errors in the computations.



Figuur 4.8: The relative error in  $\chi$  during the iterative process.



Figuur 4.9: Monte-Carlo simulation results for system (4.13). The maximum mean relative error between the true magnetic field and the computed fields.



Figur 4.10: Monte-Carlo simulation results for system (4.13). The maximum mean absolute error between the true magnetic field and the computed fields.

## 4.5. CONCLUSION

In this chapter, we proposed a method to estimate the magnetic susceptibility of a magnetic object. This method can be applied to any (ferro)-magnetic material, under the assumption that the object itself has a sufficiently small thickness compared to the other dimensions of the object. The estimation method is based on a nonlinear least-squares optimization problem, and is solved via the BFGS method. Based on an identical-twin experiment, we have seen that the method shows a very good fit; under reasonable large measurement errors, the **MSEM** method is still able to estimate an accurate distribution of the magnetic susceptibility. An interesting next step is to see how the parameter method performs in practice.

Moreover, a sensitivity analysis has shown that it is not strictly necessary to estimate the magnetic susceptibility distribution with a high accuracy, if we want to use these distributions in accurate descriptions of the reduced magnetic field. Small variations in the magnetic susceptibility distribution are only locally observable in the induced magnetic field. Based on an error analysis, the local variations in the magnetic susceptibility in a square plate are not visible in the induced magnetic field at a distance approximately the size of the plate.

Future work is to test and validate the **MSEM** method on a real magnetic plate. Using experimental data it should become clear to what extent the method is able to estimate the magnetic susceptibility distribution accurately. However, this is not an easy task as the true magnetic susceptibility distribution is unknown in practice. Therefore, validation of the results will be complicated. An experimental design can be developed to determine which measurements are necessary to obtain the magnetic susceptibility of magnetic materials.

## REFERENCES

- [1] L. Bengtsson, M. Ghil, E. Källén (Eds.). *Dynamic Meteorology: Data Assimilation Methods*. Springer, New York. 1981. p. 330.
- [2] D. Calvetti and E. Somersalo. *Introduction to Bayesian Scientific Computing*. Springer-Verlag, New York Inc. 2007.
- [3] O. Chadebec, J. L. Coulomb, J. P. Bongiraud, G. Cauffet, and P. Le Thiec. Recent improvements for solving inverse magnetostatic problem applied to thin hulls. *IEEE Trans. on Magn.*, Vol. 38, no. 2, pp. 1005–1008, 2002.
- [4] O. Chadebec, J. L. Coulomb, G. Cauffet, and J. P. Bongiraud. How to Well Pose a Magnetization Identification Problem. *IEEE Trans. on Magn.*. Vol. 39. No. 3. pp: 1634–1637. 2003.
- [5] M. B. Giles and N. A. Pierce. An introduction to the Adjoint Approach to Design. *Flow, Turbulence and Combustion*. No. 65. 2000.
- [6] P. C. Hansen and D. P. O’leary. The use of the L-curve in the regularization of discretization of discrete ill-posed problem. *J. Sci. Comput.* 14. pp: 1487 – 1503. 1993.
- [7] John. J. Holmes. *Exploitation of A Ship’s Magnetic Field Signatures*. Morgan & Claypool publ. Inc. 2006.
- [8] John. J. Holmes. *Modeling a Ship’s Ferromagnetic Signatures*. Morgan & Claypool publ. Inc. 2007.
- [9] John. J. Holmes. *Reduction of a Ship’s Magnetic Field Signatures*. Morgan & Claypool publ., Inc. 2008.
- [10] J. D. Jackson. *Classical Electrodynamics*. 3rd ed. New York: John Wiley & Sons, Inc. 1999.
- [11] D. Jiles and D. Atherton. Theory on Ferromagnetic Hysteresis. *Journal of Magnetism and Magnetic Materials* 61. Vol: 48. 1986.
- [12] B. Kressler, L. de Rochefort, T. Liu, P. Spincemaille, Q. Jiang and Y. Wang. Nonlinear Regularization for Per Voxel Estimation of Magnetic Susceptibility Distributions From MRI Field Maps. *IEEE Trans. Medical Imaging*. Vol. 29. No. 2. pp: 273 – 281. 2010.
- [13] J. Nocedal, S. J. Wright. *Numerical Optimization*. USA: Springer Text. 1999.
- [14] J.A. Osborn. Demagnetizing Factors of the General Ellipsoid. *Physical Review*. Vol. 67. No. 11 and 12. 1945.
- [15] Néstor G., Sepúlveda, Ian M. Thomas, and John P. Wiksw, Jr.. Magnetic Susceptibility Tomography for Three- Dimensional Imaging of Diamagnetic and Paramagnetic Objects. *IEEE Trans. on Magn.*. Vol. 30. No. 6. pp: 5062 – 5069. 1994.

- [16] O. J. G. Somsen, G. P. M. Wagemakers. Separating Permanent and Induced Magnetic Signature: A Simple Approach. *International Journal of Electrical, Computer, Energetic, Electronic and Communication Engineering*. Vol: 9. No. 10. 2015.
- [17] L. Sun, X. Liu, D. Jia, and H. Niu. Three-dimensional stress-induced magnetic anisotropic constitutive model for ferromagnetic material in low intensity magnetic field. *American Insitute of Physics*. 2016.
- [18] Edward. D. Torre. *Magnetic Hysteresis*. Wiley-IEEE Press. 1999.
- [19] Y. Vuillermet, O. Chadabec, J. L. Coulomb, J. P. Bongiraud, G. Cauffet and P. Le Thiec. Scalar Potential Formulation and Inverse Problem Applied to Thin Magnetic Sheets. *IEEE Trans. on Magn.*. Vol. 44. No. 6. 2008.
- [20] M. A. Zaman, P. C. Hansen. L. T. Neustock, P. Padhy and L. Hesselink. Adjoint Method for Estimating Jiles-Atherton Hysteresis Model Parameters. *Journal of Applied Physics*. No. 120. 2016.

## APPENDIX A. APPLICATION OF THE ADJOINT METHOD FOR GRADIENT COMPUTATIONS

In this appendix the gradient of the object functionals (4.20) and (4.28) are computed, by means of the adjoint method [5, 20]. The adjoint method is a technique to obtain the gradient of an implicit nonlinear function with respect to variables for which the derivative is not obtained through a direct computation. By considering the variation of the function and the underlying physical model, one can introduce a dummy variable that makes it possible to obtain an analytical expression for this derivative. In fact, the adjoint method is similar to the application of a Lagrange multiplier method.

In the first step, note that the underlying physical model, the discretised integral equation for  $\mathbf{M}$ , can be written as

$$F(\mathbf{M}, \chi) = \mathbf{0} \quad (43)$$

where  $F$  reads

$$F(\mathbf{M}, \chi) := \left[ \sum_{k=1}^{N_e} \frac{1}{\chi_k} D_k + A + B \right] \mathbf{M} - \mathbf{h}_0 \quad (44)$$

Thus, feasible pairs of magnetisation and susceptibility distributions  $(\mathbf{M}, \chi)$  satisfy (43). This is an crucial observation that is used in the adjoint method. Recall that actually  $\mathbf{M}$  is a derived quantity in our model, based on the a priori known magnetic susceptibility distribution and the known applied magnetic field  $\mathbf{h}_0$ .

The idea behind the adjoint method now is to consider the object functional

$$\mathcal{J}(\chi) = \frac{1}{2} \mathbf{Res}^T W \mathbf{Res} - L^T F(\mathbf{M}, \chi) \quad (45)$$

which is equivalent to (4.20) and where  $L$  is called the adjoint variable. Note that  $L$  acts as a Lagrange multiplier and therefore we can assign any value to  $L$  such that the mentioned equivalence still holds. As a result, we have introduced extra freedom that allows us to obtain the gradient of the object functionals as the two object functions are equivalent for each choice of  $L$ , due to (43). Using the total derivative of the functional (45), variation of  $\mathcal{J}$  with respect to variable  $\chi_j$  is given by

$$\begin{aligned} \Delta \mathcal{J}_j &= \mathbf{Res}^T W \frac{\partial \mathbf{Res}}{\partial \mathbf{M}} \Delta \mathbf{M} - L^T \left( \frac{\partial F}{\partial \mathbf{M}} \Delta \mathbf{M} + \frac{\partial F}{\partial \chi_j} \Delta \chi_j \right) \\ &= -L^T \frac{\partial F}{\partial \chi_j} \Delta \chi_j + \left( g^T - L^T \frac{\partial F}{\partial \mathbf{M}} \right) \Delta \mathbf{M} \end{aligned} \quad (46)$$

where  $g^T$  is given by

$$g^T := \mathbf{Res}^T W \frac{\partial \mathbf{Res}}{\partial \mathbf{M}}. \quad (47)$$

The variation is now in terms of a variation in  $\mathcal{J}_j$  and in the magnetisation. But because the magnetisation is nested in a complex way in our model, it is hard to retrieve values for this variations in  $\mathbf{M}$ . Therefore, we want to get rid of this term. This is where the essential idea behind the adjoint method comes in. Choose the adjoint variable  $L$  such that the last term in (46) vanishes by solving

$$\left( \frac{\partial F}{\partial \mathbf{M}} \right)^T L = g. \quad (48)$$

Using the discretised model, the above equation reduces to a system of linear equations that can be solved using traditional methods, depending on the numerical properties of the system at hand. For this choice of  $L$  the  $j$ th component of the gradient of (4.20) reads

$$(\nabla \mathcal{J})_j := \lim_{\Delta \chi_j \rightarrow 0} \frac{\Delta \mathcal{J}_j}{\Delta \chi_j} = -L^T \frac{\partial F}{\partial \chi_j} \quad (49)$$

It remains to derive analytical expressions for the partial derivatives in (46). Some fruitful computations yields

$$\frac{\partial F}{\partial \mathbf{M}} = \sum_{k=1}^{N_g} \frac{1}{\chi_k} D_k + A + B, \quad \frac{\partial F}{\partial \chi_j} = -\frac{1}{\chi_k^2} D_k \mathbf{M} \quad (50)$$

The partial derivative  $\frac{\partial \mathbf{Res}}{\partial \mathbf{M}}$  is in general difficult to compute, but (4.18) yields that

$$\frac{\partial \mathbf{Res}}{\partial \mathbf{M}} = C(\mathcal{M}) \quad (51)$$

Next, the gradient of (4.28) is computed. Using the previous computations, only the gradient of the second term in this expression remains. A simple computation shows that

$$\nabla \left[ \frac{1}{2} (\chi - \chi_0)^T R^T R (\chi - \chi_0) \right] = R^T R (\chi - \chi_0) \quad (52)$$

because  $R^T R$  is symmetric. Combining results (49) and (52) yield the gradient of (4.28).

## APPENDIX B. APPLICATION OF THE DIVERGENCE THEOREM OF GAUSS DURING THE DERIVATION OF THE METHOD OF MOMENTS.

In the derivation of the integral equation, We observed a subtle detail in the derivation of the  $\mathbf{M}$ -formulation.

Based on the derivation described in [3], the divergence theorem of Gauss is applied to the integral

$$\nabla \iint_{e_k} \frac{\mathbf{c} - \mathbf{r}'}{|\mathbf{c} - \mathbf{r}'|^3} \cdot \mathbf{M}_k dS$$

(where  $e_k$  is two-dimensional surface element and  $\mathbf{c}$  is the barycenter of  $e_k$ ) to transform the surface integral into an integral over the boundary of  $e_k$  given by

$$\iint_{\partial e_k} \frac{\mathbf{c} - \mathbf{r}'}{|\mathbf{c} - \mathbf{r}'|^3} (\mathbf{M}_k \cdot \mathbf{n}') dL$$

However, a necessary condition to be able to apply the divergence theorem is that the integrand itself is *smooth* on  $e_k$ . This is obviously not the case, because  $\mathbf{c} \in e_k$ . So the vector function has a singularity and is not smooth on  $e_k$ . Therefore, we are not allowed to directly apply the divergence theorem of Gauss.

To overcome this technicality, we should postpone the reduction of the three-dimensional object  $\Omega$  to a two-dimensional one and consider the integral over a three-dimensional element  $e_k$

$$\nabla \iiint_{e_k} \frac{\mathbf{c} - \mathbf{r}'}{|\mathbf{c} - \mathbf{r}'|^3} \cdot \mathbf{M}_k dS$$

where  $\mathbf{c}$  is the barycenter of  $e_k$ . Take  $\varepsilon > 0$  so small such that  $B_\varepsilon[\mathbf{c}] \subseteq e_k^\circ$ , where  $B_\varepsilon[\mathbf{c}]$  is the closed ball with radius  $\varepsilon$  and center  $\mathbf{c}$ . We consider the integral, but now with the integration domain  $e_k \setminus B_\varepsilon[\mathbf{c}]$ . Note that the vector function is smooth on this integration domain. Using the divergence theorem we get for all points  $\mathbf{r}^* \in B_{\frac{1}{2}\varepsilon}(\mathbf{c})$  in a neighborhood of  $\mathbf{c}$  that

$$\begin{aligned} \nabla \iiint_{e_k \setminus B_\varepsilon[\mathbf{c}]} \frac{\mathbf{r}^* - \mathbf{r}'}{|\mathbf{r}^* - \mathbf{r}'|^3} \cdot \mathbf{M}_k dS' &= \nabla \iint_{\partial e_k} \frac{1}{|\mathbf{r}^* - \mathbf{r}'|} (\mathbf{M}_k \cdot \mathbf{n}') dS' - \nabla \iint_{\partial B_\varepsilon[\mathbf{c}]} \frac{1}{|\mathbf{r}^* - \mathbf{r}'|} (\mathbf{M}_k \cdot \mathbf{n}') dS' \\ &= - \iint_{\partial e_k} \frac{\mathbf{r}^* - \mathbf{r}'}{|\mathbf{r}^* - \mathbf{r}'|^3} (\mathbf{M}_k \cdot \mathbf{n}') dS' + \iint_{\partial B_\varepsilon[\mathbf{c}]} \frac{\mathbf{r}^* - \mathbf{r}'}{|\mathbf{r}^* - \mathbf{r}'|^3} (\mathbf{M}_k \cdot \mathbf{n}') dS' \end{aligned}$$

Furthermore, using spherical coordinates one can show

$$\iint_{\partial B_\varepsilon[\mathbf{c}]} \frac{\mathbf{c} - \mathbf{r}'}{|\mathbf{c} - \mathbf{r}'|^3} (\mathbf{M}_k \cdot \mathbf{n}') dS' = \frac{4\pi}{3} \varepsilon^2 \mathbf{M}_k$$

First observe that  $\mathbf{n}'$  is the inwards normal vector for this integration domain and that the normal vector can be written as  $\mathbf{n}'(\mathbf{r}') = \frac{\mathbf{c} - \mathbf{r}'}{|\mathbf{c} - \mathbf{r}'|}$ , and  $\frac{1}{|\mathbf{c} - \mathbf{r}'|^2} = \frac{1}{\varepsilon^2}$ . Transform the integral into an integral over  $\mathbb{S}^2$  and apply spherical coordinates to obtain the value of the integral.

Taking the limit  $\varepsilon \downarrow 0$  we get

$$\begin{aligned}
 \nabla \iiint_{e_k} \frac{\mathbf{c} - \mathbf{r}'}{|\mathbf{c} - \mathbf{r}'|^3} \cdot \mathbf{M}_k dS &= \lim_{\varepsilon \downarrow 0} \nabla \iiint_{e_k \setminus B_\varepsilon(\mathbf{c})} \frac{\mathbf{c} - \mathbf{r}'}{|\mathbf{c} - \mathbf{r}'|^3} \cdot \mathbf{M}_k dS \\
 &= \lim_{\varepsilon \downarrow 0} \left( - \iint_{\partial e_k} \frac{\mathbf{c} - \mathbf{r}'}{|\mathbf{c} - \mathbf{r}'|^3} (\mathbf{M}_k \cdot \mathbf{n}') dS + \iint_{\partial B_\varepsilon(\mathbf{c})} \frac{\mathbf{c} - \mathbf{r}'}{|\mathbf{c} - \mathbf{r}'|^3} (\mathbf{M}_k \cdot \mathbf{n}') dS \right) \\
 &= \lim_{\varepsilon \downarrow 0} \left( - \iint_{\partial e_k} \frac{\mathbf{c} - \mathbf{r}'}{|\mathbf{c} - \mathbf{r}'|^3} (\mathbf{M}_k \cdot \mathbf{n}') dS + \frac{4\pi}{3} \varepsilon^2 \mathbf{M}_k \right) \\
 &= - \iint_{\partial e_k} \frac{\mathbf{c} - \mathbf{r}'}{|\mathbf{c} - \mathbf{r}'|^3} (\mathbf{M}_k \cdot \mathbf{n}') dS
 \end{aligned}$$

$$\nabla \iint_{e_k} \frac{\mathbf{c} - \mathbf{r}'}{|\mathbf{c} - \mathbf{r}'|^3} \cdot \mathbf{M}_k dS = \iint_{\partial e_k} \frac{\mathbf{c} - \mathbf{r}'}{|\mathbf{c} - \mathbf{r}'|^3} (\mathbf{M}_k \cdot \mathbf{n}') dS$$

The boundary of  $e_k$  consists of 5 faces. Now using that the magnetization of  $\mathbf{M}$  is tangential to  $\Omega$  and that  $\Omega$  is a thin sheet leads to

$$\nabla \iiint_{e_k} \frac{\mathbf{c} - \mathbf{r}'}{|\mathbf{c} - \mathbf{r}'|^3} \cdot \mathbf{M}_k dS = t \int_{L_k} \frac{\mathbf{c} - \mathbf{r}'}{|\mathbf{c} - \mathbf{r}'|^3} (\mathbf{M}_k \cdot \mathbf{n}') dS$$

where  $L_k$  is the edge of  $e_k$ , which is the two-dimensional projected copy of  $e_k$ . We conclude that equations (4) and (5) are in equivalent.



# 5

## PARAMETER ESTIMATION FOR THE JILES-ATHERTON MODEL IN WEAK FIELDS

*This chapter is based on:*

*Aad Vijn, Olivier Baas and Eugene Lepelaars. Parameter estimation for the Jiles-Atherton model in weak fields. IEEE Trans. on Magn. Vol: 56, Issue: 4. (2020)*

### ABSTRACT

*The purpose of this chapter is to estimate the parameters of the Jiles-Atherton hysteresis model, based on minor-loop measurement data in weak applied fields. The well-known hysteresis model by Jiles and Atherton serves as a basis of this work with an extension for closure of minor loops. In order to represent minor loops correctly, a dissipative factor is introduced. A methodology to obtain the initial magnetisation of a specimen is defined, based on an expansion in terms of higher-order Gaussian functions. The methodology is implemented within a finite-element method using an interconnection between MATLAB and COMSOL. This interconnection allows the investigation of potentially large ferromagnetic objects to be calibrated for the proposed ferromagnetic model in weak fields. The proposed methodology was verified using an original approach. The approach relies on the use of a sensor array that makes it possible to detect local variations of magnetic properties in steel plates. Material parameters for our test specimen are successfully obtained by means of experimental data, using the Shuffled Frog Leaping optimisation algorithm. An analysis of the obtained results show that the calibrated model is able to represent the measurement data accurately.*

## 5.1. INTRODUCTION

Accurate modeling of ferromagnetic behavior requires a complete representation of the material hysteresis properties. Over the past century, a large number of phenomenological and mathematical-physical models were presented to describe this behavior, with various success. Well known examples are the mathematical models by Preisach [37], Play-& Stop models [3, 28, 29], the hysteresis model proposed by Tellinen [35, 44], a simple formalism that is based on physics-based concepts described by Jiles and Atherton [17, 43], the energy-variational model by Henrotte et al. [12, 24, 34] and simplistic models such as the hysteresis model by Lord Rayleigh [20]. It is interesting to note that the Rayleigh Model is related to the Preisach Model [14], while the Play-& Stop models are a generalisation of the Preisach methodology.

These models each have their own challenges and advantages considering the representation of the model of the nature of ferromagnetism, numerical stability of implementations and effective descriptions of parameter estimation algorithms. All are able to capture a large portion of the nonlinear ferromagnetic behavior, while for a subset of these models extensions to temperature, temporal and stress-related effects are known. However, if one analyses the numerical stability of the proposed models, it can be observed that, for example, implementations of the Rayleigh and Jiles-Atherton model exhibit numerical difficulties, as the magnetic field  $\mathbf{H}$  can change of value rapidly as a response of material to its magnetising field. Sophisticated numerical solvers are then necessary to obtain stable integration of these models by, for example, incorporating an inner-iterative scheme that stabilises the numerical integration. Such an inner-iterative scheme is also proposed for the Energy-variational model [34].

One drawback for the Jiles and Atherton model is that model results lead to properties that are not observed in experimental data. In the original model, minor loops are not closed which leads to unfavorable behavior in the hysteresis curve as the model encounters difficulties in representing a hysteresis curve. In [1, 4, 7, 8, 15, 17, 22, 27] the authors address and discuss possible modifications to the Jiles and Atherton model to resolve this issue. In contrast, Preisach modeling, the Play-& Stop models and the Energy-variational model (and others) ensure minor loop closure.

In more detail, the following adjustments have been proposed to the model of Jiles and Atherton to resolve the above-mentioned issue. Jiles [17] proposed a modification of the differential equation that describes the irreversible component of the magnetisation, Carpenter [4] describes scaling factors to ensure closure of minor loops. Furthermore, in the original paper of Jiles and Atherton [17] the dependencies of the material parameter  $k$  on the magnetisation is discussed. It seems that taking  $k$  constant leads to such nonclosure behavior too. Leite [27] introduced a slight modification of the irreversible component of the magnetisation in order to close minor loops. By introducing a dissipative factor  $R$  in the differential equation that describes irreversible magnetisation, it is possible to properly close minor loops. In particular, the factor  $R$  depends on the magnetic field value at a reversal point of a minor loop. We will refer to this modified version of the model by Jiles and Atherton as the **JA+R** model, to emphasize the addition of this dissipative factor  $R$ . This extended hysteresis model will serve as our choice of model throughout this chapter.

In order to find a good fit between measured hysteresis curves and a hysteresis model, a parameter fit algorithm is required to find the optimal material parameters. Many numerical

procedures and algorithms have been explored and proposed, see [18, 27, 33, 42]. This is a challenging problem because of the nonlinear nature of hysteresis. It is common practice to consider the major hysteresis loop for determination of the parameters. However, obtaining the major loop of a specimen requires the application of large applied field strengths which imposes extra requirements on the measuring equipment. It is also likely that such procedures severely limit the size of a specimen that can be investigated. There are numerous papers concerning parameter estimation, for example parameter estimation for JA [1, 10, 11, 27, 39] and estimation of the parameters of Play-& Stop models [28, 29] in which the authors use slightly minor hysteresis loop measurement data, because of the difficulty in measuring major hysteresis curves due to either the strong demagnetising fields or the required applied field strengths. Among these papers, optimisation algorithms are proposed to find a feasible set of parameters in the JA model. It has been observed that the genetic algorithm showed effective applications in finding these sets of parameters. However, one should be careful with applying the genetic algorithm, as the convergence may only be local.

The main contribution in this chapter is the following: Using **JA+R**, we have developed a methodology that estimates the material parameters in the **JA+R** model based on minor loop hysteresis curve measurements. This methodology is applied on large ferromagnetic objects, such as square steel plates; other geometrical shapes and ferromagnetic materials are also possible. Furthermore, we assume that the material parameters are uniform over the domain of the object and we assume the material is anisotropic (Though the proposed methodology is defined for the general case of inhomogeneous and anisotropic material). Therefore, only a small number of material parameters are sought. Based on measurements of minor loops, in which we vary the weak background field in the order of a few hundred microtesla, an estimation of the material parameters and the dissipative factor is done using a population-based search algorithm, which searches for a global optimum.

It is important to note that the current choice of hysteresis model is not a core aspect in this methodology. In principle it is possible to use alternative hysteresis models for which the parameters can be estimated using the same scheme. The emphasis in the current chapter is on the determination of material parameters in weak fields. All aspects of this proposed methodology are implemented in the finite-element software package `Comsol Multiphysics` and controlled by `Matlab`.

This chapter has the following structure. In Section 5.2 the methodology used in the proposed formalism is discussed.

In Section 5.3, a method to determine the magnetisation distribution based on measurements and a collection of higher-order Gaussian functions is proposed. This class of radial basis functions can be used to describe magnetisation globally. In Section 5.4, we define a parameter estimation method to determine the material properties of a ferromagnetic body. This parameter estimation method is based on measurement data of minor loops and the Shuffled Frog Leaping Algorithm [30], abbreviated by SFLA.

In the latter part of the chapter, the methodology is tested in an experimental environment. The measurement setup is described in Section 5.5. In Section 5.6, we apply the proposed methodology to a collection of ferromagnetic specimens to obtain a sets of material parameters for **JA+R**. This is based on both the determination of the initial magnetisation distribution and the optimisation solver SFLA. The results and the behavior of

the optimisation process are analysed.

In Section 5.7, we conclude the chapter and discuss future recommendations. The appendices contains extra explanation about the proposed algorithm based on a flowchart diagram, and a table in which values can be found that are used to bound the search-space for the chosen numerical solver.

## ASSUMPTIONS

Throughout this chapter, the following assumptions hold:

- *Uniform background field* in the vicinity of the geometry;
- *Anisotropic material*, where tensors are given by diagonal matrices hence only the principal axes are taken into account;
- *Homogeneous material*, i.e., the material parameters do not depend on the location inside the geometry. This assumption reduces the complexity of the problem at stake significantly.

5

## 5.2. FERROMAGNETIC HYSTERESIS

In this section, a brief recap on the hysteresis model of Jiles and Atherton is given. For more details, see [2, 17, 27, 31, 37]. The main result of this section is an adapted Jiles and Atherton model, which we call the **JA+R** model, that includes both the magneto-mechanical effect up to elastic deformations and the possibility to close minor loops. Closing minor loops is essential for an accurate estimation of material parameters described in section II.D, based on minor loop measurements.

### 5.2.1. JILES-ATHERTON MODEL

Starting point is the definition of the effective field. The effective field reads

$$\mathbf{H}_e = \mathbf{H} + \mathbf{H}_m, \quad (5.1)$$

where  $\mathbf{H}$  is the total magnetic field in [ $\text{Am}^{-1}$ ],  $\mathbf{H}_m = \boldsymbol{\alpha}\mathbf{M}$  is the Weiss field in [ $\text{Am}^{-1}$ ],  $\boldsymbol{\alpha}$  is the field parameter. The magnetisation  $\mathbf{M}$  is due to magnetic domain motion and is in [ $\text{Am}^{-1}$ ]. Note that the total field is considered inside the material. Therefore, the magnetic field  $\mathbf{H}$  reads

$$\mathbf{H} = \mathbf{H}_a + \mathbf{H}_d, \quad (5.2)$$

where  $\mathbf{H}_a$  is the applied background field and  $\mathbf{H}_d$  is the demagnetizing field. Note that the value of the demagnetizing field depends on the position within the ferromagnetic body and follows from finite-element computations [16, 19].

### ANHYSYTERETIC AND (IR)REVERSIBLE MAGNETISATION

When a material starts in the demagnetized state, the ferromagnetic behavior is described by the anhysteretic magnetisation curve. The anhysteretic magnetisation curve in the  $i$ -th direction reads

$$(\mathbf{M}_{an}(\mathbf{H}_e))_i = (M_s)_i \mathcal{L} \left( \frac{\|\mathbf{H}_e\|}{a_i} \right) \frac{(H_e)_i}{\|\mathbf{H}_e\|} \quad i \in \{x, y, z\}, \quad (5.3)$$

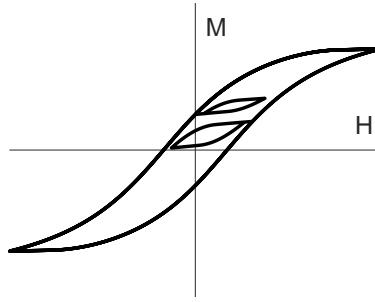


Figure 5.1: Illustration of nonclosure of minor loops in the model of Jiles and Atherton. Here, two minor loops are shown on both the increasing and decreasing branch of the minor loop. Non-closure of the minor loop is observed as the end-point of the minor loop does not coincide with the starting point of the minor loop.

where  $\mathcal{L}(x) = \coth(x) - \frac{1}{x}$  is the Langevin-function,  $(M_s)_i$  is the saturation magnetisation value in  $[\text{Am}^{-1}]$  in the  $i$ -th direction and  $a_i$  is a constant in  $[\text{Am}^{-1}]$ .

The magnetisation is considered as the sum of a reversible component  $\mathbf{M}_{rev}$  and irreversible component  $\mathbf{M}_{irr}$

$$\mathbf{M} := \mathbf{M}_{irr} + \mathbf{M}_{rev}, \quad \mathbf{M}_{rev} = \mathbf{c}(\mathbf{M}_{an} - \mathbf{M}_{irr}), \quad (5.4)$$

where  $\mathbf{M}_{irr}$  and  $\mathbf{M}_{rev}$  are in  $[\text{Am}^{-1}]$ , and  $\mathbf{c}$  is the domain rotation loss matrix. Note that when  $\mathbf{c} = \mathbf{I}$ , then  $\mathbf{M}$  is completely reversible and  $\mathbf{M}_{irr} = \mathbf{0}$ .

#### DISSIPATIVE FACTOR FOR MINOR-LOOP CLOSURE

The non-closure of minor loops in the model by Jiles and Atherton is an artifact that shows a lack of resemblance of  $\mathbf{J}\mathbf{A}$  compared to experimental data. As an example, a hysteresis curve and two minor loops are shown in Fig. 5.1, based on  $\mathbf{J}\mathbf{A}$ .

In [27], a dissipative factor is introduced that is used to close minor loops in the traditional Jiles and Atherton formalism. Note that the value of the dissipative factor for a minor loop depends on the amplitude of the corresponding applied field. The adapted differential equation [2] describing vectorial behavior of the irreversible magnetisation reads

$$d\mathbf{M}_{irr} = [\chi^{-1}(\mathbf{M}_{an} - \mathbf{R}\mathbf{M})d\mathbf{H}_e]^+, \quad (5.5)$$

where  $\chi$  and  $\mathbf{R}$  are diagonal matrices given by

$$\chi = \begin{bmatrix} \chi_1 & 0 & 0 \\ 0 & \chi_2 & 0 \\ 0 & 0 & \chi_3 \end{bmatrix} \quad \text{and} \quad \mathbf{R} = \begin{bmatrix} R_1 & 0 & 0 \\ 0 & R_2 & 0 \\ 0 & 0 & R_3 \end{bmatrix}. \quad (5.6)$$

Here,  $R_i > 0$  are dissipative factors and  $\chi_i = k_i \delta_i$  where  $k_i$  is the pinning parameter in  $[\text{Am}^{-1}]$  in the  $i$ -th direction and  $\delta_i$  is the sign of the slope of the  $i$ -th component of the effective field,  $\delta_i = \text{sign}(d(\mathbf{H}_e)_i)$ . Furthermore,  $[x]^+ := \max\{0, x\}$  is recognised as the linear activation function.

### ANISOTROPIC MATERIAL

In this chapter the simplest case of anisotropic material is considered, i.e., only along the principal axes inside the material, behavior may differ. This implies that the domain rotation loss  $\mathbf{c}$  and the field parameter  $\boldsymbol{\alpha}$  takes on the following form:

$$\mathbf{c} = \begin{bmatrix} c_1 & 0 & 0 \\ 0 & c_2 & 0 \\ 0 & 0 & c_3 \end{bmatrix} \text{ and } \boldsymbol{\alpha} = \begin{bmatrix} \alpha_1 & 0 & 0 \\ 0 & \alpha_2 & 0 \\ 0 & 0 & \alpha_3 \end{bmatrix}. \quad (5.7)$$

Note that the anisotropy assumption is already reflected in the definitions of  $\boldsymbol{\chi}$  and  $\mathbf{R}$ .

### 5.2.2. GENERAL FORM OF PDE FOR JA+R

Based on the modeling principles discussed in the previous subsections, the **JA+R** hysteresis model is defined. The general partial differential equation describing the temporal evolution of  $\mathbf{M}(t)$  in time reads

$$\frac{d\mathbf{M}}{dt} = \mathbf{c} \frac{d\mathbf{M}_{an}}{dt} + (I - \mathbf{c}) \frac{d\mathbf{M}_{irr}}{dt}, \quad (5.8)$$

for a given *initial magnetisation distribution*  $\mathbf{M}|_{t=0} = \mathbf{M}_0$ . For numerical consistency, it is necessary to indicate the value of  $\delta_i(t=0)$ , because the slope of the effective field is unknown at  $t=0$ . We choose this value based on the right-derivative of the applied field  $\mathbf{H}_a$ , i.e.,

$$\delta_i(t=0) \equiv \lim_{t \downarrow 0} \frac{(\mathbf{H}_a)_i(t) - (\mathbf{H}_a)_i(0)}{t} \quad (5.9)$$

where we tacitly assume that this signal is known a priori.

The derivative of  $\mathbf{M}_{irr}(t)$  with respect to  $t$  follows from (5.5) after differentiation with respect to  $t$

$$\frac{d\mathbf{M}_{irr}}{dt} = \left[ \boldsymbol{\chi}^{-1} (\mathbf{M}_{an} - \mathbf{R}\mathbf{M}) \frac{d\mathbf{H}_e}{dt} \right]^+. \quad (5.10)$$

Note that (5.10) follows easily after applying the chain-rule

$$\frac{d\mathbf{M}_{irr}}{dt} = \left( \frac{\partial \mathbf{M}_{irr}}{\partial \mathbf{H}_e} \right) \frac{d\mathbf{H}_e}{dt} \quad (5.11)$$

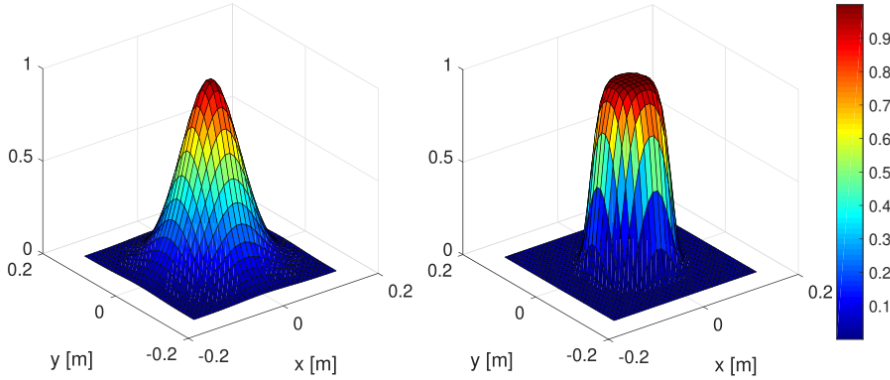
to (5.5) for both cases  $[x]^+ = 0$  and  $[x]^+ = x$  to yield (5.10).

## 5.3. INITIAL MAGNETISATION DISTRIBUTION $\mathbf{M}_0$

### GENERAL APPROACH

The initial magnetisation distribution is in general unknown. In order to find or approximate the magnetisation initially, an inverse problem has to be solved. Solving inverse problems in magnetostatics is a challenging task, see for example [5, 6, 40, 41], which often requires additional regularisation techniques for stable solutions. However, in the proposed approach below no regularisation is considered.

Defining an inverse problem for finding the magnetisation distribution is typically based on a Finite Element Method approach. In such cases, the magnetisation is described by



Figur 5.2: Two examples of higher order Gaussian functions,  $A = 1$  and  $P_x = P_y = 1$  (left) and  $A = 1$  and  $P_x = P_y = 3$  (right).

local basis functions. Typical choices for such basis functions are zeroth-order (constant functions) and linear basis functions. Higher order basis functions are usually avoided because of their complexity. Another argument is that higher order basis functions tend to be too smooth and therefore fall short in representing the solution space for  $\mathbf{M}$ .

Here, we propose a “global approach” for finding  $\mathbf{M}$ . The magnetisation distribution is described by a collection of higher order Gaussian functions<sup>1</sup>. A higher-order rectangular Gaussian function in 2D with amplitude  $A \in \mathbb{R}$ , center  $(x_c, y_c)$  and spreads  $\sigma_x, \sigma_y > 0$  reads

$$f(x, y) = A \exp \left( - \left( \frac{(x - x_c)^2}{2\sigma_x^2} \right)^{P_x} - \left( \frac{(y - y_c)^2}{2\sigma_y^2} \right)^{P_y} \right) \quad (5.12)$$

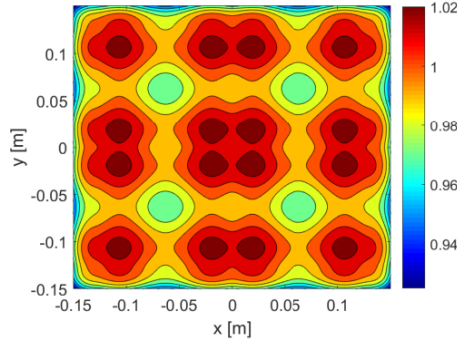
Here, the powers  $P_x$  and  $P_y$  are used to control the decay of the function. Larger values for  $P_x$  and  $P_y$  lead to a flat-top and a rapid Gaussian fall-off to zero. Two examples of these higher order Gaussian functions are given in Fig. 6.1. Notice that in the limit as  $P_x, P_y \rightarrow \infty$ , higher-order Gaussian functions correspond to basis functions with compact support. An example of a collection of Gaussian functions is given in Fig. 6.2, which can be used to approximate any constant function defined on a (square) domain. This choice of global functions also allows us to introduce magnetic anomalies inside a magnetised object.

#### DETERMINATION OF $\mathbf{M}_0$

In the remainder of this section, without loss of generality, consider a magnetised plate  $\Omega$ . Furthermore, assume a priori that centers  $(x, y) \in \Omega$ , spreads  $\sigma_x, \sigma_y > 0$  and the powers  $P_x, P_y > 0$  are fixed for a collection of Gaussian functions  $\{f_i(A_i)\}_{i=1}^n$ . Hence, only the amplitudes of the Gaussian functions are unknown and can be chosen freely.

The aim is to find the magnetisation  $\mathbf{M}$  of the plate  $\Omega$ . This is done based on measurements of the magnetic induction field  $\mathbf{B}$  at sensor locations surrounding the plate.

<sup>1</sup>Finally recall the following result from Approximation Theory: for a square interval  $[0, 1]^2$  the set of all Gaussian functions is dense in the function space  $\mathcal{C}([0, 1]^2, \mathbb{R})$ . Therefore, any component of a magnetisation can be approximated with arbitrary accuracy by a collection of  $n$  Gaussian functions, for sufficiently large  $n \in \mathbb{N}$ .



Figur 5.3: An example of a distribution of nine two-dimensional higher order square Gaussian functions,  $\sigma_x = \sigma_y = 0.05$ ,  $P_x = P_y = 1.5$  and  $A = 1$  for all Gaussian functions.

5

To that end, observe that a Gaussian function  $f_i(A_i)$  describes a magnetisation distribution  $\mathbf{M}_i = f_i(A_i)\mathbf{u}_i$  on  $\Omega$ , where  $\mathbf{u}_i$  is a unit vector. For example, if for all  $i \leq n$   $\mathbf{u}_i = \mathbf{u}_x$ , then the  $x$ -component of the magnetisation is sought.

Sub-sequentially, this magnetisation produces a magnetic induction field  $\mathbf{B}_i(A_i)$  in sensorlocations  $\mathbf{r}_1, \mathbf{r}_2, \dots, \mathbf{r}_N \in \Omega^c$ . To determine the initial magnetisation, the following linear problem has to be solved

$$\hat{\mathbf{A}} = \underset{A_1, A_2, \dots, A_n \in \mathbb{R}}{\operatorname{argmin}} \left\| \sum_{i=1}^n \mathbf{B}_i(A_i) - \mathbf{B}_m \right\|_2^2 \quad (5.13)$$

where  $\mathbf{B}_m$  is a vector that contains the measured values of the magnetic field in the sensorlocations  $\mathbf{r}_1, \mathbf{r}_2, \dots, \mathbf{r}_N$  and  $\hat{\mathbf{A}} = [A_1, A_2, \dots, A_n]^T$  is a vector containing the optimal values for amplitudes  $A_1, A_2, \dots, A_n$ . Note that the resulting vector  $\hat{\mathbf{A}}$  depends on the collected measurement data, and the sensor locations. To find the optimal sensor locations, one should vary the locations and investigate the sensitivity of the solution and fit with respect to these variations. However, finding optimal sensor locations is in general a very complex problem.

To obtain acceptable sensor configurations, one can derive configurations on the basis of minimisation of the norm of the Fisher information matrix, called the (FIM) method [21, 38]. Alternatively, the determinant or the trace of the Fisher information matrix is also a possibility. An alternative method is to minimize the expected Bayesian loss function that uses the inverse of the FIM as a measure for the quality of the sensor configuration [32]. However, information about the (model) noise is necessary, which can be hard to obtain.

## 5.4. PARAMETER ESTIMATION OF JA+R

In this section, we discuss the estimation of material parameters in the **JA+R** model. First note that there is a total of 18 parameters that fully define the model, summed up in the following matrices

$$\begin{aligned} \text{Jiles-Atherton} &\equiv \begin{bmatrix} \alpha_1 & \alpha_2 & \alpha_3 \\ (M_s)_1 & (M_s)_2 & (M_s)_3 \\ a_1 & a_2 & a_3 \\ c_1 & c_2 & c_3 \\ k_1 & k_2 & k_3 \end{bmatrix} \\ \text{Dissipative factor} &\equiv \begin{bmatrix} R_1 & R_2 & R_3 \end{bmatrix} \end{aligned} \quad (5.14)$$

where the parameters in the first, second and third columns in (5.14) correspond to the ferromagnetic behavior in the  $x$ ,  $y$  and  $z$ -direction respectively. In the latter of this report we assume for simplicity that the dissipative factors are constant such that the parameters can be stored in a single parameter vector, denoted by  $\mathbf{p} \in \mathbb{R}^{18}$ . Indeed, the values of  $R_1, R_2, R_3$  may vary in the model.

### 5.4.1. FORWARD PROBLEM

In this subsection we define the forward problem that serves as a foundation for the derivation of the parameter estimation problem. In particular, the main result in this subsection is the definition of  $\mathbf{B}_c[\mathbf{p}]$ , which is a vector that consists of computed magnetic induction field values at sensor locations for a given applied magnetic field signal.

Let  $\mathbf{B}_a : [0, t_{end}] \rightarrow \mathbb{R}^3$  be an applied background field signal and let  $\Omega$  denote a ferromagnetic object. Furthermore, assume that the initial magnetisation  $\mathbf{M}|_{t=0} = \mathbf{M}_0$  is known. Given a fixed set of material parameters for  $\mathbf{JA}+\mathbf{R}$ , the solution to the forward problem is the magnetic induction field caused by the magnetisation of  $\Omega$  at a collection of measurement locations for  $t \in [0, t_{end}]$ , when the background field signal is applied to  $\Omega$ .

If  $\mathcal{M} = \{\mathbf{r}_1, \mathbf{r}_2, \dots, \mathbf{r}_K\}$  denotes a set of  $K$  measurement locations, then  $\mathbf{B}_c(t) \in \mathbb{R}^{3K}$  is a vector that contains the magnetic induction field at the measurement locations at time  $t \in [0, t_{end}]$ .

If  $\{t_1, t_2, \dots, t_T\} \subset [0, t_{end}]$  denotes a sample of time instants, then we may form vector  $\mathbf{B}_c[\mathbf{p}] \in \mathbb{R}^{3KT}$  by concatenating the vectors  $\mathbf{B}_c(t_1), \mathbf{B}_c(t_2), \dots, \mathbf{B}_c(t_T)$  at the corresponding time instances:

$$\mathbf{B}_c[\mathbf{p}] = \text{Vec}(\mathbf{B}_c(t_1), \mathbf{B}_c(t_2), \dots, \mathbf{B}_c(t_T)) \quad (5.15)$$

### 5.4.2. MINIMIZATION PROBLEM

The idea behind parameter estimation is as follows: based on a collection of  $N$  measured minor loops, with  $T$  measurements per loop at  $K$  measurement locations, the task is to find a feasible collection of parameters  $\hat{\mathbf{p}} \in \mathbb{R}^{18}$  such that there is a good fit between the measured minor loops, and the minor loops computed by the FEM implementation in COMSOL. To measure the fit, the residual

$$\mathbf{Res} := \mathbf{B}_m - \mathbf{B}_c[\mathbf{p}] \quad (5.16)$$

is chosen. Here, the vector  $\mathbf{Res} \in \mathbb{R}^{3KNT}$  is the residual between the measured minor loops  $\mathbf{B}_m$  and the computed values of the minor loop  $\mathbf{B}_c[\mathbf{p}]$  for a given parameter vector  $\mathbf{p}$ . If the residual is small, then corresponding parameter vector  $\mathbf{p}$  is a feasible solution to the parameter estimation problem.

To define the minimization problem, we introduce the Root Mean Square Error (RMSE)

$$\mathcal{J}(\mathbf{p}) = \sqrt{\frac{\mathbf{Res}^T W \mathbf{Res}}{n}}, \quad n \equiv 3KNT. \quad (5.17)$$

The positive diagonal matrix  $W$  contains weights that can be used to control the importance of each measured point on the minor loop. For example, one should relax the fit near the tip-points of the minor loop, to increase the performance of the parameter estimation. This is achieved by choosing weights  $w_{ii}$  relatively small for tip point measurements, compared to the weights for other measurements .

### 5.4.3. SOLVING THE MINIMIZATION PROBLEM

To find the optimal values that best fit the (measured) data, a memetic meta-heuristic called the Shuffled Frog Leaping Algorithm (SFLA) is applied [23]. The SFLA is a population-based cooperative search inspired by frogs that work together to find food. The algorithm contains both elements of local search and global information exchange, and it is shown to be very efficient for finding traditional Jiles and Atherton parameters [30].

Choosing a particular bounded search space increases the speed of convergence significantly. This is done by choosing suitable boundaries for the unknowns. The minimal and maximal values for the above-mentioned parameters in the **JA+R** model are given in Appendix 5.7. These bounds are based on successively applying the SFLA to learn the behavior of the optimisation process and the already known material parameters found in the literature [18, 25, 26, 36].

Finally, in Appendix 5.7 a flowchart is shown that describes the complete parameter estimation procedure based on the initial magnetisation distribution and the SFLA.

## 5.5. MEASUREMENT SETUP

In this section the experimental setup is explained briefly. A measurement facility is available consisting of a coil configuration and a magnetic sensor array. The rectangular coil configuration can change the local ambient magnetic field by imposing a uniform magnetic field in all three directions. Fig. 5.4 shows a picture of the coil structure. Inside the cage the background field can take values of the form

$$\{\mathbf{B}_{app} \in \mathbb{R}^3 : |(\mathbf{B}_{app})_i| \leq 400 \mu\text{T for } i = x, y, z\}. \quad (5.18)$$

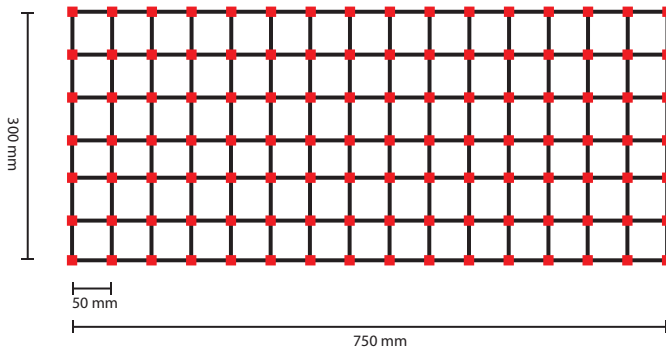
The sensor array consisting of 112 sensors is placed 56 mm below the object. To measure the magnetic field, HMC5983 Triple Axis Compass magnetometers are used. Depending on the set gain, the sensor noise is approximately  $1 \mu\text{T}$  up to  $3 \mu\text{T}$ . A schematic overview of this sensor array is found in Fig. 5.5.

## 5.6. EXPERIMENTAL RESULT

In this section, we apply the proposed parameter fit to steel specimens. The goal is to obtain the material parameters for **JA+R**. The assumptions of homogeneity and isotropy imply that there is no spatial dependency in the material parameters. Therefore five material parameters are sought, plus a dissipative factor for each measured minor loop.



Figuur 5.4: Measurement facility “CLAViS” that contains a coil configuration to change the ambient field in three directions.



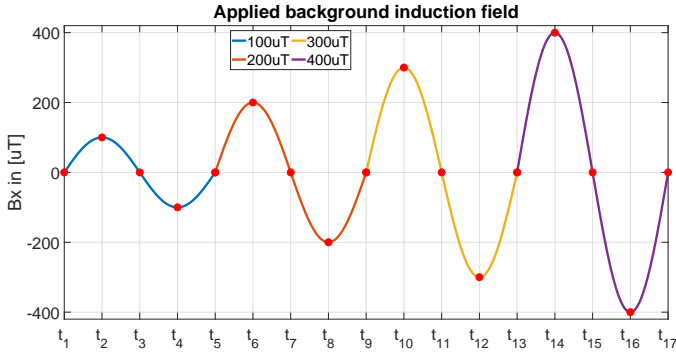
Figuur 5.5: Schematic overview of the sensor array.



Figuur 5.6: Steel plate above sensor array.

### 5.6.1. SPECIMEN DESCRIPTION

In this experiment four different specimen (I,II,III,IV) are investigated. Each specimen is a square metal plate with sides of 300 mm. Specimen I and III have a thickness of 5 mm, II



Figur 5.7: Scenario: sinusoidal background field of increasing and measurements at several instances.

and IV have a thickness of 2 mm.

Each plate is placed parallel to the sensor array in the cage, and is measured at a distance of 56 mm above the array. In Fig. 5.6 a picture is shown of the steel plate within the coil structure on top of the sensorarray.

In the remainder of this section, we take the measurement and results of **specimen I** as a guideline. The results of the other specimen are similar except for specimen III. This is likely due to the prior deperming procedure applied to this specimen, which made the initial magnetisation distribution estimation procedure additionally complicated.

### 5.6.2. MEASURING A MINOR LOOP

At the start of a measurement, the background field is set to  $0 \mu\text{T}$  in  $x$ ,  $y$ , and  $z$ -directions, which is from here on defined as  $t_1$ . Then, the background field is varied in the  $x$ -direction for one full period with an amplitude of  $A \mu\text{T}$ , where  $A \in \{100, 200, 300, 400\}$ . During this period, five distinctive time instants are defined:

- $t_A$ , the starting point when the background field is  $0 \mu\text{T}$ ;
- $t_B$ , after the background field has been increased to  $A \mu\text{T}$  in  $x$ -direction;
- $t_C$ , after the background field is reduced to  $0 \mu\text{T}$ ;
- $t_D$ , after the background field is set to  $-A \mu\text{T}$  in  $x$ -direction;
- $t_E$ , when the background field is increased back to  $0 \mu\text{T}$ .

In total, the experiment consists of measuring four minor loops subsequently. See Fig. 5.7 for clarification of the described scenario. The first measurement (at time  $t = t_1$ ) is used to determine the initial magnetisation distribution  $\mathbf{M}_0$  and we refer to Section II.C for more details on this specific routine.

### 5.6.3. INITIAL MAGNETISATION DETERMINATION

First the initial magnetisation of specimen I is determined. The measurement of the magnetic induction field (the  $x$ -component  $B_x$ ) of specimen I in zero field at time  $t = t_1$  is given

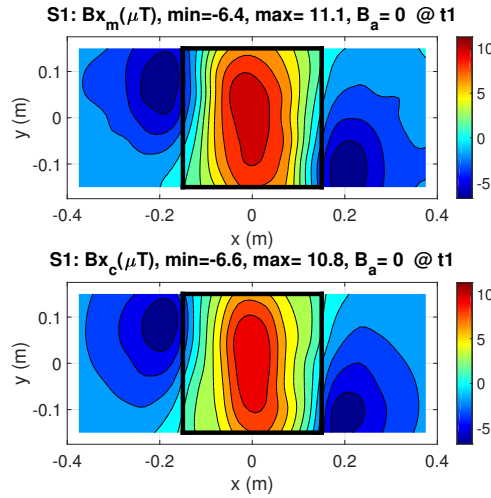


Figure 5.8: Specimen 1: (above) measured  $B_x$ -field at  $t_1$  and (below) the corresponding computed  $B_x$ -field based on the initial magnetisation distribution estimation.

in Fig. 5.8. This is a measurement in which the background field is cancelled by the coil cage.

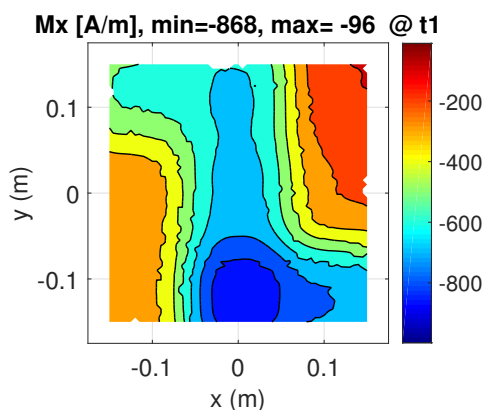
Applying the method in Section II.C leads to the following initial magnetisation distribution for which the  $x$  component of the magnetisation is given in Fig. 5.9. Here, the collection of higher-order Gaussian functions is chosen such that the resulting condition number of the linear problem is low. This is done by choosing functions that are (almost) linearly independent. By tuning the values of  $\sigma_x$  and  $\sigma_y$  such that the resulting support of the Gaussian functions is small, one can achieve such independences. Finally, solving the linear problem is done using standard Gaussian elimination (or equivalently using an  $LU$ -decomposition of the coefficient matrix).

After solving the linear problem of finding the amplitudes  $(A_i)_i^n$  of the Gaussian functions, the corresponding initial magnetisation distribution is found and given in Fig. 5.9. The erratic behavior that is seen in the initial magnetisation distribution is caused by COMSOL when the solution to the linear problem was imported to COMSOL. COMSOL translates the continuous magnetisation distribution to a discretised version on a mesh for further finite-element computations.

The resulting computed magnetic induction field for the obtained initial magnetisation distribution is found in Fig. 5.8. Compared to the measured field, there is a good agreement. The difference between the computed and measured values in terms of the RMSE is sufficiently small, and therefore we accept the estimation of this initial magnetisation distribution.

#### 5.6.4. PARAMETER ESTIMATION RESULTS

Using the initial magnetisation distribution from the previous subsection, the **JA+R** material properties are obtained using forward simulations within the SFLA as described in Section 5.4.B. The optimal parameter values for all specimen are found in Table. 5.1. In



Figur 5.9: Specimen 1: estimated initial magnetisation at time  $t_1$ . Only the  $x$ -component of the initial magnetisation is shown, as this is the dominant component of the vector field.

Tabel 5.1: JA+R parameters obtained using SFLA.

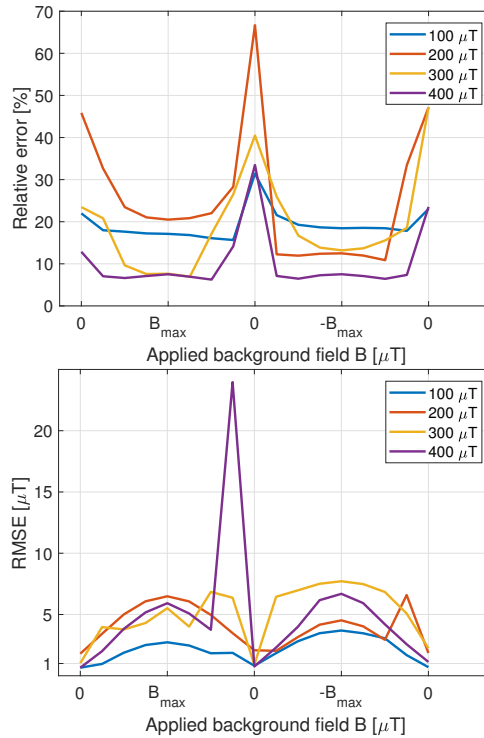
JA Parameter	I	II	III	IV	Unit
$M_s$	$1.52 \times 10^6$	$1.67 \times 10^6$	$1.52 \times 10^6$	$1.66 \times 10^6$	$\text{Am}^{-1}$
$k$	379	270	295	323	$\text{Am}^{-1}$
$a$	2565	1256	1763	379	$\text{Am}^{-1}$
$c$	0.1344	0.0974	0.1139	0.1194	-
$\alpha$	$1.793 \times 10^{-3}$	$9.929 \times 10^{-4}$	$9.884 \times 10^{-4}$	$7.777 \times 10^{-4}$	-
thickness	5	2	5	2	mm

particular, the dissipative factors  $R$  for specimen I for minor loops of amplitude  $100 \mu\text{T}$ ,  $200 \mu\text{T}$ ,  $300 \mu\text{T}$  and  $400 \mu\text{T}$  are respectively  $R_{100} = 1.5$ ,  $R_{200} = 1.2$ ,  $R_{300} = 1.1$  and  $R_{400} = 1.0$ . Note that these values are consistent with the reasoning in [27], in which it is assumed that the values of  $R$  are decreasing with increasing field strength, and such that  $R$  is bounded below by 1.

It is observed that applying the SFLA multiple times on the same problem may result in different sets of parameters for which the functional takes (approximately) the same minimal value. This implies that based on minor loop measurements the set of parameters is not unique. A consequence is that these material parameters cannot be used in the region of the hysteresis curve outside the  $400 \mu\text{T}$  minor loop, as it is expected that the hysteresis curve outside this region is poorly described by the obtained material parameters. Fortunately, for our applications this is not a limitation because we stay within the  $400 \mu\text{T}$  region for a given initial magnetisation distribution.

### 5.6.5. ERROR ANALYSIS OF SFLA RESULTS

The resulting computed magnetic induction field based on the initial magnetisation from Fig. 5.9 and optimal JA+R parameters from table 5.1 subjected to a hysteresis loop of  $400 \mu\text{T}$  for specimen I is given in figure 5.11. Based on visual inspection, a good agreement



Figuur 5.10: Specimen 1: Relative error and Root Mean Square Error.

is seen between the measured fields and the computed fields by the proposed model.

The result of error calculations for the first specimen are given in Fig 5.10. Observe that the relative error is smaller for larger minor loops. This is explained by the fact that for larger background fields the hysteresis effects are more pronounced, such that discrepancies between the measured and computed fields are relatively small. It can be observed that, as expected, the relative error becomes rather large when the background field is zero since the measured fields are much closer to 0  $\mu\text{T}$  than whenever the background field is nonzero. Therefore no strong conclusions can be made by interpreting the values of the relative error.

A better quantity to considering is the Root Mean Square Error which averages all absolute errors along the measurement locations. Observe that this error does not exceed 2  $\mu\text{T}$  whenever the background field is zero. This error is within the sensor noise level, hence the model represents our measurements very well in these cases. Unfortunately, there is a large peak in the RSME computed during a 400  $\mu\text{T}$  minor loop. A plausible explanation for this is that an error occurred while doing a measurement and that the coil configuration did not produce the correct background field. Similar arguments may hold for other minor loops, although it is not completely clear if the larger RMSE is due to malfunctioning of the equipment or to the performance of the model.

Note that for measurements in zero background field, there is a significant discrepancy between the measured and computed magnetic induction field. Nevertheless, there is a

good agreement between the measured and computed 400  $\mu\text{T}$  minor loop with a maximum RMSE error of 6  $\mu\text{T}$ . Overall, the RMSE is 10 % (see Fig. 5.11) of the average measured field strength which indicates a good fit.

In general it is also observed that there is a better agreement between the model and measurements for larger field strength amplitude. This makes sense since high amplitude field variations make larger hysteresis effects better visible. In total, based on error computations we conclude that we correctly found material parameters for the **JA+R** model and our model reproduces the measured data accurate enough.

### 5.6.6. COMPUTATIONAL EFFORT

Finally, we look at the computational effort of SFLA. The computation time is rather long. For each specimen there are 1000 evaluations of the forward problem required within the SFLA to find a good fit. This translates to a total computation time of approximately 24 hours on a high-end CPU. The computational burden is mainly caused by the communication between Matlab and COMSOL. COMSOL is used to compute the forward simulations that the SFLA require in the optimisation problem. However, each evaluation of such a forward simulation requires a fresh call to the COMSOL engine, which drastically increases the computation time. Indeed, a more sophisticated implementation of the method reduces the computation time significantly by integrating SFLA into COMSOL, so there is no need to rebuild the model every time.

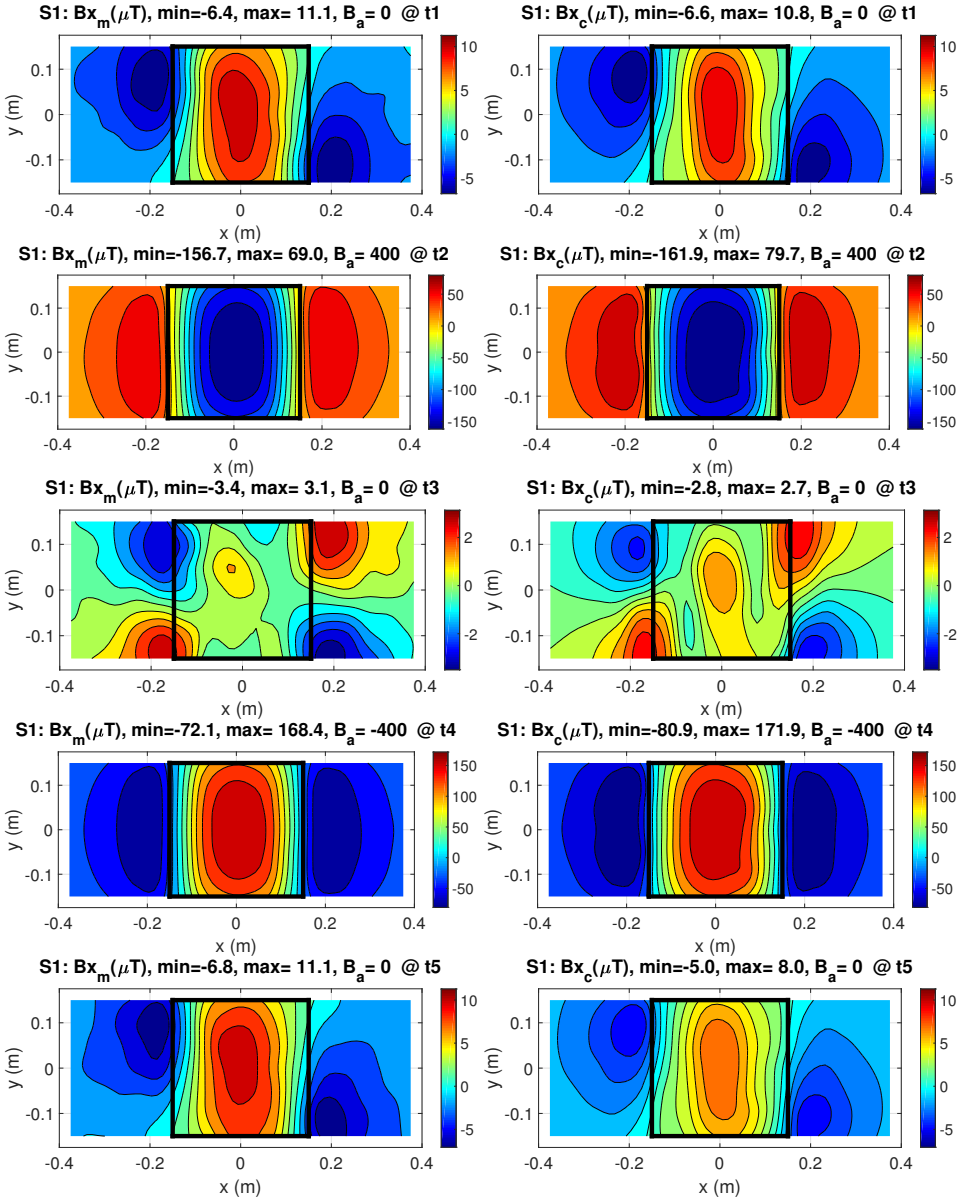
## 5.7. CONCLUSION

This chapter presented a method to estimate the material parameters of homogeneous anisotropic material in the Jiles and Atherton Model framework in weak applied fields. This estimation is based on both the hysteresis model that we refer to as **JA+R** and the optimisation algorithm called the Shuffled Leaping Frog Algorithm (SFLA). Based on a collection of minor loop measurements for steel plates in weak fields, we have shown that material parameters of a number of specimen can be obtained at the required accuracy.

The choice to use only minor loop measurements is not common and we have shown that it is possible to only use such measurements with accurate results. This increases the applicability of material estimation properties, while in other related work only material parameters are obtained using major loop measurements. Such measurements are not trivial and may not be achievable in practice. Therefore, our method is applicable in finding the material parameters in a more general setting.

The material parameters that we have found are similar to values found in the literature for different alloys of steel. This gives us confidence that our application of the proposed methodology is correctly performed. Also it is shown that the RMSE, whenever the results are compared to the measurements, is small enough. It is further noted that the performance of the method is better when the initial magnetisation is not too small. Deperming a specimen increased the complexity of finding material parameters, and therefore this is an important observation for future experiments.

Preliminary results indicate that the obtained values have some predictive power to model ferromagnetic behavior for weak fields inside the region that is used to obtain the parameters. However, more research and measurements are required to further investigate this



Figur 5.11: Specimen 1: measured (left) and computed (right) magnetic induction field component  $B_x$  at  $t_A, t_B, \dots, t_E$  for a 400  $\mu T$  minor loop measurement. Note that all field components ( $B_x, B_y, B_z$ ) are used in the computations.

predictive power in more detail, e.g., how to interpret the nonuniqueness of obtained material parameter set, as different sets are solutions to the minimisation problem as described in Section 5.4.2.

Future steps are to apply the methodology to experimental data to obtain the material parameters for the full anisotropic tensor case. Furthermore, the use of regularisation to increase the robustness of the solutions to the parameter estimation is valuable and must be incorporated in further extensions of the proposed model. This will reduce the effect of noise to the solutions. Lastly, the predictive performance of the obtained parameters is still ongoing research and must be understood in more detail.

## REFERENCES

- [1] A. Benabou et al. Minor loops modelling with a modified Jiles Atherton model and comparison with the Preisach model. *J. Magn. Magn. Mater.* pp: 320. 2008.
- [2] A. J. Bergqvist. A Simple Vector Generalization of the Jiles-Atherton Model of Hysteresis. *IEEE Trans. on Magn.*. Vol: 32. No. 5. pp: 4213 – 4215. 1996.
- [3] S. Bobbio, G. Miano, C. Serpico and C. Visone. Models of Magnetic Hysteresis Based on Play and Stop Hysteresis. *IEEE. Trans. on Magn.* Vol. 33. No. 6. 1997.
- [4] K. H. Carpenter. A Differential Equation Approach to Minor Loops in the Jiles-Atherton Hysteresis Model. *IEEE Transactions on Magnetics*, Vol: 27. No. 6. pp: 4404 – 4406. 1991.
- [5] O. Chadebec, J. L. Coulomb, J. P. Bongiraud, G. Cauffet, and P. Le Thiec. Recent improvements for solving inverse magnetostatic problem applied to thin hulls. *IEEE Trans. on Magn.*, Vol. 38, no. 2, pp. 1005–1008, 2002.
- [6] O. Chadebec, J. L. Coulomb, G. Cauffet, and J. P. Bongiraud. How to Well Pose a Magnetization Identification Problem. *IEEE Trans. on Magn.*. Vol. 39. No. 3. pp: 1634–1637. 2003.
- [7] K. Chwastek et al. Modelling dynamic hysteresis loops in steel sheets, *COMPEL*. Vol. 28. No. 3. pp: 603 – 612. 2009.
- [8] K. Chwastek. Modelling offset hysteresis loops with the modified Jiles-Atherton description. *Journal of Physics D: Applied Physics*. Vol: 42. 2009.
- [9] K. O’Grady and S. J. Greaves. Minor Hysteresis loops effects in magnetic materials. *Journal of Magnetism and Magnetic Materials* 138. pp: L233–L236. 1994.
- [10] Ch. Guérin et al. Using a Jiles-Atherton vector hysteresis model for isotropic magnetic materials with the finite element method, Newton-Raphson method, and relaxation procedure. *International Journal of Numerical Modelling, Electronic Networks, Devices and Fields*. Vol. 30. No. 5.
- [11] M. Hamimid, S.M. Mimoune, M. Feliachi. Minor hysteresis loops model based on exponential parameters scaling of the modified Jiles–Atherton model. *Physica B: Condensed Matter*. Vol. 407. No. 13. pp: 2438 – 2441. 2012.

- [12] F. Henrotte and K. Hameyer. A Dynamical Vector Hysteresis Model Based on an Energy Approach. *Trans. on Magn.*. Vol: 42. No. 4. 2006.
- [13] K. Hergli, H. Marouani, M. Zidi, Y. Fouad and M. Elshazly, Identification of Preisach hysteresis model parameters using genetic algorithms. *Journal of King Saud University – Science*. 2017.
- [14] A. Iványi (Ed.). Preisach Memorial Book. Akadémiai Kiadó, Budapest. 2005.
- [15] Z. Włodarski *et al.*. Modeling DC-biased hysteresis curves in self-developed SMC cores. *International Journal of Applied Electromagnetics and Mechanics*. Vol: 61. No. 1. pp: S151-S157. 2019.
- [16] J. D. Jackson, Classical Electrodynamics. 3rd ed. New York: John Wiley & Sons, Inc. 1999.
- [17] D. Jiles and D. Atherton. Theory on Ferromagnetic Hysteresis. *Journal of Magnetism and Magnetic Materials* 61. Vol: 48. 1986.
- [18] D. Jiles. Numerical Determination of Hysteresis Parameters for the Modeling of Magnetic Properties Using the Theory of Ferromagnetic Hysteresis. *IEEE Transactions on Magnetics*. Vol: 28. No. 1. 1992.
- [19] Jianming Jin. The Finite Element Method in Electromagnetics. New York: John Wiley & Sons, Inc. 2002.
- [20] M. Kachniarz, R. Szewczyk. Study on the Rayleigh Hysteresis Model and its Applicability in Modeling Magnetic Hysteresis Phenomenon in Ferromagnetic Materials. *Acta Physica Polonica A*. Vol: 131, No. 5. pp: 1244 – 1249. 2017.
- [21] P.H. Kirkegaard, R. Brincker. On the Optimal Locations of Sensors for Parametric Identification of Linear Structural Systems. *Mechanical Systems and Signal Processing*. Vol: 8. pp: 639 – 647. 1994.
- [22] P.I. Koltermann *et al.*, A modified Jiles method for hysteresis computation. *Physica B*. Vol: 275. pp: 233 – 237. 2000.
- [23] Muzaffar Eusuff, Kevin Lansey and Fayzul Pasha. Shuffled frog-leaping algorithm: a memetic meta-heuristic for discrete optimization. *Engineering Optimization*. Vol: 38. No.2. pp: 129 – 154. 2006.
- [24] V. François-Lavet, F. Henrotte, L. Stainier, L. Noels, and C. Geuzaine. An energy-based variational model of ferromagnetic hysteresis for finite element computations. *Journal of Computational and Applied Mathematics*. Vol: 246. pp: 243 – 250. 2013.
- [25] J.V. Leite *et al.*. The Inverse Jiles-Atherton Model Parameters Identification. *IEEE Trans. on Magn.*. Vol: 39. No. 3. pp: 1397 – 1400. 2003.
- [26] J.V. Leite *et al.*. Real coded genetic algorithm for Jiles-Atherton model parameters identification. *IEEE Trans. on Magn.*. Vol: 40. No. 2. pp: 888 – 891. 2004.

- [27] J.V. Leite, A. Benabou and N. Sadowski. Accurate minor loops calculation with a modified Jiles-Atherton hysteresis model. *COMPEL*. Vol: 28. No. 3. pp: 741 – 749. 2009.
- [28] T. Matsuo, D. Shimode, Y. Terade and M. Shimasaki. Application of Stop and Play Models to the Representation of Magnetic Characteristics of Silicon Steel Sheet. *Trans. on Magn.*, Vol. 39, No. 3, May 2003.
- [29] T. Matsuo, Y. Terada, M. Shimasaki. Representation of minor hysteresis loops of a silicon steel sheet using stop and play models. *Phys. B.* Vol: 372. pp: 25 – 29. 2006.
- [30] R. Naghizadeh, B. Vahidi and S. H. Hosseinian. Parameter identification of Jiles-Atherton model using SFLA. Vol: 31. No. 3. pp: 1293 – 1309. 2012.
- [31] H.W.L. Naus. Theoretical developments in magnetomechanics. *IEEE Trans. on Magn.* Vol: 47. No. 9. pp: 2155 – 2162. 2011.
- [32] C. Papadimitriou, J.L. Beck and S.K. AU. Entropy-Based Optimal Sensor Location for Structural Model Updating. *Journal of Vibration and Control*. Vol: 6. No. 5. pp: 781 – 800. 2000.
- [33] N.C. Pop and O.F. Caltun. Jiles–Atherton Magnetic Hysteresis Parameters Identification. *ACTA PHYSICA POLONICA A*. Vol: 120. No. 3. pp: 491 – 497. 2011.
- [34] L. Prigozhin, V. Sokolovsky, J. W. Barret, and S. Zirka. On the Energy-Based Variational Model for Vector Magnetic Hysteresis. *IEEE Trans. on Magn.* Vol: 52. No. 12. 2016.
- [35] J. Tellinen. A Simple Scalar Model for Magnetic Hysteresis. *IEEE. Trans. on Magn.* Vol: 34. No. 4. 1998.
- [36] M. Toman, G. Stumberger, and D. Dolinar. Parameter identification of the Jiles-Atherton hysteresis model using differential evolution. *IEEE Trans. on Magn.* Vol. 44. No. 6. pp: 1098 – 1101. 2019.
- [37] Edward. D. Torre. *Magnetic Hysteresis*. Wiley-IEEE Press. 1999.
- [38] F.E. Udwardia. Methodology for Optimal Sensor Locations for Parameter Identification in Dynamic Systems. *Journal of Engineering Mechanics (ASCE)*. Vol: 120. No. 2. pp: 368 – 390. 1994.
- [39] G. Vertésy et al. Minor hysteresis loops measurements for characterization of cast iron. *Physica B: Condensed Matter*. Vol: 372. Issues 1–2. pp: 156 – 159. 2006.
- [40] A.R.P.J. Vijn, E.S.A.M. Lepelaars, J.B.L. Dubbeldam, M.B. van Gijzen, A.W. Heemink. Magnetic susceptibility Estimation for Magnetostatics. *IEEE Trans. on Magn.* Vol. 55. No. 3. 2019.
- [41] Y. Vuillermet, O. Chadabec, J. L. Coulomb, J. P. Bongiraud, G. Cauffet and P. Le Thiec. Scalar Potential Formulation and Inverse Problem Applied to Thin Magnetic Sheets. *IEEE Trans. on Magn.* Vol. 44. No. 6. 2008.

- [42] M. A. Zaman, P. C. Hansen, L. T. Neustock, P. Padhy and L. Hesselink. Adjoint Method for Estimating Jiles-Atherton Hysteresis Model Parameters. *Journal of Applied Physics*. No. 120. 2016.
- [43] S. E. Zirka et al. On physical aspects of Jiles-Atherton models. *Journal of Applied Physics*. Vol: 112. 2012.
- [44] J. Ziske and T. Bödrich. Magnetic Hysteresis for Modelica. *Proceedings of the 9th International Modelica Conference*. 2012.

## APPENDIX A. TABLE OF JA+R PARAMETER BOUNDARIES FOR SFLA

A set of JA+R parameter boundaries for SFLA are given in Table. 2. Recall that using such bounds reduces the computation time of to execute the SFLA and speeds up the convergence of the algorithm. The values of the boundaries should be chosen in such a way that one avoids the introduction of a bias in the solution. In this chapter, the values are based on both known values from the literature for steel alloys, as mentioned in Section 5.6.

Tabel 2: JA+R parameter boundaries for SFLA.

JA Parameter	min. value	max. value	Unit
$M_s$	$1.50 \times 10^6$	$1.80 \times 10^6$	$\text{Am}^{-1}$
$k$	0	5000	$\text{Am}^{-1}$
$a$	0	5000	$\text{Am}^{-1}$
$c$	0.05	0.5	-
$\alpha$	$1.0 \times 10^{-5}$	$1.0 \times 10^{-2}$	-

5

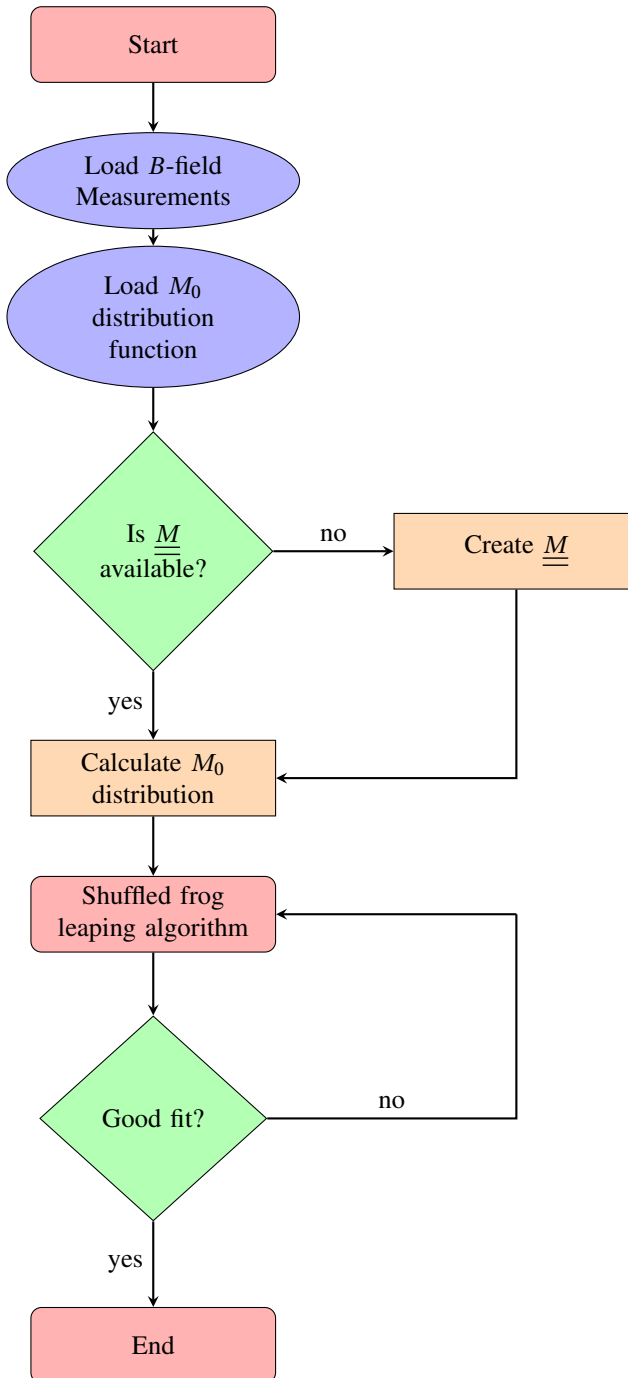
## APPENDIX B. PARAMETER ESTIMATION FLOWCHART

In this appendix, a flowchart for the proposed parameter estimation is presented. Based on the initial magnetisation distribution estimation and the shuffled frog leaping algorithm, an optimisation process is defined to find the optimal values of the parameters in the **JA+R** model. The flowchart can be found in Fig. 12.

To clarify the flowchart, note that  $\underline{\underline{M}}$  is the coefficient matrix based on the collection of higher-order Gaussian functions with unknown amplitudes. Note that the linear problem mentioned in (5.13) can be translated to a linear system of the form

$$\underline{\underline{MA}} = \mathbf{b} \quad (19)$$

from which the initial magnetisation distribution can be computed.



Figur 12: Algorithm for determination of material parameters. Firstly, measured data of the magnetic induction field  $B$  is loaded into the algorithm. Based on the initial magnetisation distribution, the sensitivity matrix  $\underline{M}$  is created and  $M_0$  is computed. Then the Shuffled frog leaping algorithm is used to find the optimal set of material parameters that fits the measured data in an optimal way.



# 6

## PREDICTION OF THE MAGNETIC STATE OF FERROMAGNETIC OBJECTS BY ASSIMILATING DATA INTO A PHYSICAL MODEL

*This chapter is based on:*

*Aad Vijn, Bart Jan Peet, Marianne Schaaphok, Eugene Lepelaars and Arnold Heemink. Prediction of the Magnetic State of Ferromagnetic Objects by Assimilating Data into a Physical Model. Submitted to: IEEE Trans. on Magn.. Manuscript under review (2021).*

### ABSTRACT

*This chapter presents a hybrid model to estimate the magnetic behaviour of a ferromagnetic structure. The mathematical-physical model has been developed using the Method of Moments combined with a hysteresis model. The mathematical model was derived by a linearisation of the hysteresis curve. The initial magnetic state of a ferromagnetic object is found through inverse computations, including regularisation techniques. The idea of dictionary regularisation is introduced to support the inverse computations with prescribed templates that reflect a priori knowledge of the typical shapes of magnetisation distributions. These templates are extracted from the Method of Moments. Data assimilation is used to update the model in time by means of measurements of the magnetic field near a ferromagnetic structure. The proposed hybrid model is implemented for a typical steel object and verified by means of numerical experiments and measurements in an experimental environment.*

## 6.1. INTRODUCTION

Estimation of the magnetic state of ferromagnetic objects is in general very difficult. This is due to the nonlinear and hysteretic behaviour of ferromagnetic material, a field that is still open to be explored scientifically. In the past century, a number of models have been developed to describe ferromagnetic behaviour. The mathematical principles of Preisach [20] and the quasi-physical model of Jiles and Atherton [12] serve as a foundation for this modeling. Also energy-based models show promising results, such as the energy-based variational model [14] based on laws of thermodynamics, the extended version [16] in which the underlying minimisation problem is analysed in more detail, and the homogenized energy model [18].

Accurate descriptions of the ferromagnetic dynamics are important in smart material systems, where ferromagnetic materials such as steel cores are used in the construction of electronic devices [18]. The performance of such devices suffer from the non-static electrostatics of their structures and in order to work properly, this has to be taken into account. Also understanding energy losses in transformers due to soft ferromagnetic cores requires a good understanding of ferromagnetic behaviour and corresponding modeling principles.

Another application is the identification of magnetic states of steel vessels in a military context. In [8–10] it is explained that identification and evaluation of magnetic signatures of naval vessels is important in order to protect these vessels against hostile threats. In particular, two threats are of interest in the case of magnetic signatures. One are modern influence mines that sense the magnetic field. Based on these measurements, a mine can decide if a potential naval vessel is nearby and can actuate to (critically) damage a naval vessel. Another threat is the risk for a submarine to be detected by means of so-called *magnetic anomaly detection* (MAD) [17]. This inverse method effectively determines the location and strength of a magnetic dipole based on measurements of the magnetic field.

In this chapter, we propose a mathematical-physical model to predict the magnetic state of a ferromagnetic object. Following from this is the hybrid model which is based on the combination of a hysteresis model to describe the behaviour of ferromagnetic material and the Method of Moments to describe the inter-coupling effects inside a large magnetised structure. This mathematical-physical model is then used to describe changes in magnetisation for varying magnetic background fields.

Data-assimilation [1, 6] is a mathematical field that combines (numerical) models with experimental observations to obtain a more accurate mathematical-physical description of the phenomenon at hand. In such methods, as in parameter estimation methods, inverse problems are typically involved. By inverse problems, it is understood that an underlying quantity is estimated by means of measurement data. Such problems are challenging from a mathematical point of view. By assimilating data, an estimate of the underlying model parameters can be obtained. Alternatively, it is used to enhance the estimation of the state of a model and thus to improve the predictive power of a model. The application of data-assimilation is well known in the field of weather forecasting and air quality models. In this chapter, data-assimilation is used in the following way. By means of near field measurements of the magnetic field, we set up a data assimilation procedure. This allows us to correct the predictions based on the physical model. It is important to note that in specific applications, a much simpler correction method can be used to obtain an improved model.

In this chapter, a much more general approach is proposed, which is based on the known underlying physics. This allows one to correct for a larger set of effects that might be absent in the numerical model by forehand.

In the prediction of the magnetic state, inverse problems are solved. In magnetostatics, such inverse problems are inherently ill-posed, which introduces extra difficulties in obtaining robust solutions. One way to resolve these issues, is the regularisation of the inverse problem. In the current chapter, a priori information about the solutions of an inverse problem is used to reduce the problem complexity. In the data-assimilation scheme, regularisation plays an important role. Examples of regularisation that are considered in this work are a smoothness operator and dictionary learning. The addition of regularisation in the assimilation scheme implies that changes in the magnetic state prediction are correct and numerically stable.

This chapter is structured as follows. In Section 6.2 the assumptions throughout this chapter are mentioned. In Section 6.3 a few preliminary notions in magnetostatics are recalled. In particular a field description of the magnetic distortion field is mentioned, that is used extensively in the derivation of the Method of Moments. The methodology behind the Method of Moments is discussed in Section 6.4. Section 6.5 defines the forward and inverse problems that are used in the derivation of the mathematical physical model and data assimilation. Also, the use of a dictionary regularisation approach is discussed, in which a set of templates are used to support the inverse problems in obtaining accurate solutions to inverse problems. In Section 6.6 the connection between the MoM and a hysteresis model is discussed. The Rayleigh model is used as a model for ferromagnetic behaviour, although this choice is not strictly necessary. In a similar way other hysteresis models can be used. Via point-wise linearisation in time, a dynamical model for temporal changes in magnetisation due to ferromagnetism follows. In Section 6.7 the data-assimilation step is added to the ferromagnetic model that is obtained in Section 6.6. The resulting model is called the hybrid model, as it incorporates both a mathematical-physical model and data-assimilation. After the methodology, a twin experiment is conducted to understand the consistency of the proposed prediction model and to analyse to what extent it is possible to describe the magnetic state sufficiently accurate. In Section 6.8 the test object and experimental setup are introduced. To verify the hybrid model, a numerical twin experiment is conducted and the results are found in Section 6.9. After this numerical analysis, the application of our hybrid model to real measurement data is discussed in Section 6.10. The chapter is concluded in Section 6.11.

## 6.2. ASSUMPTIONS

Throughout this chapter, the following assumptions hold.

- *Uniform background field* in the neighborhood of a ferromagnetic object is considered. It is assumed that the changes in the background field are relatively slow in time, ensuring that the linearised model can be used in a time-stepping numerical scheme.
- *Isotropic nonlinear behaviour*. We look at the static ferromagnetic behaviour that is described by the magnetostatic equations. The nonlinear and hysteretic behaviour is taken into account, but time-dependent behaviour such as relaxation and magnetic viscosity are neglected;

- *First-order approximation of hysteretic and nonlinear behaviour* based on the well known separation of the magnetisation into an induced part and a permanent part. The induced magnetisation is described by the location-dependent magnetic susceptibility  $\chi$ , which is assumed to change in time due to the hysteretic behaviour. Furthermore, we assume that any hysteretic behaviour is described by a (slowly) varying permanent magnetisation and small changes in the value of the magnetic susceptibility. Note that this approach remains valid in the presence of a weak applied field [13].

### 6.3. MAGNETOSTATICS

Suppose that a ferrous object is placed in a uniform magnetic background field  $\mathbf{B}_0 = \mu_0 \mathbf{H}_0$ . Let  $\Omega \subseteq \mathbb{R}^3$  represent the compact volume corresponding to the object. Assume that  $\Omega$  is constructed from ferromagnetic material that behaves in an isotropic way. The ferromagnetic material responds to the background field, inducing a magnetisation  $\mathbf{M}$  in the material. Assuming that the magnetic field  $\mathbf{H}$  is sufficiently close to  $\mathbf{H}^*$ , a linearisation is allowed to approximate the nonlinear behaviour of the ferromagnetic material. In particular, Taylor expansion around the point  $(\mathbf{H}^*, \mathbf{M}^*)$  leads to

$$\mathbf{M}(\mathbf{H}) = \mathbf{M}^* + \left. \frac{\partial \mathbf{M}}{\partial \mathbf{H}} \right|_{\mathbf{H}=\mathbf{H}^*} \bullet (\mathbf{H} - \mathbf{H}^*) + \text{h.o.t.} \quad (6.1)$$

where h.o.t. stands for the higher order terms of this expansion. From here after the magnetisation is assumed to be the sum of an induced part and a permanent part

$$\mathbf{M} = \mathbf{M}_{ind} + \mathbf{M}_{per}. \quad (6.2)$$

Note that combining (6.1) and (6.2) leads to the expressions

$$\mathbf{M}_{per} = \mathbf{M}^* - \left. \frac{\partial \mathbf{M}}{\partial \mathbf{H}} \right|_{\mathbf{H}=\mathbf{H}^*} \bullet \mathbf{H}^* \text{ and } \mathbf{M}_{ind} = \left. \frac{\partial \mathbf{M}}{\partial \mathbf{H}} \right|_{\mathbf{H}=\mathbf{H}^*} \bullet \mathbf{H}. \quad (6.3)$$

where we have used that  $\mathbf{M}_{per}$  is the magnetisation that remains in absence of the magnetic field  $\mathbf{H}$ . In general, the higher order terms are neglected and hence the traditional separation of ferromagnetism into a permanent and induced part follows [19]. In this chapter, we assume that the higher order terms in (6.1) and hysteretic behaviour are included into the permanent magnetisation part, under the assumption that these higher order terms vary slowly in time. These slow variations are required to allow the use of data assimilation to capture the hysteretic effects in the sensor data.

The constitutive relationship for isotropic linearly reacting material now follows from (6.3) and reads

$$\mathbf{M}_{ind} = \chi \mathbf{H}, \quad \left. \frac{\partial \mathbf{M}}{\partial \mathbf{H}} \right|_{\mathbf{H}=\mathbf{H}^*} := \chi I_3 \quad (6.4)$$

where  $\chi \in \mathbb{R}$  is the incremental magnetic susceptibility and  $I_3$  is the  $3 \times 3$  identity matrix. Note that the value of  $\chi$  typically depends on the centre for which the Taylor expansion is evaluated. Lastly, the value of the permanent magnetisation is assumed to be constant for a given Taylor expansion of  $\mathbf{M}(\mathbf{H})$ .

Due to the magnetisation, a perturbation in the magnetic background field arises and this is called the reduced magnetic field, denoted by  $\mathbf{H}_{red}$ . The total magnetic field  $\mathbf{H}$  and the magnetic induction field  $\mathbf{B}$  inside and outside  $\Omega$  reads

$$\begin{aligned}\mathbf{H} &:= \mathbf{H}_0 + \mathbf{H}_{red} \\ \mathbf{B} &:= \mathbf{B}_0 + \mathbf{B}_{red}.\end{aligned}\quad (6.5)$$

Note that  $\mathbf{H}_{red}$  depends on the total magnetisation  $\mathbf{M}$ , and therefore on both the permanent and induced magnetisation. In turn, this implies that in (6.3) and (6.4) the induced magnetisation in fact also depends on the permanent magnetisation. In Section 6.5.3 this implication is further discussed.

To obtain the reduced magnetic field due to a prescribed magnetisation  $\mathbf{M}$ , the magnetostatic field equations are solved:

$$\begin{cases} \nabla \times \mathbf{H} = \mathbf{0} \\ \nabla \cdot \mathbf{B} = 0 \\ \mathbf{B} = \mu_0(\mathbf{H} + \mathbf{M}) \end{cases}.\quad (6.6)$$

In these equations,  $\mathbf{B}$  denotes the magnetic induction field, and  $\mu_0 = 4\pi \cdot 10^{-7} \text{ N/A}^2$  is the magnetic permeability in vacuum. In [15] the reduced magnetic induction field  $\mathbf{B}_{red}$  is expressed in terms of the curl of the vector potential

$$\mathbf{B}_{red}(\mathbf{r}) = \nabla \times \left( \frac{\mu_0}{4\pi} \iiint_{\Omega} \frac{\mathbf{M}(\mathbf{r}') \times (\mathbf{r} - \mathbf{r}')}{\|\mathbf{r} - \mathbf{r}'\|^3} d\mathbf{r}' \right).\quad (6.7)$$

## 6.4. METHOD OF MOMENTS

In this section, the methodology behind the prediction model is discussed. Most of the equations are already derived in [15], but here we extend the proposed Method of Moments to include permanent magnetisation. To make this chapter self-contained, the relevant equations are briefly reviewed. After both the forward and inverse problem are defined, a filter algorithm is described for data-assimilation and correction of the magnetic state. This filter also includes a regularisation technique to avoid local updates in the magnetic state prediction, as such corrections are unphysical. A smoothness operator ensures that the updates are done globally.

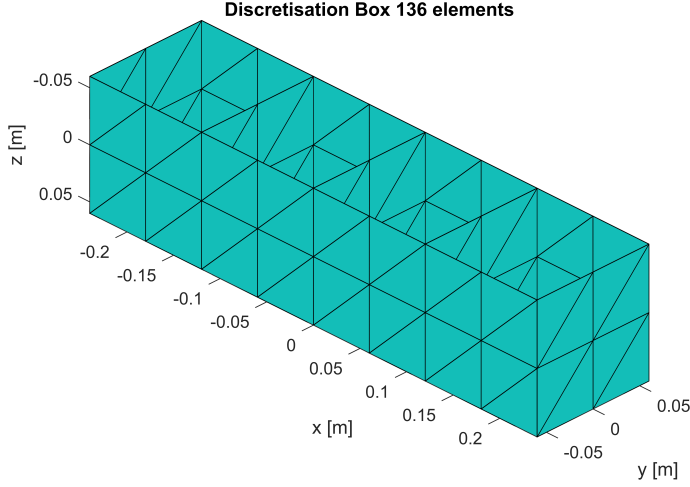
Following [15], Morandi et al. proposed a Method of Moments based on the discretisation of a magnetic object in triangular prisms. As an example in Fig. 6.1 a discretisation of an object is depicted.

It is assumed that the magnetisation (both permanent and induced) is uniform within each triangular prism  $e_k$ , i.e.,

$$\mathbf{M}(\mathbf{r})_{e_k} = \mathbf{M}_k, \quad \text{for } \mathbf{r} \in e_k.\quad (6.8)$$

Furthermore, the magnetic susceptibility is assumed uniform on each element. Equivalent to the constitutive relation mentioned in (6.4),

$$\mathbf{M}_{ind} = f \left( \frac{\mathbf{B}}{\mu_0} - \mathbf{M}_{per} \right), \quad f := \frac{\chi}{1 + \chi}\quad (6.9)$$



Figuur 6.1: A mesh of the test object in triangular prisms. Dimensions are in meters. The thickness of the elements are not shown.

6

for a prescribed permanent magnetisation  $\mathbf{M}_{per}$ . Equation (6.9) is used to derive the Method of Moments where  $\mathbf{B}$  is the internal magnetic induction field. The scalar value of  $\hat{f}$  reflects the assumptions on isotropic material and depends on the location in  $\Omega$ . Using the discretisation, the magnetic induction field at any point  $\mathbf{r} \in \Omega$  inside the object is approximated by

$$\mathbf{B}(\mathbf{r}) = \mathbf{B}_0 + \mathbf{B}_{red} = \mathbf{B}_0 + \mathbf{B}_{ind} + \mathbf{B}_{per} \quad (6.10)$$

$$= \mathbf{B}_0 + \sum_{k=1}^{N_e} [C(\mathbf{r})]_k (\mathbf{M}_{ind})_k + (\mathbf{M}_{per})_k \quad (6.11)$$

where  $\mathbf{B}_{ind}$  and  $\mathbf{B}_{per}$  are the magnetic induction field produced by the the induced and permanent magnetisation respectively. Furthermore,  $N_e$  is the number of elements and  $[C(\mathbf{r})]_k$  is a  $3 \times 3$  matrix defined by

$$[C(\mathbf{r})]_k = \sum_{i=1}^3 \left[ \nabla \times \left( \frac{\mu_0}{4\pi} \iiint_{e_k} \frac{\mathbf{u}_i \times (\mathbf{r} - \mathbf{r}')}{\|\mathbf{r} - \mathbf{r}'\|^3} d\mathbf{r}' \right) \right] \mathbf{u}_i^T \quad (6.12)$$

where  $\mathbf{u}_i$  is the unit vector along the  $i$ -th direction. Further derivations for these matrices are found in [15]. Knowing all the  $3 \times 3$  matrices  $[C(\mathbf{r})]_k$ , one can assemble a  $3N_e \times 3N_e$  matrix  $C = [C(\mathbf{r}_1) \ C(\mathbf{r}_2) \ \dots \ C(\mathbf{r}_{N_e})]^T$  by applying a point-matching method for which the centre of each prism is used to evaluate the matrices  $[C(\mathbf{r})]_k$ . Note that matrix  $C$  maps a magnetisation distribution to the corresponding internal magnetic induction field. A similar reasoning is applied to  $\hat{f}$ , which leads to a  $3N_e \times 3N_e$  diagonal matrix  $f$  with the magnetic susceptibility values on the diagonal for each element.

Using the assembled matrix  $C$  the numerical approximation of the magnetic induction field  $\mathbf{B}$  in (6.11) can be written as

$$\mathbf{B}(\mathbf{r}) = \mathbf{B}_0 + C\mathbf{M}_{ind} + C\mathbf{M}_{per} \quad (6.13)$$

where the quantities  $\mathbf{M}_{ind}, \mathbf{M}_{per} \in \mathbb{R}^{3N_e}$  are now the numerical vectors for the induced and permanent magnetisation. In the remainder of this chapter, we will refer to these numerical vectors for the induced and the permanent magnetisation respectively, on a fixed partitioning of the object  $\Omega$ . Combining the assembled matrix  $C$  and the expression for the magnetic induction field  $\mathbf{B}$ , the following linear equation can be found for the magnetisation after substitution into (6.9):

$$A(\chi)\mathbf{M}_{ind} = \left(\frac{f}{\mu_0}\right)\mathbf{B}_0 + \left(\frac{f}{\mu_0}\right)C\mathbf{M}_{per} - f\mathbf{M}_{per}, \quad (6.14)$$

where  $A(\chi)$  is a  $3N_e \times 3N_e$  matrix that depends on the magnetic susceptibility and is given by

$$A(\chi) = I - \left(\frac{f}{\mu_0}\right)C. \quad (6.15)$$

Therefore, the solution to system (6.14) is given by

$$\mathbf{M}_{ind} = A(\chi)^{-1} \left( \left(\frac{f}{\mu_0}\right)\mathbf{B}_0 + \left(\frac{f}{\mu_0}\right)C\mathbf{M}_{per} - f\mathbf{M}_{per} \right). \quad (6.16)$$

Note that the induced magnetisation depends of the permanent magnetisation. This observation is reflected by the MoM in (6.16).

## 6.5. STATIC FORWARD AND INVERSE PROBLEM

### 6.5.1. STATIC FORWARD PROBLEM

Let  $\mathcal{V} = \{\mathbf{s}_1, \mathbf{s}_2, \dots, \mathbf{s}_{N_s}\}$  be a collection of measurement locations of the magnetic field  $\mathbf{B}$  outside  $\Omega$ , where  $N_s$  is the number of sensors. Assume that the magnetic background field  $\mathbf{B}_0$  is known beforehand. The static forward problem amounts to computing the magnetic induction field  $\mathbf{B}$  at the given collection of measurement locations.

Given some magnetisation distribution  $\mathbf{M}$  the magnetic field at the measurement locations  $\mathcal{V}$  can be computed using (6.7) and (6.5). If  $\mathbf{B}_0 \in \mathbb{R}^{3N_s}$  contains the values of the magnetic background induction field at the sensor locations, then the magnetic induction field  $\mathbf{B}_c$  is computed through

$$\mathbf{B}_c[\mathbf{M}] = \mathbf{B}_0 + C_1\mathbf{M}, \quad C_1 \in \mathbb{R}^{3N_s \times 3N_e}, \quad (6.17)$$

where  $C_1 = [C(\mathbf{s}_1) \ C(\mathbf{s}_2) \ \dots \ C(\mathbf{s}_{N_s})]^T$  is the field matrix in locations  $\mathcal{V}$  and  $\mathbf{M} = \mathbf{M}_{ind} + \mathbf{M}_{per}$  is the numerical vector for the total magnetisation.

### 6.5.2. STATIC INVERSE PROBLEM

The static discrete inverse problem amounts to finding the optimal magnetisation  $\mathbf{M}$  such that there is an agreement between a measured magnetic induction field  $\mathbf{B}_m \in \mathbb{R}^{3N_s}$  and the magnetic field  $\mathbf{B}_c[\mathbf{M}]$  computed using (6.17). If one defines the residual

$$\mathbf{Res} = \mathbf{B}_m - \mathbf{B}_c[\mathbf{M}], \quad (6.18)$$

then the solution to the discrete inverse problem is found by solving the following Tikhonov minimisation problem

$$\hat{\mathbf{M}} = \underset{\mathbf{M} \in \mathbb{R}^{3N_e}}{\operatorname{argmin}} \mathbf{Res}^T \mathbf{Res} + \lambda^2 \|\mathbf{R}\mathbf{M}\|_2^2, \quad (6.19)$$

where  $R$  is a regularisation operator [21] and  $\lambda$  is the corresponding regularisation parameter. The regularisation operator typically enforces certain conditions or properties on the solution, depending on the choice of  $R$ . Well known examples of  $R$  are either the identity matrix (minimising the length of the solution-vector) or a smoothing operator (the first-order derivative or Laplacian operator), enforcing certain smoothness properties upon the solutions. The regularisation parameter is used to put more or less emphasis on the regularisation term. If  $\lambda$  is chosen small, the optimisation problem primarily minimises the residual, while if  $\lambda$  is large, the regularisation term is minimised, enforcing the regularised solution to stay close to the null-space of  $R$ .

If we only consider reduced magnetic fields, then the solution to the above minimisation problem is found in an equivalent way by solving the normal equations

$$(C_1^T C_1 + \lambda^2 R^T R) \mathbf{M} = C_1^T \mathbf{B}_m \quad (6.20)$$

using a singular value decomposition [21] or by applying a Krylov iterative method such as CGLS on (6.19). The optimal value for  $\lambda$  is found using the  $L$ -curve criterion [7].

### 6.5.3. PERMANENT MAGNETISATION ESTIMATION

To determine the initial magnetic state in the hybrid model in Section 6.7, an inverse problem has to be solved for  $t = 0$ . Based on the discrete inverse problem, an inverse problem for the permanent magnetisation is derived.

Assume that at time instant  $t = 0$  a measurement of the magnetic induction field  $\mathbf{B}_m$  is available at a collection of measurement locations, as described in Section 6.5.1 in the presence of an applied field  $\mathbf{B}_0$ . We stress that, although in the absence of an applied field, the magnetisation always consists of a permanent magnetisation contribution and an induced magnetisation. The induced magnetisation is the result of the internal magnetic field caused by the permanent magnetisation.

Based on the above observation, let us write the magnetisation  $\mathbf{M}|_{t=0}$  (in the presence of an applied field) as a sum of the permanent magnetisation and the corresponding induced magnetisation, i.e.,

$$\mathbf{M}|_{t=0} = \mathbf{M}_{per} + \mathbf{M}_{ind}|\mathbf{B}_0. \quad (6.21)$$

The induced magnetisation is the solution to the MoM under the conditions of applied field and the presence of an internal magnetic field due to the permanent magnetisation. The resulting solution to the MoM is given in (6.16). Using the intermediate result

$$I + A(\chi)^{-1} \left( \left( \frac{f}{\mu_0} \right) C - \frac{\chi}{\chi + 1} I \right) = \frac{1}{\chi + 1} A(\chi)^{-1} \quad (6.22)$$

shows that the total magnetisation can be fully expressed in terms of the presence of a permanent magnetisation and an applied magnetic background field by combining (6.21) and (6.16):

$$\mathbf{M}|_{t=0} = A(\chi)^{-1} \left( (1 - f) \mathbf{M}_{per} + f \left( \frac{\mathbf{B}_0}{\mu_0} \right) \right), \quad s \equiv \frac{\chi}{\chi + 1}. \quad (6.23)$$

Note that the permanent magnetisation is easily obtained from the magnetisation if (6.23) is solved for  $\mathbf{M}_{per}$ :

$$\mathbf{M}_{per} = \frac{1}{1 - f} \left( A(\chi) \mathbf{M} - f \left( \frac{\mathbf{B}_0}{\mu_0} \right) \right). \quad (6.24)$$

The computed magnetic induction field  $\mathbf{B}_c$  at  $t = 0$  at the measurement locations is then obtained through

$$\mathbf{B}_c = K\mathbf{M}_{per} + C_1 A(\chi)^{-1} \left( \frac{f}{\mu_0} \right) \mathbf{B}_0 + \mathbf{B}_0, \quad (6.25)$$

where  $K \equiv \frac{1}{\chi+1} C_1 A(\chi)^{-1}$  and the residual is defined as

$$\mathbf{Res} = \mathbf{B}_m - \left( \mathbf{B}_0 + K\mathbf{M}_{per} + C_1 A(\chi)^{-1} \left( \frac{f}{\mu_0} \right) \mathbf{B}_0 \right). \quad (6.26)$$

#### 6.5.4. OPERATORS FOR REGULARISATION

In order to reduce the large solution space in the inverse problem, a regularisation operator is derived based on the interaction matrix mentioned in the previous section.

##### SMOOTHNESS OPERATOR

The first well known example of a regularisation operator is based on the assumption of smoothness on the solution to the inverse problem. Assuming that the solution is differentiable, we know that local variations in the solution are bounded. Then a regularisation operator  $R$  can be derived as explained in [21].

##### DICTIONARY AS A REGULARISER

Sometimes the magnetisation distribution can be represented by a linear combination of a priori basis distributions, which we will refer to as templates for the (permanent) magnetisation. In this way, a dictionary of field-shapes can work as a regulariser. In this paragraph, the principles behind this dictionary approach are illustrated using a small set of templates. In the next paragraph, the dictionary is extended using a more general approach in finding templates for  $\mathbf{M}$ . Note that this approach resembles the use of spectral decomposition in model order reduction (MOR) and sparse dictionary learning [2].

Let  $\mathbf{M}_1, \mathbf{M}_2, \mathbf{M}_3$  be three solutions to the MoM associated to uniform background fields of unit length in all three principal directions  $x, y$  and  $z$  respectively. Then one may regularise the solution space of the static inverse problem by using the distance of a solution to the subspace spanned by the three basis fields as a measure.

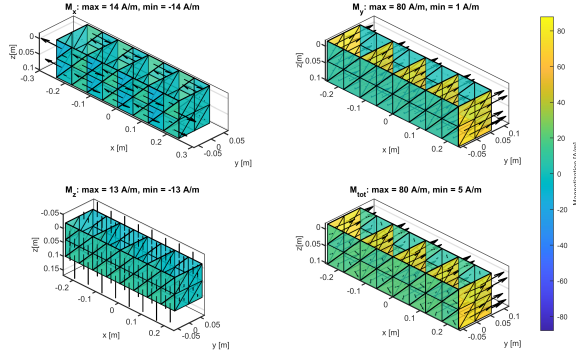
Note that when the distance of a solution to the above subspace is zero, the solution can be written as a linear combination in the basis fields. Let  $P$  be a projection matrix onto the subspace  $W = \text{sp}(\mathbf{M}_1, \mathbf{M}_2, \mathbf{M}_3) \subseteq \mathbb{R}^{3N_e}$ . Then a solution  $\mathbf{M}$  lies in the subspace  $W$  if and only if the orthogonal complement of  $\mathbf{M}$  is the zero-vector, i.e.,

$$(I - P)\mathbf{M} = \mathbf{0} \quad \Leftrightarrow \quad \mathbf{M} \in \ker(I - P). \quad (6.27)$$

Note that in the same manner as in the previous proposed regularisation operator an innovative term is introduced to allow small deviations from the templates. In mathematical terms,

$$((I - P)\mathbf{M})_i = \frac{1}{3N_e} \mathcal{I}, \quad \mathcal{I} \sim \mathcal{N}(0, \sigma^2) \quad (6.28)$$

for  $i = 1, 2, \dots, 3N_e$ . In the permanent estimation problem, the templates are added as a penalty term in the Tikhonov regularisation approach (6.19) with  $R = I - P$ . In Fig. 6.2 an example of the resulting templates can be found.



Figur 6.2: Example of a template for the static inverse problem, based on a MoM computation with a uniform background field in the  $y$ -direction.

MOM-BASED TEMPLATES FOR DICTIONARY REGULARISATION

To extend the dictionary mentioned in the previous paragraph, the Method of Moments can be used to obtain a basis of templates for magnetisation. In this section, it is assumed that the magnetic susceptibility does not show spatial variations, therefore the value of  $\chi$  is constant. Recall that a solution  $\mathbf{M}$  to the MoM (in the absence of a permanent magnetisation) satisfies

$$A(\chi)\mathbf{M} = \left(\frac{f}{\mu_0}\right)\mathbf{B}_0. \tag{6.29}$$

Furthermore,  $f$  is now a diagonal matrix with constant diagonal-entries. Therefore we can state that if  $\mathbf{M}$  is a solution to the MoM, then a necessary condition for  $\mathbf{M}$  is that it is an element of the column-space of the pseudo-inverse of  $A(\chi)$ :

$$\mathbf{M} \in \text{col } A(\chi)^\dagger. \tag{6.30}$$

Using the compact singular value decomposition (cSVD) of  $A(\chi)^\dagger$ , a basis of shapes for these solutions can be obtained. Note that if we write  $A(\chi)^\dagger = U\Sigma V^T$ , where  $U$  is an  $n \times r$  orthogonal matrix,  $V$  is an  $r \times n$  orthogonal matrix,  $\Sigma$  is an  $r \times r$  diagonal matrix with non-zero singular values on the diagonal-entries in decreasing order and  $r = \text{Rank}(A^\dagger(\chi))$ , then an immediate result is that

$$\text{col}(A(\chi)^\dagger) = \text{col}(U). \tag{6.31}$$

In the Method of Moments,  $n = 3N_e$  and  $A(\chi)^\dagger$  is non-singular, thus  $r = \text{Rank}(A^\dagger(\chi)) = 3N_e$ . To obtain a set of MoM-based templates, take  $l < r$ . The first  $l$  columns of  $U$  form a basis of a subspace of  $\text{col } A^\dagger$ , say  $\mathcal{F} = \{\mathbf{u}_1, \dots, \mathbf{u}_l\}$  (not to be confused with the unit vectors in (6.12)). These elements are added to the dictionary approach to regularise the (static) inverse problem. Note that these  $l$  vectors correspond to the  $l$  largest singular values of  $A^\dagger$ . To use the projection-approach as mentioned above, it is assumed that the size of the dictionary does not exceed the dimensions of the solution space; otherwise the projection  $I-P$  does not exist. To illustrate this template approach a template example is shown in Fig. 6.2. Note that the above-mentioned cSVD depends on the value of  $\chi$ . To avoid a numerical

burden, the limit  $\chi \rightarrow \infty$  is can be considered to obtain a cSVD independent of the value of  $\chi$ . Note that in this limit (6.29) simplifies to

$$A\mathbf{M} = \frac{1}{\mu_0}\mathbf{B}_0, \quad A := I - \frac{1}{\mu_0}C. \quad (6.32)$$

### 6.5.5. DICTIONARY REGULARISATION AS A PRECONDITIONER

The dictionary regularisation, as introduced in the previous subsections, can be seen as a preconditioner for the static inverse problem described in Section 6.5.2.

Let  $\mathcal{T}$  be a collection of linearly independent templates, as defined in the previous section. The set  $\mathcal{T}$  forms a basis of a subspace of  $\mathbb{R}^{3N_e}$ . We augment this basis with a basis  $\mathcal{T}'$  of choice for the orthogonal complement  $\text{col}\mathcal{T}$ . Then  $\mathcal{T} \cup \mathcal{T}'$  is a basis for the whole space  $\mathbb{R}^{3N_e}$ . Now form the  $3N_e \times 3N_e$  matrix  $Q = [Q_1 \ Q_2]$  for which the columns of  $Q_1$  and  $Q_2$  consist of the basis vectors from  $\mathcal{T}$  respectively  $\mathcal{T}'$ . Note that per construction the matrix  $Q$  is non-singular.

Recall that the main idea behind dictionary regularisation is that in the static inverse problem, one seeks solutions that (approximately) are a linear combination of prescribed templates. This idea can be cast into a preconditioner in the following way. One can write a solution  $\mathbf{M}$  for the static inverse problem as described in Section 6.5.2 as

$$\mathbf{M} = \sum_{j=1}^{|\mathcal{T}|} c_j \mathbf{t}_j + \sum_{j=|\mathcal{T}|+1}^{3N_e} c_j \mathbf{t}'_{j-|\mathcal{T}|} \quad (6.33)$$

where  $|X|$  stands for the number of elements in the set  $X$ ,  $\mathcal{T} = \{\mathbf{t}_1, \mathbf{t}_2, \dots, \mathbf{t}_{|\mathcal{T}|}\}$ ,  $\mathcal{T}' = \{\mathbf{t}'_1, \mathbf{t}'_2, \dots, \mathbf{t}'_{|\mathcal{T}'|}\}$  and the two bases satisfy  $|\mathcal{T}| + |\mathcal{T}'| = 3N_e$ . Using the matrix  $Q$  equation (6.33) can be compactly written as

$$\mathbf{M} = [Q_1 \ Q_2] \begin{bmatrix} \mathbf{c}_1 \\ \mathbf{c}_2 \end{bmatrix}, \quad \text{for some } \mathbf{c}_1 \in \mathbb{R}^{|\mathcal{T}|}, \mathbf{c}_2 \in \mathbb{R}^{|\mathcal{T}'|}. \quad (6.34)$$

Hence, matrix  $Q$  can be seen as a preconditioner for the static inverse problem. Therefore, if we rewrite the static inverse problem with the use of (6.34), we find the following inverse problem

$$\mathbf{M} = Q\hat{\mathbf{c}}, \quad \hat{\mathbf{c}} = \underset{\mathbf{c} \in \mathbb{R}^{3N_e}}{\text{argmin}} \|\mathbf{B}_0 + C_1 Q\mathbf{c} - \mathbf{B}_m\|^2, \quad (6.35)$$

which is equivalent to (6.19) for  $\lambda = 0$ . In particular, if a solution is found for which the entries in  $\mathbf{c}_2$  are zero, then  $\mathbf{M}$  is a linear combination of templates. Therefore, we can introduce a penalty term in terms of the 2-norm for vector  $\mathbf{c}_2$  that regularises the solution  $\mathbf{c}$ , to obtain a solution  $\mathbf{c}_2$  with small length and thus to steer the solution towards the dictionary. Hence,

$$\mathbf{M} = Q\hat{\mathbf{c}}, \quad \hat{\mathbf{c}} = \underset{\mathbf{c} \in \mathbb{R}^{3N_e}}{\text{argmin}} \|\mathbf{B}_0 + C_1 Q\mathbf{c} - \mathbf{B}_m\|^2 + \lambda^2 \|\mathbf{R}\mathbf{c}\|_2 \quad (6.36)$$

where the regularisation operator  $R$  is given by

$$R = \begin{bmatrix} \emptyset_{|\mathcal{T}| \times |\mathcal{T}|} & \emptyset_{|\mathcal{T}| \times |\mathcal{T}'|} \\ \emptyset_{|\mathcal{T}'| \times |\mathcal{T}|} & I_{|\mathcal{T}'| \times |\mathcal{T}'|} \end{bmatrix} \quad (6.37)$$

and where  $\emptyset_{|\mathcal{T}| \times |\mathcal{T}|}$  is the  $|\mathcal{T}| \times |\mathcal{T}|$  zero matrix, and  $I_{|\mathcal{T}'| \times |\mathcal{T}'|}$  is the  $|\mathcal{T}'| \times |\mathcal{T}'|$  identity matrix.

## 6.6. HYSTERESIS MODEL AND CONNECTION TO THE METHOD OF MOMENTS

In this section the Rayleigh hysteresis model, that serves as one of the building blocks for our ferromagnetic model, is explained in detail. The model describes ferromagnetic behaviour on a material level. Therefore, the connection with the Method of Moments is made to describe how magnetisation changes in a ferromagnetic macroscopic structure. We require the Method of Moments to compute the internal magnetic fields of the ferromagnetic object, to be able to use the hysteresis model in a consistent way. As only isotropic material is considered, it is sufficient to use the scalar version of the hysteresis model.

### 6.6.1. RAYLEIGH'S HYSTERESIS MODEL

Rayleigh's hysteresis model [13, 18] approximates the nonlinear behaviour of ferromagnetic materials in weak applied fields. For higher field strengths of the applied field the model is not applicable and a different more general model such as the Jiles-Atherton model or the energy-variational model is required for correct modeling of the hysteresis effects. However, Rayleigh's model gives a fairly simple way to model the hysteresis effects by approximating the minor loop branches by quadratic functions.

The initial magnetisation curve of ferromagnetic material is given by

$$M(H) = (\mu_i - 1)H + \alpha_R H^2 \quad (H > 0) \quad (6.38)$$

and

$$M(H) = (\mu_i - 1)H - \alpha_R H^2 \quad (H < 0), \quad (6.39)$$

where  $\mu_i$  is called the *initial relative permeability* and  $\alpha_R$  is called the Rayleigh constant,  $M$  and  $H$  are the magnetisation and internal magnetic field respectively. Both values of the parameters of the Rayleigh model can be found experimentally by determining the initial magnetisation curve by means of measurements. The minor loops within the hysteresis curve are based on approximation by quadratic functions. More specifically, the Rayleigh model introduces a dependence on the **modulus** of the field value  $H_m$  at the turning point of such branches.

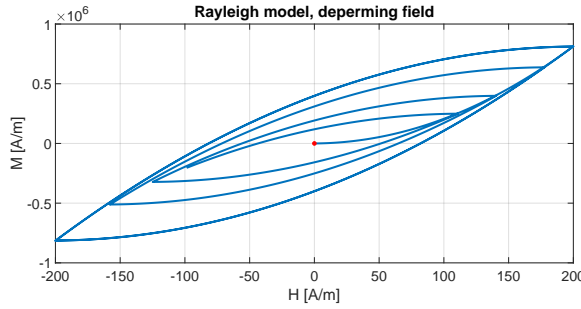
The above considerations lead to the following set of equations that describe the increasing and decreasing branches for higher-order reversal curves. For any *increasing branch* ( $H \nearrow H_m$ ) where the field strength increases we have

$$M(H) = \left[ (\mu_i - 1 + \alpha_R H_m)H - \frac{\alpha_R}{2} (H_m^2 - H^2) \right] \quad (6.40)$$

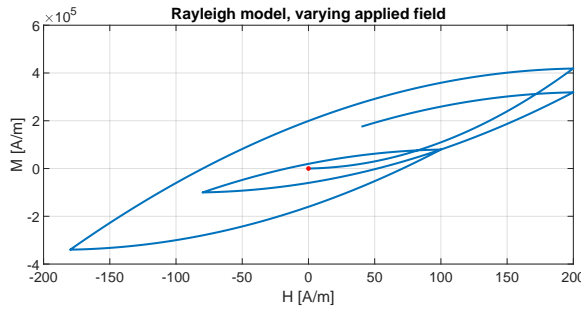
and for *decreasing branches* ( $H_m \searrow H$ ) where the field strength decreases we find that

$$M(H) = \left[ (\mu_i - 1 + \alpha_R H_m)H + \frac{\alpha_R}{2} (H_m^2 - H^2) \right]. \quad (6.41)$$

Whenever the time derivative of the magnetic field changes sign, the hysteresis follows a new increasing or decreasing branch that is defined by the last field turning point  $H_m = H_{last}$ . In Fig. 6.3 and Fig. 6.4 two realisations of the Rayleigh model are shown.



Figur 6.3: Example of a deperming signal using the Rayleigh hysteresis model. Here, the material parameters are  $\mu_i = 100$  and  $\alpha_R = 100 \text{ m/A}$ , starting at a demagnetised state. The hysteresis curve is the result of a magnetic deperm signal for the applied background field  $H$ . This signal is piece-wise linear with turning points  $H_m = [0, 200, -200, 200, -200, 178, -158, 140, -125, 111, -99]$ .



Figur 6.4: Example of a hysteresis curve in the presence of a varying applied field. Here, the materials parameters are  $\mu_i = 100$  and  $\alpha_R = 100 \text{ m/A}$ , starting at a demagnetised state. The applied field is piece-wise linear with turning points  $H_m = [0, 200, -180, 100, -80, 200, 40]$ . Observe that the symmetrical properties for increasing and decreasing branches is no longer present, but the erasure of magnetic memory is still visible.

Along the increasing and decreasing branches, we may compute the incremental magnetic susceptibility  $\chi$ . It follows that

$$\chi = \begin{cases} (\mu_i - 1 + \alpha_R H_m) - \alpha_R H & (H_m \nearrow H) \\ (\mu_i - 1 + \alpha_R H_m) + \alpha_R H & (H \nearrow H_m) \end{cases} \quad (6.42)$$

Note the change of signs in the above expressions for increasing and decreasing branches. Also, if  $\frac{dH}{dt}$  changes sign, then the incremental magnetic susceptibility makes a discontinuous jump in the model, which may lead to gaps in the minor branches. This behaviour is unfavourable. Fortunately, if one casts the above direct expressions for the parabolic curves into the scheme

$$M_{n+1} = M_n + \left. \frac{\partial M}{\partial H} \right|_{H=H_n} dH \quad (6.43)$$

for which the resulting hysteretic solutions are continuous.

### 6.6.2. MATHEMATICAL MODEL FOR TEMPORAL BEHAVIOUR OF A FERROMAGNETIC OBJECT

In this section, the Method of Moments is combined with the Rayleigh hysteresis model to obtain a framework in which the magnetic state of a ferromagnetic object is described. The idea is to alternately 1) linearise the hysteresis model around the current magnetic state ( $\mathbf{H}, \mathbf{M}$ ) of a ferromagnetic object, and 2) use the Method of Moments to compute the next point in the hysteresis model due to a change in the applied magnetic field. If one assumes that variations in the background field are small, then such a linearisation in the second step is allowed to compute the next magnetic state. This implies that variations in the magnetic state due to a time-varying background field can be tracked in the hysteresis model, which is necessary for our mathematical-physical model. In the remainder of this chapter the combination of (1) and (2) is called a *Rayleigh time step*.

## 6.7. HYBRID MODEL BASED ON DATA ASSIMILATION

In this section, the hybrid model is defined. The model consists of an initial state computation, in which an estimation of the initial permanent magnetisation is determined, and an online algorithm that describes the evolution of the magnetisation for a varying background field signal by means of Rayleigh time stepping. In this online algorithm the magnetisation is corrected during the data-assimilation step.

Note that in Section 6.5.3 the permanent magnetisation is estimated on the basis of the a priori known distribution for the magnetic susceptibility  $\chi$ . In practical applications, one should also estimate this distribution. This estimation is omitted in this chapter, and the authors refer to [21] for a method to obtain a magnetic susceptibility distribution.

A pseudo-code of the resulting hybrid model in this section is found in Appendix 6.11.

### 6.7.1. INITIAL MAGNETIC STATE

In the initial magnetic state computation, the inverse problem in Section 6.5.3 is solved. In this step, the dictionary regularisation approach is used to obtain a reliable permanent magnetisation field. Via an L-curve criterion, the optimal regularisation parameter is determined.

### 6.7.2. DATA ASSIMILATION

The data assimilation step in the hybrid model (see Section 6.7.3) is based on updating the value of the magnetisation through describing the change of permanent magnetisation. Recall that we assume that during a on a small time-scale the magnetic susceptibility distribution is fixed, but permanent magnetisation is not and varies slowly. This implies that the induced magnetisation is fully determined if one knows the values of the magnetic susceptibility, the current value of the permanent magnetisation and applied magnetic field. The value of the magnetic susceptibility and the permanent magnetisation follow from the linearisation in the Rayleigh hysteresis curve. Therefore it is assumed that discrepancies between estimation of the magnetic state and the true (hidden) magnetic state correspond to variations in the permanent magnetisation that are not taken into account in the Rayleigh hysteresis model.

The update step is based on a filtering step using near field measurements of the magne-

tic induction field. Assume that at time  $t = n + 1$  an estimate of the magnetic state is known given the information at time  $t = n$ , i.e.,  $\mathbf{M}(n + 1|n)$  is given.

Now suppose that we have a collection of measurements at locations  $\mathcal{V}$ . Note that  $\mathbf{B}_m$  is of the form

$$\mathbf{B}_m(n + 1) = \mathbf{B}_0(n + 1) + \mathbf{B}_{red}(n + 1) \quad (6.44)$$

where  $\mathbf{B}_0(n + 1)$  is the applied magnetic field at time instance  $n + 1$ . Based on the prediction  $\mathbf{M}(n + 1|n)$  we compute the residual magnetic induction field at the measurements using (6.17)

$$\mathbf{Res}(n + 1) = \mathbf{B}_m(n + 1) - \left( \mathbf{B}_0(n + 1) + \mathbf{B}_{red}[\mathbf{M}(n + 1|n)] \right) \quad (6.45)$$

By assumption, the above residual magnetic induction field corresponds to a variation in the permanent magnetic field  $\Delta\mathbf{M}_{per}$ , and to find this variation we solve the equivalent discrete inverse problem for obtaining the permanent magnetisation as described in (6.19):

$$\widehat{\Delta\mathbf{M}}_{per} = \underset{\Delta\mathbf{M} \in \mathbb{R}^{3N_e}}{\operatorname{argmin}} \left\| C_1 \Delta\mathbf{M} - \mathbf{B}_{res} \right\|_2^2 + \lambda^2 \left\| R \Delta\mathbf{M} \right\|_2^2 \quad (6.46)$$

where  $C_1$  is the field matrix at measurement locations  $\mathcal{V}_2$  and  $R$  is either the smoothing or the template operator. It is important to note that the regularisation is necessary to ensure that the update  $\Delta\mathbf{M}$  is not locally, but a correct update along the whole magnetisation vector. This is because the inverse problem is under-determined, hence extra information must be added to obtain a robust solution.

### 6.7.3. MAGNETIC STATE UPDATE

The magnetic state update step in the hybrid model is defined in terms of an iterative scheme. In this section, the steps to go from instant  $t = n$  to instant  $t = n + 1$  are discussed. Consider that case that the initial state is already determined, i.e., the magnetisation at time  $t = 0$  is known beforehand.

At time instant  $t = n + 1$  we assume that the magnetisation  $\mathbf{M}(n) := \mathbf{M}(n|n)$  is known, that the linearisation in the hysteresis curve about the point  $(\mathbf{H}(n), \mathbf{M}(n))$  led to the magnetic susceptibility value  $\chi$  and that the background induction field  $\mathbf{B}_a(n + 1)$  is given. The magnetisation at time  $n + 1$  is approximated by means of the Method of Moments. If  $\Delta\mathbf{B}_0$  is the change in the applied magnetic induction field, then

$$\mathbf{M}(n + 1|n) = \mathbf{M}(n|n) + A(\chi)^{-1}(f\Delta\mathbf{B}_0). \quad (6.47)$$

Note that in this step, it is assumed that permanent magnetisation did not change, thus any change in magnetisation is solely in a linear manner.

The next step is to update the magnetisation by means of the data-assimilation filter, as described in Section 6.7.2. Applying this filter yields

$$\mathbf{M}(n + 1|n + 1) = \mathbf{M}(n + 1|n) + \Delta\mathbf{M}(n + 1). \quad (6.48)$$

Based on the corrected magnetisation, the corresponding internal magnetic field  $\mathbf{H} \in \mathbb{R}^{3N_e}$  at the centre of the mesh elements follows from combining the Method of Moments and (6.6):

$$\mathbf{H}(n + 1) = \mu_0^{-1} \mathbf{C} \mathbf{M}(n + 1) - \mathbf{M}(n + 1) \quad (6.49)$$



Figuur 6.5: A picture of the steel rectangular test object, without an on-board sensor system.

is computed, where  $C$  is the interaction matrix defined in (6.12). The pair  $P = (\mathbf{H}(n + 1), \mathbf{M}(n + 1))$  is used to obtain a new linearisation in the hysteresis curve about the point  $P$ , as a starting point for the next time step.

## 6.8. TEST OBJECT

For numerical and practical examples, a rectangular test object is used consisting of four attached open cubes with sides of 120 mm without a top-plate. The test object is constructed from 0.5 mm thick steel plates, see Fig. 6.5. Inside 20 sensors are placed, one at the centre of each face and another 14 sensors are placed on the outside of the test object. These 34 sensors are considered as the on-board sensors for the purpose of the data-driven corrections. In Fig. 6.7 the on-board sensor locations are depicted.

The test object is placed inside a coil structure that can change the local magnetic field in all three directions. Inside the cage the background fields can take values of the form

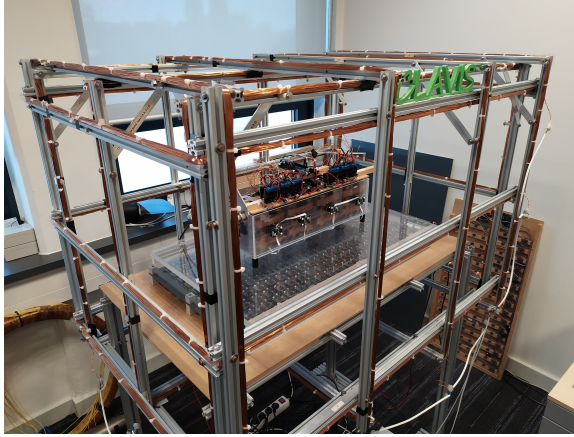
$$\left\{ \mathbf{B}_0 \in \mathbb{R}^3 : |(\mathbf{B}_0)_i| \leq 400 \mu\text{T for } i = x, y, z \right\}. \quad (6.50)$$

A sensor array consisting of 200 sensors is placed 56 mm below the object for validations. To measure the magnetic field, RM3100 Geomagnetic sensors are used. In Fig. 6.6 the experimental setup is shown.

The object is discretised using a structured mesh with equally sized triangles, see Fig. 6.1. For the experiments a mesh consisting of 136 elements is used, giving a good trade off between accuracy and computational time. An important observation is that for this choice of a mesh for the steel object, and the number of sensors in the sensor array, the static inverse problem is over-determined. Therefore, one should expect that the resulting solutions to the static inverse problem are robust.

## 6.9. NUMERICAL TWIN EXPERIMENT

To understand if a proposed model has predictive power, testing it on (experimental) data is necessary. However, in many applications, a true state is often not measurable directly. This is in particular the case when inverse problems are involved. In such cases, it is important to run numerical simulations to analyse the model's properties. A twin experiment uses the forward model to simulate a data set, by means of a prescribed true state. Then,



Figuur 6.6: The coil setup, sensor array and sensors close to the steel object. Inside and outside the steel object, magnetometers are placed at approximately 5 mm away from the faces of the object. The sensor array is placed at a distance of 56 mm beneath the steel object.

the simulated data is contaminated with noise to create a challenging data set. The same forward model is then applied on this noisy data with the aim to reproduce the underlying true state, while taking into account the noise level in the analysis of the performance.

In this section, a twin experiment is conducted to understand the consistency of the proposed hybrid model. The goal is to show that the data-assimilation is able to retrieve a good description of the magnetic state, in the case that the model initialisation differs from the true state. A consistent model is able to recover the prescribed magnetic state of the object up to a certain accuracy, depending on signal-to-noise ratio in the data.

In this twin experiment the hybrid model is applied to the rectangular test object, found in Fig. 6.5. A set of simulated data is created by running the hybrid model for a given applied magnetic field together with a prescribed initial permanent magnetisation. In this Twin experiment, the permanent magnetisation is the result of solving an inverse problem based on a real measurement of the test object inside our experimental environment. With the same hybrid model we try to estimate the magnetisation variations in time from noisy data.

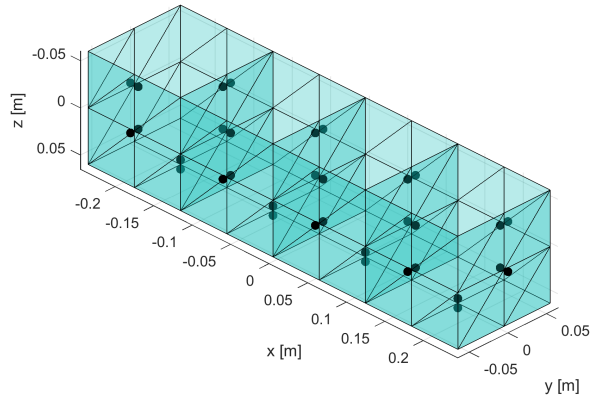
### 6.9.1. COMPUTATION OF THE SIMULATED DATA SET

In order to obtain a realistic set of simulated data, one measurement of the steel object is used. This measurement is assumed to correspond to the initial magnetic state of the object. In Fig. 6.8 the measurement of the magnetic induction field of the steel object is found.

The following values for the Rayleigh model are chosen:

$$\mu_i = 200, \quad \text{and} \quad \alpha_r = 2. \quad (6.51)$$

Note that these values are reasonable for ferromagnetic materials, in the case that hysteresis is relatively small. Based on the magnetic susceptibility, the initial permanent magnetisation is obtained via solving the corresponding inverse problem.



Figuur 6.7: The placement of the on-board sensors with respect to the test object.

Next, a varying magnetic background field  $\mathbf{B}_0$  is defined to compute how the magnetic state of the object varies in the scenario. In this computation, the magnetic model (i.e., the hybrid model without the assimilation step) is used to find the changes in the magnetic state.

In Fig. 6.9 this background field is shown. It consists of three double loops in principal directions, followed by figures-of-eight in the  $x - y$ ,  $y - z$  and  $x - z$  plane.

In each time step, the resulting magnetic induction field at the sensor array and on-board sensor locations are computed and stored for the given value of the applied magnetic field.

The magnetisation and the magnetic induction fields at the sensor locations are calculated using the hybrid model. Next the data set is contaminated with Gaussian white noise with standard deviation  $\sigma = 2 \cdot 10^{-6}$  T:

$$\mathbf{B}_m = \mathbf{B}_c + \mathbf{e}, \quad \mathbf{e} \sim \mathcal{N}(0, \sigma^2 I_{3N_s \times 3N_s}) \quad (6.52)$$

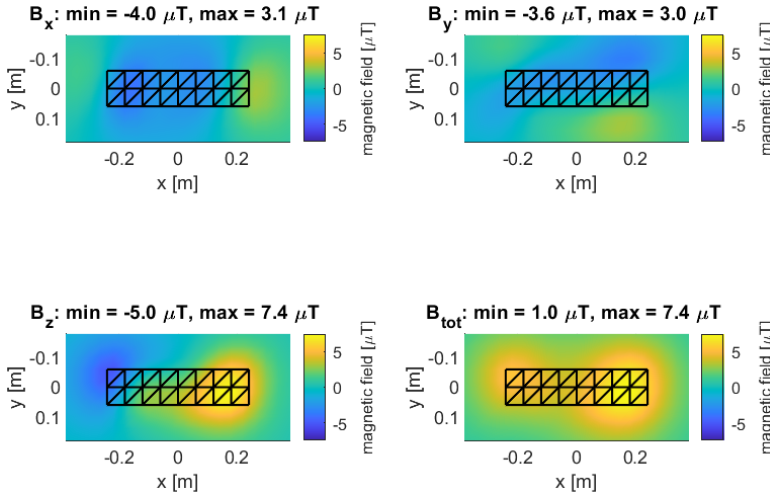
for both the sensor array and the on-board sensor measurements. This results in variations of  $\pm 6 \mu\text{T}$  per component. Note that this is a fairly large noise level. In practice magnetometers have a much lower noise level. The resulting simulated data set is used in our numerical twin experiment.

### 6.9.2. RESULTS OF TWIN EXPERIMENT

With the set of simulated data from the previous section, the numerical twin experiment can now be conducted. The idea is the following: We start with the initialisation of the hysteresis model. We guess that

$$\mu'_i = 100, \quad \text{and} \quad \alpha'_R = 1. \quad (6.53)$$

Note that the guess is quite far away from the true values. This means that our numerical model (without data-assimilation) differs from the true state and thus a significant mismatch is to be expected. Therefore it is the task of the data-assimilation scheme to correct the model based on on-board measurements.



Figur 6.8: Magnetic induction field measured at the sensor array. This field is used to obtain the initial magnetic state of the steel object to generate a realistic simulated data set.

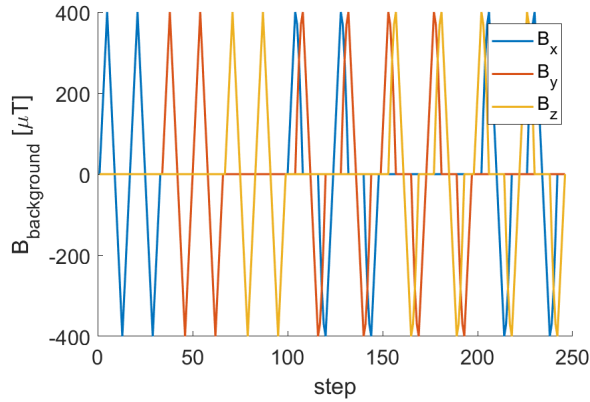
Besides choosing values for the material parameters, the initial magnetic state is estimated by applying the static inverse problem defined in Section 6.5.3 to the measurement (for all sensors) showed in Fig. 6.8. The application of Template regularisation with  $\lambda = 5 \times 10^{-10}$  is used to obtain a robust solution. The templates are derived for  $\chi = 100$  and the first three are used in our regularisation operator. If one compares Figures 6.8 and 6.11, then it is observed that there is a good agreement between the ground truth and the estimated initial magnetic induction field.

Next, the performance of the hybrid model is tested on the applied magnetic field signal. During the assimilation step, standard Tikhonov regularisation is used to obtain a smooth magnetisation correction with  $\lambda = 5 \times 10^{-10}$ . It is observed that the value of  $\lambda$  influences the resulting performance of the assimilation scheme. If the value of  $\lambda$  is too high, then in Fig. 6.12 the magnetic induction field corresponding to the ground truth, the uncorrected numerical model and hybrid model are shown for  $t = 1, 2, \dots, 150$ . Observe that our assimilation scheme often corrects the numerical model in such a way that the magnetic induction field coincides with the true state.

To evaluate the performance of the hybrid model, the Root Mean-Squared Error (RMSE) defined by

$$RMSE(X) = \sqrt{\frac{1}{N_t N_X} \sum_{i=1}^{N_t} \sum_{j=1}^{N_X} (X_{ij}^{est} - X_{ij}^{truth})^2} \quad (6.54)$$

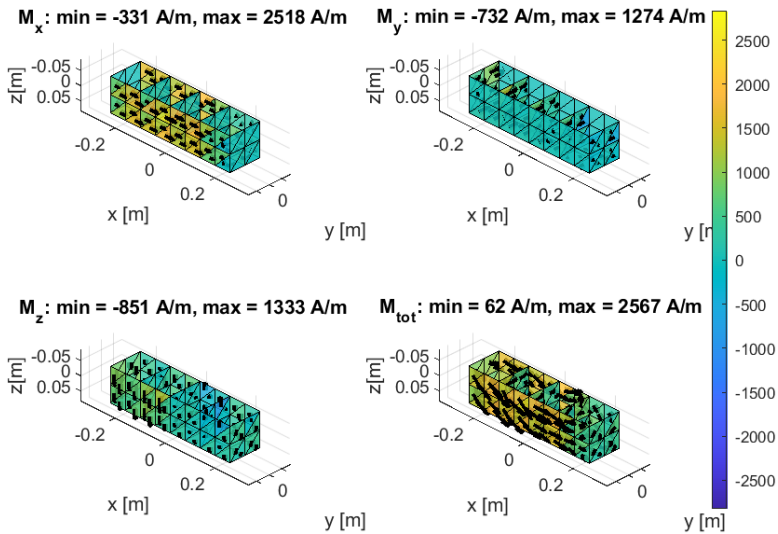
is used to check if the method is consistently able to recover the ground truth. In this chapter,  $X$  stands for either the three magnetisation components of  $\mathbf{M}$  or the three magnetic induction field components of  $\mathbf{B}$ , measured at the sensor array. Here  $N_X = 136$  (the number of mesh elements) if the RMSE is evaluated for the magnetisation and  $N_X = 200$  (the number of sensor locations) if it is evaluated at the sensor array. The number of measurements along the scenario is  $N_t = 250$ .



Figur 6.9: The applied magnetic background field that is used to generate a set of simulated data.

Looking at the values of the RMSE for the magnetic induction field in Fig. 6.13, it is observed that there is a good agreement between the estimated state and the ground truth. The RMSE at the sensor array has a maximum of  $1.44\mu\text{T}$ , which is (compared to the typical field values at the sensor array) only a few percent. Taking into account the relatively large chosen noise-level, the RMSE is surprisingly small. It is concluded that the Twin experiment is succesfull and that data-assimilation is able to correct the estimated magnetic state in a sufficient way.

6



Figur 6.10: The estimated initial magnetisation.

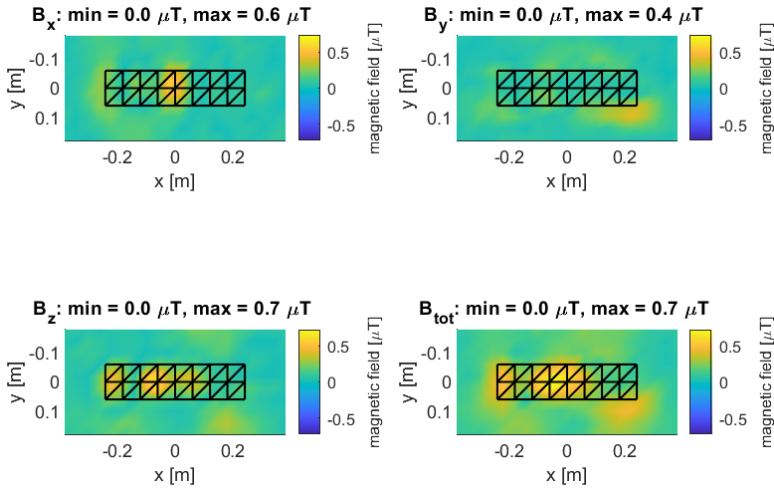


Figure 6.11: The absolute error in the initial magnetisation estimated at the sensor array. The error has a maximum of  $1\mu\text{T}$  and thus the found magnetisation is agreement with the field shown in Fig. 6.8.

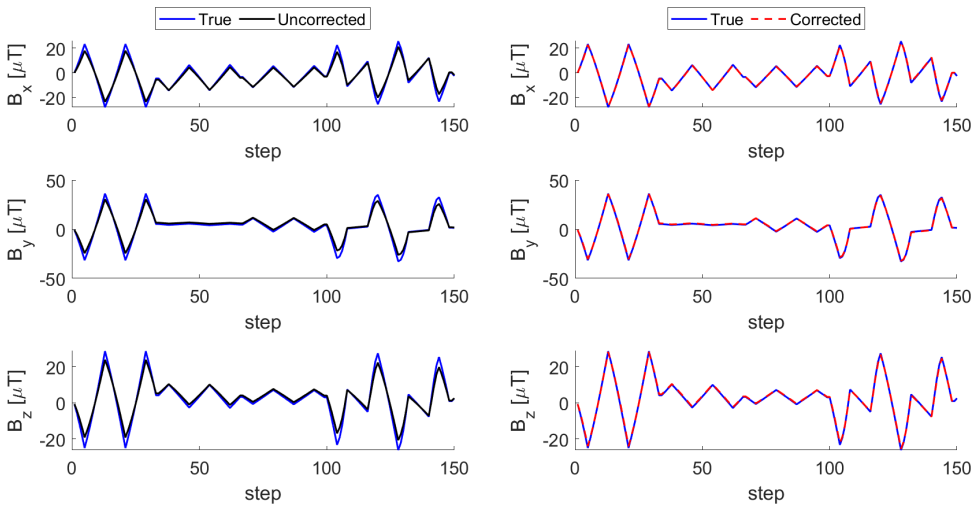


Figure 6.12: The uncorrected and corrected estimated magnetic induction field using the hybrid model compared with the ground truth magnetic induction field simulated at a sensor that is positioned at the centre of the sensor array. The uncorrected curves uses the hybrid model without the data-assimilation step.

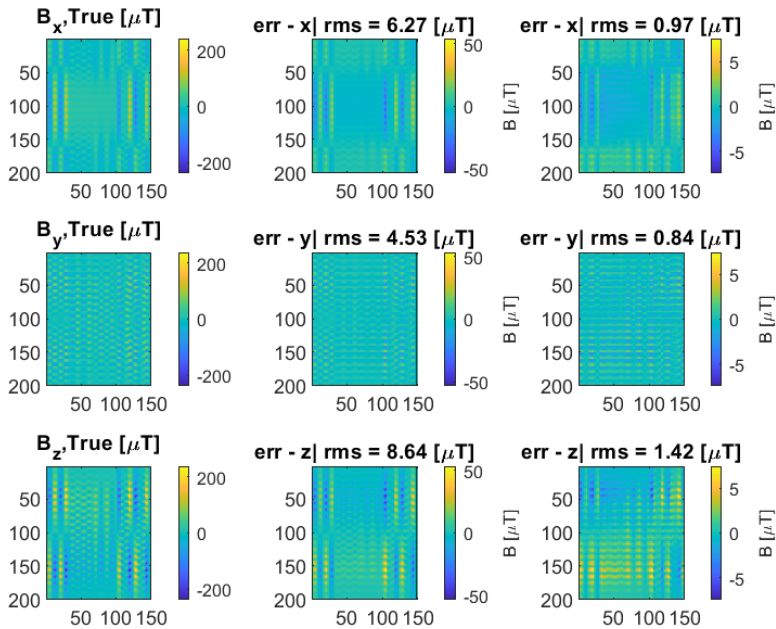


Figure 6.13: Resulting performance of both the uncorrected and corrected model. The time steps are shown along the horizontal axis, and the values of the magnetic induction field of the sensor components are shown along the vertical axis. The first column shows the magnetic induction field at the sensor array in  $\mu\text{T}$ . The second column shows the errors between the true state and the uncorrected model. The RMSE indicates that there is a relatively large discrepancy between the true state and the uncorrected model. This is expected, as the material values are far away from the true values. The third column shows the performance of the hybrid model. Note that the assimilation scheme significantly lowers the RMSE and the error drops to only a few percent of the true state.

## 6.10. APPLICATION OF THE HYBRID MODEL TO EXPERIMENTAL DATA

In the previous section it was shown that the hybrid model accurately recovers the true state during the scenario. Such a numerical twin experiment gives the user confidence that the hybrid model also works on experimental data.

In this section we validate the hybrid model on experimental data. The experimental data set is obtained using the coil construction, sensor array and the sensors in the vicinity of the steel object, as depicted in Fig. 6.6 and Fig. 6.7.

In Fig. 6.14 the applied magnetic field is shown. During this scenario, the magnetic induction field at the sensor array and at the sensors in the vicinity of the steel object are collected.

At  $t = 0$  the measurement on the sensor array is used to determine the initial magnetisation. Note that this measurement is already used in the previous section as input for a realistic initial magnetic state. Therefore, the corresponding initial state estimation is the same for the current experimental validation. The data of the sensor array for  $t > 0$  is only used for validation of the hybrid model.

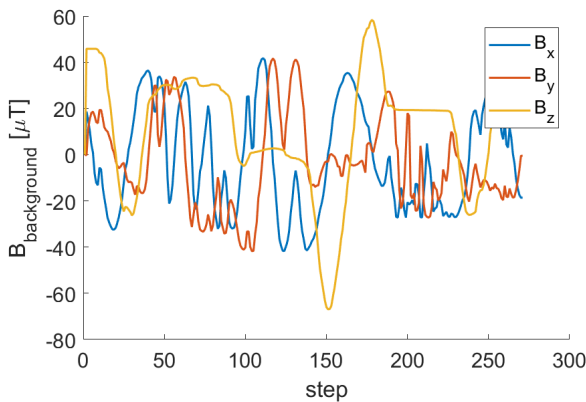


Figure 6.14: The applied magnetic background field that is used in the scenario to collect experimental data. In 270 steps the applied magnetic field is varied.

Next, the hybrid model is applied to the experimental data obtained from the scenario. The chosen hysteresis parameters are

$$\mu_i = 30, \quad \text{and} \quad \alpha_R = 0.2 \quad (6.55)$$

The data-assimilation scheme is applied to the measurements of the 34 nearby sensors, shown in Fig. 6.7. This leads to an estimation of the magnetic state  $\mathbf{M}(t)$  along the scenario. By means of the forward problem (see Section 6.5.1), the magnetic induction field at the sensor array locations is estimated and compared to the measured magnetic induction field.

For the sensor located at the centre of the sensor array, a comparison is done between the estimated field and measured field. In Fig. 6.15 the performance of the methodology is shown, in the absence of the data-assimilation scheme. Note that the performance of the

model is already good if one considers the  $y$ -component of the magnetic induction field. However, there is quite a discrepancy in the  $x$  and  $z$ -component. This implies that the current physical model does not include all effects that are measured, such as anisotropy and inhomogeneity of the material (recall that it is assumed that the material is homogeneous, which implies that the hysteresis behaviour is described by one set of parameters). Additional research, not included in this chapter, indicates that the material does behave anisotropic, for which the chosen material properties do not represent the hysteretic behaviour well in all directions in the material.

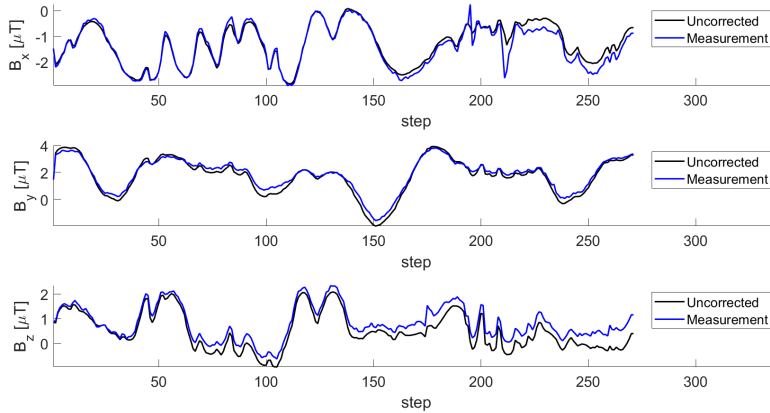
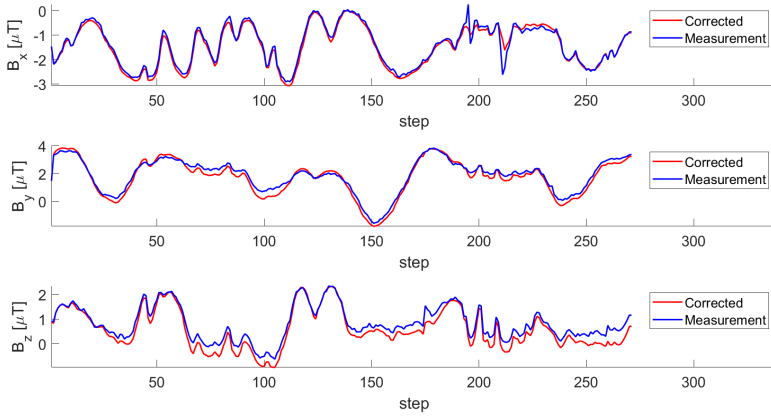


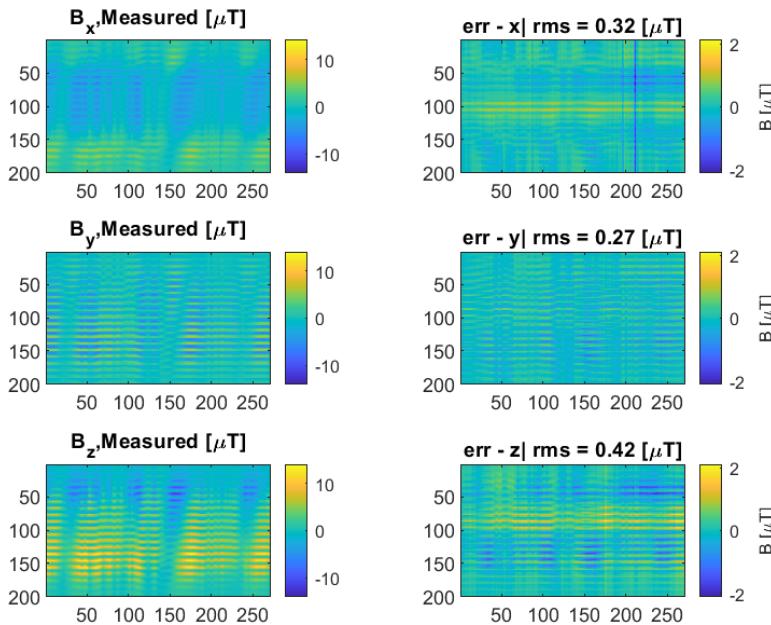
Figure 6.15: The performance of the hybrid model in the absence of a data-assimilation scheme. The reduced magnetic induction field components are shown. Note that the model is able to represent a portion of the measured data, but it has difficulties in describing the  $x$  and  $z$ -component of the magnetic induction field.

Next, the performance of the model is considered including the data-assimilation scheme. The results are shown in Fig. 6.16. Note that the data-assimilation scheme correctly picks up any discrepancy in the estimation of the magnetic state, and corrects the magnetic state such that the resulting estimated magnetic induction fields match the measured data more accurately.

Finally, we analyse the results by considering the absolute errors between the measured and the estimated magnetic induction field at the sensor array. The difference between the estimated and the measured induction field is shown in Fig. 6.17. The RMSE in the current scenario is 0.32, 0.27 and 0.42  $\mu\text{T}$  for each component respectively, resulting in errors in the order of a few percentage compared to the field strength of the measured field. This shows that the methodology is robust and able to accurately estimate the magnetic state of the steel object. In Fig. 6.18 the maximum value of the magnetic induction field at the sensor array is visualised for both the uncorrected numerical model and the hybrid model. Note that on the time interval  $[0, 180]$  both the uncorrected and the hybrid model are producing a maximum field close to the measured value. However, on the interval  $[180, 225]$  we see that the uncorrected numerical model deviates away from the measurements, while the hybrid model is capable of staying close to the measurement. This illustrates the added value of data-assimilation to the numerical model. We conclude that the validation of our hybrid model with experimental data is successful.



Figur 6.16: The performance of the hybrid model, with the data-assimilation scheme. Note that, compared to Fig. 6.15, the assimilation of data leads to a better estimation of the  $x$ -component of the magnetic induction field at the centre of the sensor array.



Figur 6.17: (left) the measured magnetic induction field during the scenario. Along the  $y$ -axis, the measurement of the field in each sensor is shown, while along the  $x$ -axis the estimation in time is shown. (right) The difference between the estimation and the measured magnetic induction field is shown.

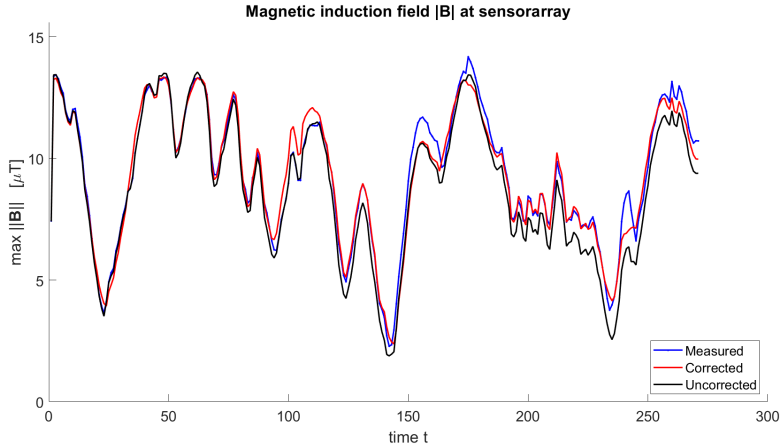


Figure 6.18: Maximum reduced magnetic induction field at the sensor array for the measurement, uncorrected and hybrid model. The maximum per time step is taken over all 200 sensors.

## 6.11. CONCLUSION

In this chapter, a hybrid model is proposed to describe temporal changes in the magnetisation of a ferromagnetic object. By the means of the Method of Moments and the Rayleigh hysteresis model, a mathematical model is derived that describes the changes of magnetisation in a ferromagnetic object for a varying background field. The addition of a dictionary regularisation allows the user to obtain accurate solutions to the inverse problems that are encountered in the application of the hybrid model. A data-assimilation scheme is introduced to correct the magnetisation estimation by the mathematical model to improve performance of the model.

A Numerical Twin experiment is conducted to test the consistency of the hybrid model. It is shown that the methodology is able to reproduce the simulated data accurately. Therefore it is concluded that the methodology behind the hybrid model is consistent. Finally, the methodology is validated on an experimental data set. The proposed model is able to simulate the measured data accurately. It is shown that the data-assimilation scheme is essential for a robust model. In the absence of the scheme, it is observed that there is a significant discrepancy when estimating all three components of the magnetic induction field at the sensor array. This suggests that the hysteresis model should include anisotropic behaviour in order to further improve the results. Fortunately, the data-assimilation scheme can detect and correct these inaccuracies, which results in robust predictions of the magnetic state.

Future steps are to include anisotropic behaviour into the model, as it is observed that the assumption on isotropic material is probably too strong. Furthermore, an online parameter estimation of the material parameters of the Rayleigh Model can be included in the assimilation step, which can lead to an improved performance of the hybrid model. Furthermore, more advanced data assimilation methods can be used to improve the performance of the update step. A Kalman filter approach could lead to an improvement of the hybrid model.

## REFERENCES

- [1] L. Bengtsson, M. Ghil, E. Källén (Eds.). *Dynamic Meteorology: Data Assimilation Methods*. Springer, New York. 1981. p. 330.
- [2] Steven L. Brunton and J. Nathan Kutz. *Data-driven science and engineering: machine learning, dynamical systems, and control*. Cambridge University Press. 2019.
- [3] D. Calvetti and E. Somersalo, *Introduction to Bayesian Scientific Computing*. Springer-Verlag New York Inc.. 2007.
- [4] O. Chadebec, J. L. Coulomb, J. P. Bongiraud, G. Cauffet, and P. Le Thiec. Recent improvements for solving inverse magnetostatic problem applied to thin hulls. *IEEE Trans. on Magn.*, Vol. 38, no. 2, pp. 1005–1008, 2002.
- [5] O. Chadebec, J. L. Coulomb, G. Cauffet, and J. P. Bongiraud. How to Well Pose a Magnetization Identification Problem. *IEEE Trans. on Magn.*. Vol. 39. No. 3. pp: 1634–1637. 2003.
- [6] M. B. Giles and N. A. Pierce. An introduction to the Adjoint Approach to Design. *Flow, Turbulence and Combustion*. No. 65. 2000.
- [7] P. C. Hansen and D. P. O’leary. The use of the L-curve in the regularization of discretization of discrete ill-posed problem. *J. Sci. Comput.* 14. pp: 1487 – 1503. 1993.
- [8] John. J. Holmes. *Exploitation of A Ship’s Magnetic Field Signatures*. Morgan & Claypool publ. Inc. 2006.
- [9] John. J. Holmes. *Modeling a Ship’s Ferromagnetic Signatures*. Morgan & Claypool publ. Inc. 2007.
- [10] John. J. Holmes. *Reduction of a Ship’s Magnetic Field Signatures*. Morgan & Claypool publ., Inc. 2008.
- [11] J. D. Jackson. *Classical Electrodynamics*. 3rd ed. New York: John Wiley & Sons, Inc. 1999.
- [12] D. Jiles and D. Atherton. Theory on Ferromagnetic Hysteresis. *Journal of Magnetism and Magnetic Materials* 61. Vol: 48. 1986.
- [13] M. Kachniarz, R. Szewczyk. Study on the Rayleigh Hysteresis Model and its Applicability in Modeling Magnetic Hysteresis Phenomenon in Ferromagnetic Materials. *Acta Physica Polonica A*. Vol: 131, No. 5. pp: 1244 – 1249. 2017.
- [14] V. François-Lavet, F. Henrotte, L. Stainier, L. Noels, and C. Geuzaine. An energy-based variational model of ferromagnetic hysteresis for finite element computations. *Journal of Computational and Applied Mathematics*. Vol: 246. pp: 243 – 250. 2013.
- [15] A. Morandi, M. Fabbri and P. Ribani. A modified Formulation of the Volume Integral Equations Method for 3 – D Magnetostatics. *IEEE Trans. on Magn.*. Vol: 46. No. 11. 2010.

- [16] L. Prigozhin, V. Sokolovsky, J. W. Barret, and S. Zirka. On the Energy-Based Variational Model for Vector Magnetic Hysteresis. *IEEE Trans. on Magn.*. Vol: 52. No. 12. 2016.
- [17] A. Sheiner, L. Frumkis, B. Ginzburg, N. Salomonski, and B. Kaplan. Magnetic Anomaly Detection Using a Three-Axis Magnetometer. *IEEE Trans. Magn.*. Vol: 45. No. 1. pp: 160 – 167. 2009.
- [18] R.C. Smith. Smart Material Systems. Model Development. SIAM. 2005.
- [19] O. J. G. Somsen, G. P. M. Wagemakers. Separating Permanent and Induced Magnetic Signature: A Simple Approach. *International Journal of Electrical, Computer, Energetic, Electronic and Communication Engineering*. Vol: 9. No. 10. 2015.
- [20] Edward. D. Torre. Magnetic Hysteresis. Wiley-IEEE Press. 1999.
- [21] A.R.P.J. Vijn, E.S.A.M. Lepelaars, J.B.L. Dubbeldam, M.B. van Gijzen, A.W. Heemink. Magnetic susceptibility Estimation for Magnetostatics. *IEEE Trans. on Magn.*. Vol. 55. No. 3. 2019.
- [22] Y. Vuillermet, O. Chadabec, J. L. Coulomb, J. P. Bongiraud, G. Cauffet and P. Le Thiec. Scalar Potential Formulation and Inverse Problem Applied to Thin Magnetic Sheets. *IEEE Trans. on Magn.*. Vol. 44. No. 6. 2008.

# APPENDIX A. PSEUDO-CODE FOR HYBRID MODEL

In this appendix, a pseudo-code for the algorithm is given. During stepping from time  $n$  to  $n + 1$ , a number of problems are solved to estimate the magnetic state by means of the Method of Moments and the data-assimilation scheme. The algorithm is first initialised by estimating the initial magnetic state for a prescribed set of hysteresis parameters. The pseudo-code is found in Fig. 19.

**Algorithm 1** Hybrid Model MoM+Hyst

---

**Input:**  $\mathbf{M}_{per}(0) \leftarrow \mathbf{M}_0$  ▷ Initial state solution  
**Input:**  $\theta|_{t=0} \leftarrow \theta_0$  ▷ Initial guess parameters  
**Input:**  $\mathbf{H}_m$  ▷ Set memory for hysteresis model

- 1: **procedure**  $\mathcal{F}(\mathbf{M}_{per}(n), \mathbf{B}_0(n+1), \mathbf{B}_m(n+1))$
- 2:   **for**  $n \rightarrow n+1$  **do** ▷ Outer, sampled time-loop
- 3:      $\mathbf{b}_0 = \mathbf{B}_0(n)$  ▷ Background field at  $t = t_n$
- 4:      $\mathbf{b}_1 = \mathbf{B}_0(n+1)$  ▷ Background field at  $t = t_{n+1}$
- 5:      $\Delta \mathbf{b} = \mathbf{b}_1 - \mathbf{b}_0$  ▷ Change in background field
- 6:      $\mathbf{B}_m = \mathbf{B}_m(n+1)$  ▷ Measured field at  $t = t_{n+1}$
- 7:     **function** COMPUTE  $\mathbf{M}(n+1|n)$  AND  $\mathbf{H}_{in}$
- 8:       Linearisation:  $\chi = \left. \frac{\partial \mathbf{M}}{\partial \mathbf{H}} \right|_{t=t_n, \theta}$ , where  
        $(\mathbf{H}_i(n), \mathbf{M}(n))$  is from previous time step.
- 9:        $\Delta \mathbf{M} = A(\chi)^{-1} f \Delta \mathbf{b}$
- 10:        $\mathbf{M}(n+1|n) \leftarrow \mathbf{M}(n|n) + \Delta \mathbf{M}$
- 11:        $\mathbf{H}_{in} = (\mu_0^{-1} C - I) \mathbf{M}(n+1|n)$
- 12:     **end function**
- 13:     **function** UPDATE MAGNETIC MEMORY
- 14:       for all  $j \in \{x, y, z\}$ :
- 15:        $(d\mathbf{H}_m)_j^+ = (\mathbf{H}_m)_j - \mathbf{H}_j$
- 16:       **if**  $\sigma((d\mathbf{H}_m)_j^+) \neq \sigma((d\mathbf{H}_m)_j^-)$  **then**
- 17:          $(\mathbf{H}_m)_j \leftarrow \mathbf{H}_j$
- 18:       **end if**
- 19:     **end function**
- 20:     **function** UPDATE  $\mathbf{M}(n+1|n)$
- 21:        $\mathbf{B}_{res} = C\mathbf{M}(n+1|n) - \mathbf{B}_m$
- 22:       Solve:  $\Delta \mathbf{M} = \operatorname{argmin}_{\mathbf{M} \in \mathbb{R}^{3N_e}} \mathcal{J}_2(\mathbf{M}) + \lambda^2 \|\mathbf{R}\mathbf{M}\|^2$
- 23:        $\mathbf{M}(n+1) \leftarrow \mathbf{M}(n+1|n) + \Delta \mathbf{M}$
- 24:     **end function**
- 25:     **function** COMPUTE FIELDS
- 26:        $\mathbf{B}_c[\mathbf{M}(n+1)] = C_1 \mathbf{M}(n+1)$
- 27:        $\mathbf{H}_{in}(n+1) = (\mu_0^{-1} C - I) \mathbf{M}(n+1)$
- 28:     **end function**
- 29:   **end for**
- 30: **end procedure**

---

Figuur 19: Pseudo-code for the proposed hybrid model.

# 7

## CONCLUSION

The main contribution of this thesis is the development of a Magnetic Signature Prediction Model that can be used in a closed-loop degaussing framework. In particular, we have derived a mathematical-physical model that described the temporal behavior of the signature of a ferromagnetic object. This mathematical-physical model is based on the choice of a hysteresis model to describe the nonlinear effects that occur in ferromagnetic material. In addition, a sensor configuration that measures the magnetic induction field is introduced to correct the mathematical model by means of an assimilation scheme to improve the estimation of the magnetic state of a ferromagnetic object. In this chapter, the conclusions of this thesis and subsequent recommendations are presented.

For readability, we restate the research questions:

- (RQ1) Investigate the state-of-the art developments in the field of ferromagnetism. Which hysteresis model should we choose for our mathematical-physical model?
- (RQ2) How can we determine the initial magnetic state of a vessel?
- (RQ3) Is it possible to obtain an efficient numerical model that describes the temporal dynamics of the ferromagnetic behavior of a large structure?
- (RQ4) What is the added value of data-assimilation in magnetostatic?

Answers on the research questions (RQ1– RQ4) defined in Section 1.5.1 are presented in the same order. After the conclusion a number of recommendations are presented.

### 7.1. ANSWERS TO THE RESEARCH QUESTIONS

A literature study on some well known hysteresis models for ferromagnetic behavior was performed to select the most suitable model for magnetic signature monitoring. The classical models of Lord Rayleigh (**RM**), Jiles and Atherton (**JA**) and the more recent energy-based variational model (**EV**) by Prigozhin et al. were compared in Chapter 3. It is concluded that the Rayleigh model seems to be most promising because of its simple formulation.

Advantages for using the Rayleigh model are its numerical properties, the applicability in weak fields and the straight-forward connection to the Method of Moments as shown in Chapter 6. This answers research question 1 (RQ1).

In (RQ2) we looked at how the initial magnetic state of a vessel can be determined. The magnetic state of a vessel is the combination of the determination of material parameters and the magnetisation distribution. It is noted that both notions are intertwined. To obtain the distribution of the magnetic susceptibility, a parameter estimation method is presented in Chapter 4. Finding the magnetic susceptibility distribution involves solving a regularised nonlinear problem. The Magnetic Susceptibility Estimation Method (**MSEM**) we propose solves this problem. In the case that we consider the Jiles-Atherton model, the material parameters are found by the parameter estimation method proposed in Chapter 5. We have shown that the values of the parameters of the Jiles and Atherton model can be obtained in the case that only measurements in weak applied fields are given. A method to determine the initial magnetisation of a vessel is presented in Chapter 6. The corresponding inverse problem is solved using Dictionary Regularisation. This method is based on an a priori assumption on the shape of the initial magnetisation. Here, we assume that the initial magnetisation is approximately represented by a linear combination of magnetisation distributions that follows from solutions to the Method of Moments. The presented initial magnetisation determination method is successfully validated on experimental data. We conclude that we have obtained a methodology that can accurately determine the initial magnetic state of a vessel.

## 7

Chapter 6 covers research questions (RQ3) and (RQ4). In this chapter, we propose a numerical model that describes the temporal dynamics of the ferromagnetic behavior of a steel object. The connection of the Rayleigh hysteresis model to the Method of Moments allows us to describe these dynamics in time. In reality, it is unlikely that a mathematical-physical model can correctly represent experimental data. Therefore we have introduced a data-assimilation scheme to correct our numerical model with measurements to obtain an improved description of the magnetic state. Through Twin experiments, it is shown that the implementation of our hybrid model is numerically stable and consistent. Using experimental data we have successfully demonstrated the numerical model and the added value of a data-assimilation scheme in magnetostatics.

## 7.2. RECOMMENDATIONS FOR FUTURE WORK

Although the research described in this dissertation forms a good basis for the development of a closed-loop degaussing system, there is more work required in order before such a system can be developed and applied to naval vessels.

As a first step, a sophisticated degaussing controller should be developed that uses the mathematical-physical model to compute optimal degaussing currents for effective degaussing of naval vessels. It is envisioned that techniques from nonlinear control theory are required as the underlying mathematical-physical model is nonlinear. This is a challenging step as research in nonlinear control theory is an open and active field. Due to the character

of the underlying mathematical-physical model, it is expected that *gain-scheduling* might be an effective technique to derive such a nonlinear degaussing controller.

In the present work, the emphasis was on the derivation of a numerical model to describe the temporal changes in the magnetic signature due to the underlying ferromagnetic behavior of steel. Our proposed models are validated in an experimental setup on small ferromagnetic structures. It is clear that when we look at larger ferromagnetic structures, extra challenges will arise such as computational time, out-of-memory issues, and the numerical burden. Therefore, it is important to investigate numerical methods to obtain fast implementations of the forward model. Model Order reduction (MOR), for example Proper Orthogonal Decompositions (POD), can help to reduce the numerical burden of the mathematical-physical model, by embedding the nonlinear model into a lower dimensional subspace. Also the use of hierarchical matrices can reduce the computation time of matrix-vector calculations in the iterative methods used in the current implementation of the numerical model.

In our hybrid model, we have implemented a data-assimilation scheme to support the mathematical-physical model in describing the magnetic state of a ferromagnetic object. We have proposed a general assimilation-scheme that can correct for all (non)linear discrepancies that may occur. However, in many cases a simple correction of the mathematical-physical model can be sufficient in order to simulate measurement data in an accurate way. Such a correction model can be obtained by applying *Total Least-Squares* to a small set of measurements.



# ACKNOWLEDGEMENTS

I would like to thank everyone who has directly or indirectly contributed to my journey into this PhD adventure and to the successful completion of this dissertation.

I would like to start by thanking my supervisors and promotors Arnold Heemink, Johan Dubbeldam and Martin van Gijzen. The trust and freedom you gave me was what I needed to develop myself and give direction to my research. The many “monthly” meetings (you know what I mean :P ) were always a pleasure to have. It was inspiring to see how you were always able to advise me quickly when I got stuck, so that I could continue again at a fast pace. I feel honored for your guidance.

Eugene. Finishing this PhD was not possible without your support as a daily supervisor and copromotor. Your knowledge, eye for details and enthusiasm helped me through this adventure. I cherish our discussions, sometimes not related to my research, and the things we have build up to the point where we stand now. Moreover, I am grateful for not only having had a great mentor and supervisor during my PhD, but also gaining a great friend in the past years.

A special thanks to Bart Jan Peet, who helped me out during the implementation of my numerical model in the final stage of my PhD. Because of your help, we were able to publish our paper and finish my dissertation.

This PhD was not possible without the inexhaustible effort that Eugene Lepelaars and Leon Smit put into securing the necessary funding for pursuing my PhD. Thank you for that!

To conclude, I want to thank everyone in my personal life who supported me in the past five years. My family, friends, and colleagues.



# CURRICULUM VITÆ

## **Adrianus Robert Petrus Johannes VIJN**

Aad Vijn was born on August 21, 1990 in The Hague, the Netherlands. He completed his secondary education in 2009 at the Segbroek College in The Hague. In the same year he started his studies in Applied Mathematics at Delft University of Technology. He obtained his BSc degree and MSc degree in Applied Mathematics in 2014 and 2016 respectively. He wrote his master thesis titled “Inverse Modeling for Magnetic Signature Monitoring of Naval Ships” under the supervision of dr. M. Keijzer and dr. ir. E.S.A.M. Lepelaars. In 2016 he started his PhD research under the supervision of prof. dr. ir. A.W. Heemink, prof. dr. ir. M.B. van Gijzen and dr. J.L.A. Dubbeldam at Delft University of Technology.



# LIST OF PUBLICATIONS

## JOURNAL PAPERS

- A.R.P.J. Vijn et al.. Magnetic Susceptibility Estimation for Magnetostatics. *IEEE Trans. on Magn.*. Vol: 55, Issue: 3, March 2019.
- A.R.P.J. Vijn et al.. Parameter Estimation for the Jiles-Atherton Model in Weak Fields. *IEEE Trans. on Magn.*. Vol: 56, Issue: 4, April 2020.
- A.R.P.J. Vijn et al.. Prediction of the Magnetic State of Ferromagnetic Objects by Assimilating Data Into a Physical Model. submitted to *IEEE Trans. on Magn.*. Under review (2021).

## CONFERENCE PAPERS

- A.R.P.J. Vijn and H. Jongbloed. Ferromagnetic Hysteresis Models for Magnetic Signature Prediction: a study to select the right model. Proceeding paper, Marelec Conference 2019.